SURFACE BIOLOGICAL MODIFICATION AND CELLULAR INTERACTIONS OF MAGNETIC SPINEL FERRITE NANOPARTICLES

A Dissertation
Presented to
The Academic Faculty

By

Eva Liang-Huang Heintz

In Partial Fulfillment
Of the Requirements for the Degree
Doctor of Philosophy in Chemistry
Georgia Institute of Technology

October, 2004

SURFACE BIOLOGICAL MODIFICATION AND CELLULAR INTERACTIONS OF MAGNETIC SPINEL FERRITE NANOPARTICLES

Approved by:

_____
Dr. Z. John Zhang

_____
Dr. Jiri Janata

_____
Dr. Laren Tolbert

_____
Dr. L. Andrew Lyon

_____
Dr. Christopher Jones

October 20th, 2004

This thesis is dedicated to:

My grandfather, Jia Wen Tsai
My parents, Ling X. Jia and Peihuang Huang
My husband, Joseph G. Heintz
and to Mackie Heintz.

ACKNOWLEDGEMENT

I owe gratitude to a number of people for helping me get to where I stand today. My family made so many sacrifices for me and it is their unconditional support and encouragement that I am here today. Giving up was never an option. Each time that overwhelming feeling of giving up takes over, it was family and all those I thank here that helped me survive through those obstacles.

I had a rough start at Georgia Tech and throughout every unexpected events, Dr. Janata was always there to guide me through. I will never forget all the time Dr. Janata has devoted to me. Dr. Tolbert was the chair of this department when I started. He was a fascinating teacher and a chair that cared about students. He stood by me in good and bad situations and is another person that I will always owe gratitude to. I would also like to thank Dr. Lyon for scientific stimulating discussion and feedback of my research and for allowing me to use instrumentations in his lab for explorative research. When I was lost and searching for a new group to work in, Dr. Zhang reached out and took me under his wing. He immediately placed me in his lab and gave me the opportunity to work with fascinating science. Dr. Zhang was also very supportive of my other involvements with Georgia Tech such the Graduate Student Forum and serving and the Graduate Student Government Association. So I would like to extend a special thanks to Dr. Zhang. There

are just a few more professors I would like to thank. I would like to express great gratitude to Dr. Fahrni for many hours of helpful discussion and Dr. Doyle for trusting me with everything in your lab. Additionally, I would like to thank Dr. Chris Jones for serving on my committee and giving me thoughtful and sound feedback.

My list continues with Dr. Cam Tyson and Kathy Huggins, who not only steered me towards the right direction over and over again but were true friends. The relationship that I have built with Cam and Kathy will be one that I will always cherish. From the first day I came to Georgia Tech, Dr. Anna Samia always greeted me with a smile. She was always there to guide me and still does so all the way up in Chicago. I would also like to thank Dr. Christy Vestal for sharing her knowledge with me and for stimulating discussions in science. Both Anna and Christy were great friends and will forever be great friends. Additionally, I would like to thank Ms. Priyanka Rohatgi for training me on pertinent biological techniques required to complete my work. A big thanks to Mr. Jose I. Gonzalez for taking fluorescence images for me and Dr. Lynn Capadona for assisting in the darkfield microscopy portion of my thesis. Sometimes lab life can be a drudge but it was friends like Chala Cripps, Christine Nolan, Dr. M. Tony Belcher, Dr. Victor DeJesus, Dr. Tiffany Hoang, Kathy White, and many other “Lyoners” and “Schusterers” that kept me from going insane. Finally, I would like to thank the staff members of the Chemistry Department for making stay at Georgia Tech a pleasant one.

TABLE OF CONTENTS

Acknowledgement iv

Table of Contents vi

List of Tables xi

List of Figures xii

Summary xviii

Chapter 1 Introduction to Magnetism and Magnetic Material 1

1.1 Introduction 1

1.2 Brief review of Magnetism 4

1.2.1 Fundamentals 4

1.2.2 Magnetic Classification 6

1.3 Superparamagnetism 11

1.3.1 Single Domain 11

1.3.2 Superparamagnetism 13

1.3.3 Stoner – Wohlfarth Theory and Néel Theory 15

1.3.4 Anisotropy 17

1.4 Applications 18

1.4.1 Ferrofluids 18

1.4.2. Data Storage 19

1.4.3 Magnetic Resonance Imaging (MRI) Contrast Enhancement 21

14.4 Magnetic Hyperthermia 23

1.4.5 Magnetic Separation 25

1.4.6 Drug Delivery 26

1.5 References 29

Chapter 2 Spinel Ferrites and Synthesis Methods of Magnetic Nanoparticles 34

2.1 Spinel Ferrites 34

2.2 Synthesis Methods of Magnetic Nanoparticles 36

2.2.1 Ball Milling 36

2.2.2 Sonochemical Methods 37

2.2.3 Sol-gel Method 38

2.2.4 Co-Precipitation 40

2.2.5 Microemulsions 41

2.2.5.1 Reverse Micelle Method 40

2.2.5.1 Normal Micelle Method 42

2.2.6 Seed Mediated Thermal Decompositional Method 44

2.3 References 49

Chapter 3 Instrumentation and Related Techniques 53

3.1 Magnetic and Physical Characterization Instrumentation 53

3.1.1 Powder X-ray Diffraction 53

3.1.2 SQUID Magnetometry 56

3.1.3 Transmission Electron Microscopy (TEM) 59

3.1.4 Inductively Coupled Plasma – Optical Emission Spectrometry 59

3.2 Biologically Related Instrumentation and Techniques 62

3.2.1 Laser Scanning Confocal Microscopy (LCSM) 62

3.2.2 Dark Field Microscopy 66

3.2.3 Flow Cytometer 67

3.2.4 Cell Culture Techniques 70

3.2.4.1 Introduction to Cell Culture 70

3.2.4.2 Transfection 71

3.3 References 73

Chapter 4 Modulating the Magnetic Properties of Cobalt Spinel Ferrite Nanoparticles with Samarium 76

4.1 Introduction 77

4.2 Experimental 79

4.2.1 Synthesis 79

4.2.2 Instrumentation 80

4.3 Results and Discussion 80

4.3.1 Composition Variation 81

4.3.2 Size Variation 89

4.4 Conclusions 94

4.5 References 96

Chapter 5 Cellular Uptake and Magnetic Manipulation of Cobalt Spinel Ferrite – Oligonucleotide Conjugates 98

5.1 Introduction 99

5.2 Experimental 101

5.2.1 Cell Lines and Medium Preparation 101

5.2.2 Preparation of Magnetic Nanoparticle – Oligonucleotide Conjugates 102

5.2.3 Transfection of Magnetic Nanoparticle – Oligonucleotide Conjugates in Cells 107

5.2.4 Confocal Microscopy and Dark Field Microscopy 107

5.2.5 Inductively Coupled Plasma – Optical Emission Spectrometry 109

5.3 Results and Discussion 110

5.3.1 Crosslinking of $CoFe_2O_4$ to Oligonucleotides 110

5.3.2 Lipofection of $CoFe_2O_4$ – Oligonucleotide Conjugates into HeLa and CV – 1 Cells 110

5.4 Conclusions 124

5.5 References 117

Chapter 6 Surface Modification of Cobalt and Manganese Spinel Ferrites for Cellular Delivery 128

6.1 Introduction 129

6.2 Experimental 130

6.2.1 Preparation of Spinel Ferrite – Oligonucleotide Conjugates 130

6.2.2 Preparation of $CoFe_2O_4$ – HPC Conjugates 135

6.2.3 Transfection 136

6.2.4 Cellular Delivery of Positively Charged $CoFe_2O_4$ into CV – 1 Cells 136

6.2.5 Characterization 137

6.3 Results and Discussion 137

6.3.1 Crosslinking of MFe_2O_4 (M = Co, Mn) to Oligonucleotide 137

6.3.2 Transfection of MFe_2O_4 – Oligonucleotide Conjugates (M = Co, Mn) into CV – 1 Cells 139

6.3.3 Surface Charge Modification with HPC and Cellular Delivery of $CoFe_2O_4$ – HPC 145

6.4 Conclusion 147

6.5 References 148

Chapter 7 Conclusions and Future Work 149

7.1 Tunability of magnetic nanoparticles 149

7.2 Cellular Uptake of Magnetic Nanoparticles 150

7.3 Magnetic Nanoparticles Coupled to Viruses 152

7.4 Conclusion 152

Appendix A Magnetic Force and Hemadynamic Force Estimation 154

A.1 Magnetic Gradient Determination 154

A.2 Magnetic Force Experienced by Cells 156

A.3 Hemadynamic Force Experienced by Cells 157

A.4 Conclusions 158

A.5 References 160

Appendix B Cowpea Mosaic Virus Coupled Cobalt Spine Ferrites 161

B.1 Introduction 162

B.2 Experimental 163

B.3 Results and Discussion 166

B.4 Conclusions 168

B.5 References 169

LIST OF TABLES

Table 1.1	Magnetic units in both Gaussian and SI unit.	6
Table 1.2	Summary of the magnetic behavior of different magnetic materials.	10
Table 1.3	Examples of critical diameters of some common magnetic materials.	13
Table 3.1	A comparison between the magnetic field of Earth, human body, and the threshold of SQUID.	57
Table 4.1	Summary of magnetic characteristics of $CoSm_xFe_{2-x}O_4$	83
Table 4.2	Magnetic characteristics of $CoSm_{0.19}Fe_{1.81}O_4$ of various sizes.	90
Table A.1	Table A.1 Magnetic Flux change with distance	155

LIST OF FIGURES

Figure 1.1	Important historical contributions of the fundamentals of magnetism.	2
Figure 1.2	Schematic representation of domains and domain walls in bulk material.	3
Figure 1.3	Magnetism classification of different elements.	8
Figure 1.4	Magnetic moment ordering in (a) diamagnetics, (b) paramagnetics, (c) ferromagnetics, (d) antiferromagnetics, (e) ferrimagnetics.	9
Figure 1.5	Schematic representation of domain wall moving as an external field is applied, minimizing the magnetostatic energy.	12
Figure 1.6	Correlation between particle size and domain classification and coercitivity.	14
Figure 1.7	Schematic representation of energy barrier for magnetization reversal.	15
Figure 1.8	Diagram showing the steady increase in storage capacity and decrease in physical size hard disk drives after the commercialization of 305 RAMAC.	20
Figure 2.1	Partial unit cell structure of a typical spinel ferrite.	36
Figure 2.2	Cavitation process.	38
Figure 2.3	Products that can be formed through sol-gel synthesis.	39
Figure 2.4	General structure of (a) reverse micelle and (b) normal micelle	42

Figure 2.5	Figure 2.5 Three-dimensional cross section plot illustrating the effects of metal salt concentration [S(M)] and base concentration [A(M)] at constant temperature.	46
Figure 2.6	Figure 2.6 Three-dimensional cross section plot illustrating the effects of metal salt concentration [S(M)] and reaction temperature (T) using constant base concentration.	46
Figure 3.1	Interference between x-ray beams scattering rows of atoms in a crystal.	55
Figure 3.2	Josephson junction.	58
Figure 3.3	Schematic representation of an Inductively Coupled Plasma Spectrometer.[16] Basic components include sample introduction system, torch, generator, optics, spectrometer, and a computer interface.	61
Figure 3.4	Illumination difference between conventional wide field microscopes and laser scanning confocal microscopes.	62
Figure 3.5	Schematic representations of the components of a typical confocal microscope. A laser is used as a light and excitation source. The beam of laser is focused onto the sample. Light signal hits the low noise photomultiplier tube and is then amplified, processed, then displayed.	64
Figure 3.6	Flow of laser beam through confocal microscope.	65
Figure 3.7	Darkfield condenser / objective pair.	67
Figure 3.8	Basic components of a flow cytometer include laser(s) as an illuminating source, flow cell to house the capillary that cells flow through in a single file, lenses to focus laser(s) and to focus the signal, filters to select specific wavelength(s) for detection, and photodiode or photomultiplier tube detectors.	69
Figure 4.1	XRD pattern of $CoSm_xFe_{2-x}O_4$ compared to native $CoFe_2O_4$. Intensities were intentionally offset to demonstrate the similarity in patterns.	82

Figure 4.2 Varying percent Sm doped susceptibility vs. temperature plot of a series of 7.25nm $CoSm_xFe_{2-x}O_4$ (x = 0, 0.027, 0.085, 0.145, 0.187) magnetic nanoparticles. The blocking temperature correlates to the peak or maximum susceptibility point of each curve. 85

Figure 4.3 Figure 4.3 Hysteresis loop of 7.2nm $CoSm_xFe_{2-x}O_4$ magnetic nanoparticles at 5K. The magnetic field is ramped from zero to 50 kOe then to the same magnitude but in a different direction. Once at the magnetization saturation point, where moments align with the direction of the applied field, the reversal of magnetic moments generates a hysteresis loop. The introduction of samarium into cobalt spinel ferrite reduces the M_s and increases the H_c due to high coercive forces from samarium. 86

Figure 4.4 Figure 4.4 Hysteresis measurement of $CoSm_{0.19}Fe_{1.81}$ at 300K. Above the blocking temperature of $CoSm_{0.19}Fe_{1.81}$ (283.4K), there is enough thermal energy to overcome the E_A allowing reversal of magnetization, hence there is an absence of hysteresis. 87

Figure 4.5 Figure 4.5 XRD pattern of various sized $CoSm_{.0191}Fe_{1.981}O_4$. The intensities were intentionally offset to demonstrate the similarity in patterns. Inset shows a TEM micrograph of a sample of approximately 7.2nm diameter at 100K magnification. 91

Figure 4.6 Figure 4.6 Size variation susceptibility vs. temperature plot of $CoSm_{.019}Fe_{1.81}O_4$. For the 12.5 nm $CoSm_{0.19}Fe_{1.81}O_4$ curve, it is actually made up of two curves, one ranging from 5-400K and another from 400-500K. The maximum susceptibility point or peak of the curve correlates to the blocking temperature of different sized $CoSm_{.019}Fe_{1.81}O_4$. 92

Figure 4.7 Figure 4.7 Hysteresis loop of various sized $CoSm_{.0191}Fe_{1.981}O_4$ at 5K, 5T. The magnetic field is ramped from zero to 50 kOe then to the same magnitude but in a different direction. Once at the magnetization saturation point, where moments align with the direction of the applied field, the reversal of magnetic moments generates a hysteresis. From the different hysteresis loops, there is a direct correlation

between size and M_s. An increase in size produced higher magnetization saturation points and vice versa for smaller sizes. Coercitivity initially increases with size then decreases with increasing size. This may be attributed to initial coherent rotation of magnetic moments followed by spin canting. 93
.

Figure 5.1 Schematic representation of the crosslinking chemistry behind mnp-oligo conjugates. An amino functionalized magnetic nanoparticle is reacted with the maleimide group of SPDP leaving the thiol reactive terminus of the crosslinker exposed and unreacted. In the presence of reduced thiol-terminated oligonucleotides, a thiol-thiol exchange between the thiol terminus of the oligo and the disulfide bond of the crosslinker occurs forming a new disulfide bond. 103

Figure 5.2 Illustration of the general protocol for transfection with Lipofectamine™. 106

Figure 5.3 Grids of a hemacytometer. The number of cells in region 5 represents the number of cells, n, present in 0.1 μL. Hence, the total number of cells per 1 mL is n x 10^4. 109

Figure 5.4 HeLa cells transfected with $CoFe_2O_4$ – oligonucleotide **3**. 112

Figure 5.5 CV-1 cells transfected with $CoFe_2O_4$ – oligonucleotide **3**. 113

Figure 5.6 Confocal image of native HeLa cells. 110

Figure 5.7 Confocal image of native CV1 cells. 110

Figure 5.8 Darkfield micrographs of (a) native CV – 1 cells, (b) $CoFe_2O_4$ – oligo clusters, (c) CV – 1 cells transfected with $CoFe_2O_4$ – oligos. 114

Figure 5.9 Confocal micrograph of C-1 cells transfected with $CoFe_2O_4$ – oligonucleotides where oligonucleotides were not fluorescently labeled. 116

Figure 5.11 Movie of cells responding to the magnetic field (heintz_eva_l_200412_phd_magneticmovement1.mpg) 117

Figure 5.12	Confocal micrograph of CV-1 cells incubated transfected with $CoFe_2O_4$ nanoparticle mixed (not conjugated to) with fluorescein labeled oligonucleotides.	119
Figure 5.13	Confocal micrograph of CV-1 cells transfected with fluorescein labeled oligonucleotides without the presence of magnetic nanoparticles.	120
Figure 5.14	Fluorescence micrograph of CV-1 cells transfected with $CoFe_2O_4$ – oligonucleotide conjugates demonstrating the transfecting efficiency.	122
Figure 5.15	Reflective and fluorescent overlay confocal images of CV-1 cells (a) 24hrs, (b) 48hrs, (c) 96hrs, (d) 250hrs post transfection.	123
Figure 6.1	Surface modification of magnetic nanoparticles with epichlorohydrin – EMCA for attachment of thiol terminated oligonucleotides through a thiol ester bond formation. Alternatively, the first step can be accomplished with 1% APTES.	132
Figure 6.2	Surface functionalization of magnetic nanoparticle with APTES – MPA – EMCA for attachment of amine terminated oligonucleotides.	134
Figure 6.3	Surface modification of $CoFe_2O_4$ for the attachment of HPC.	135
Figure 6.4	Functionalization of magnetic nanoparticles ($CoFe_2O_4$ or $MnFe_2O_4$) with a heterocrosslinker for amide bond attachment to oligonucleotides	138
Figure 6.5	Confocal overlay z-stack images of CV-1 cells transfected with $CoFe_2O_4$-epichlorohydrin – EMCA – SH – oligonucleotide.	140
Figure 6.6	Confocal overlay z-stack images of HeLa cells transfected with $CoFe_2O_4$-epichlorohydrin – EMCA – SH – oligonucleotide	141
Figure 6.7	Confocal overlay z-stack images of HeLa cells transfected with $MnFe_2O_4$ – EMCA – SH – oligonucleotide	142

Figure 6.8	Confocal overlay z-stack images of CV-1 cells transfected with $CoFe_2O_4$ – EMCA – NH – oligonucleotide	143
Figure 6.9	Figure 6.5 Confocal overlay z-stack images of HeLa cells transfected with $CoFe_2O_4$ – EMCA – NH – oligonucleotide.	144
Figure 6.10 	Movie of synchronized movements of the cells in response to an external magnetic field (heintz_eva_l_200412_phd_magneticmovement2.mpg).	145
Figure 6.11	Bright field micrographs of CV-1 cells with $CoFe_2O_4$ – HPC moving with an external magnetic field.	146
Figure A.1	A.1 Graph of Magnetic field of a small Nd-Fe-B magnet with distance.	155
Figure B.1	Surface modification of magnetic nanoparticles with EMCA crosslinker for the attachment of CPMV	165
Figure B.2	Three dimensionally reconstructed cryo-TEM image of the (a) native CPMV virus and (b) CPMV-$CoFe_2O_4$ virus.	167
Figure B.3	(a) Three dimensional reconstructed cryo-TEM image of mutant CPMV labeled with 1.45nm gold nanoparticles. (b) Difference electron density map showing the gold nanoparticles and the nucleic acids. (c) Superimposed image of a pentametric section of the difference electron density map and the atomic model of CPMV.	167

SUMMARY

The interest in magnetic nanoparticles is multi-dimensional. Fundamentally, it is important to be able to control their magnetic properties and to correlate to specific applications. In biology, magnetic nanoparticles offer promising potential as magnetic carriers or “chaperones” for magnetic localization and manipulation of therapeutic reagents.

The synthesis of superparamagnetic $CoFe_{2-x}Sm_xO_4$ nanoparticles and the tunability of their magnetic properties by size and composition variations are discussed. An increase in size of $CoSm_{0.19}Fe_{1.81}O_4$ nanoparticles produced an increase in blocking temperature and saturation magnetization, but a non-linear coercitivity response was observed with change in size. By varying the composition, the saturation magnetization of $CoFe_{2-x}Sm_xO_4$ decreased dramatically while the coercitivity increased when compared to native cobalt spinel ferrite ($CoFe_2O_4$) nanoparticles. These results demonstrate how the magnetic properties of cobalt spinel ferrite nanoparticles can be tailored to specific applications.

Surface modifications of cobalt spinel ferrite nanoparticles facilitated the conjugation of oligonucleotides. Using a transfection reagent, $CoFe_2O_4$ – oligonucleotide

conjugates were delivered into mammalian cells. Post transfection, synchronized movement of cells in response to an external magnetic field was observed. This demonstrated the possibility of magnetic manipulation and localization of therapeutic reagents coupled to $CoFe_2O_4$ magnetic nanoparticles.

Results from this thesis demonstrate the potential role of magnetic spinel nanoparticles in cell biology and will facilitate the progress towards *in vivo* testing.

CHAPTER I

INTRODUCTION TO MAGNETISM AND MAGNETIC MATERIALS

1.1 Introduction

One of the first documented encounters with a magnetic material was made by Magnes, a Greek shepherd, around 900 B.C.[1] While walking across a field with an abundant amount of black stones, the iron tip of his staff struck one of these stones and he observed that the nails in his hobnail boots were being pulled out of their place by these stones.[1,2] These black stones are lodestones, comprised of the mineral magnetite (Fe_3O_4). They were also referred to as the bones of Haroeri, grandson of the earth goddess, by ancient Egyptians.[2] The magnetism phenomenon had many early explanations that lacked sound concepts. For example, Thales (636-546 B.C.), a Greek philosopher, explained that the lodestones had a soul just like animals.[1,2] It was discovered that a lodestone carved into the shape of a spoon sitting on a polished bronze plate had been used as a South pointing device invented by the Chinese around 200 B. C.[1,2] However, it was not until 1600 A.D. that modern concepts of magnetism evolved. Dr. William Gilbert, court

physician to Queen Elizabeth I of England, systematically studied and documented (~1600 A. D.) that the entire world is a big magnet.[1] Since then, a number of historical contributions have helped evolve the current theories relating to magnetism (See figure 1.1).

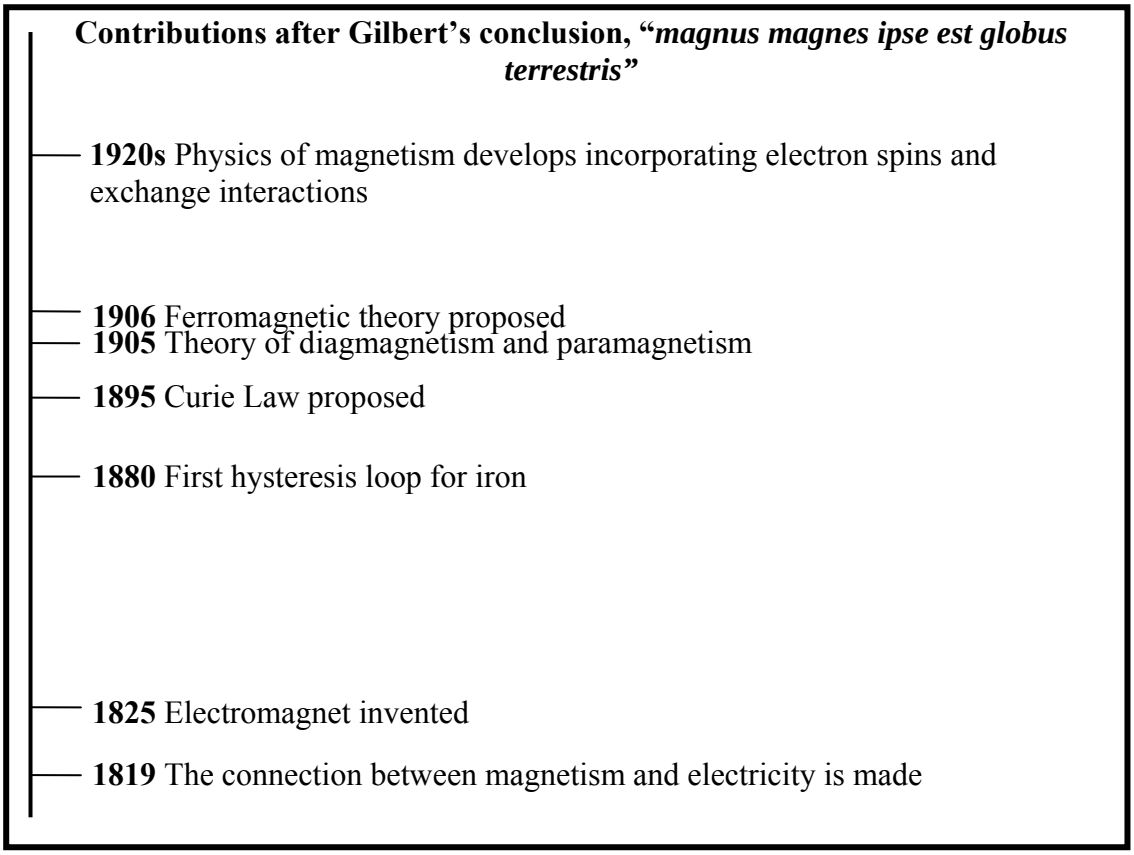

Figure 1.1 Important historical contributions to the fundamentals of magnetism.[2]

The drive to miniaturize magnetic materials and to develop novel materials often involves scaling down to nanometers. The magnetic behavior of nanoparticles differs dramatically from their bulk counterparts.[2-4] In bulk material, the magnetic behavior is influenced by domains and domain walls (See figure 1.2). Magnetic domains are regions in a crystal where the magnetic moment orientation is different but aligns with the easy axis and each domain is separated by a thin domain wall.[3,4] Magnetic nanoparticles that are small enough, are single domained. Magnetic domains exist to reduce the energy of the system but when the size of magnetic nanoparticles decrease to a critical size, D_c, it can no longer support multiple domains and it exhibits interesting single domain behavior.[3,4] In this chapter, the fundamentals of magnetism, and single domain behavior, as well as superparamagnetism are briefly reviewed. Since it is impossible to list all of the applications in which magnetic nanoparticles can be utilized, an overview of some of the most common applications are discussed.

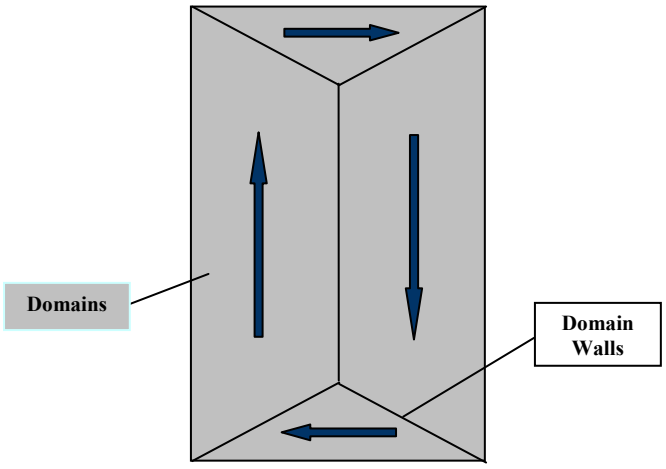

Figure 1.2 Schematic representation of domains and domain walls in bulk materials.

1.2 Brief Review of Magnetism

1.2.1 Fundamentals

There is an intimate relationship between magnetism and electricity. A magnetic field is produced when there are electrical charges moving.[2,5-8] In an atom, when electrons circulate the nucleus, an orbital magnetic moment is produced. Associated with this is the spin magnetic moment produced by electrons spinning about its own axis. When a material is placed under a magnetic field, the *magnetic induction* or the *flux* of magnetic lines through a cross-sectional area of the material can be represented by

$$\mathbf{B} = \mathbf{H} + 4\pi\mathbf{M} \tag{1.1}$$

where **B** is the magnetic induction, **H** is the applied magnetic field, and **M** is the magnetization in response to the field.[5,8] The susceptibility and permeability of a material is also an important factor that relates information such as the type of magnetic material (paramagnetic, diamagnetic, etc.) and the strength of the magnetic effect associated with a particular magnetic material.[6] Essentially, the *susceptibility*, χ, is the ratio of magnetization and the applied field (see equation 1.2).[2,5-8]

$$\chi = \mathbf{M}/\mathbf{H} \tag{1.2}$$

The *permeability*, μ, of the material is given by

$$\mu = \mathbf{B}/\mathbf{H} \tag{1.3}$$

and the susceptibility and permeability can be related by

$$\mu = \mu_0 (1+ \chi) \tag{1.4}$$

where μ_0 is the permeability under vacuum.[2,5-8] In the study of magnetic properties, the susceptibility parameter is the main characterization parameter since it describes the response of a material with an applied magnetic field. Since magnetism interconnects chemistry, physics, and material science, it is worth pointing out that there are two unit systems that are currently acceptable, the SI units and Gaussian (cgs) units (see Table 1.1).

Table 1.1 Magnetic units in both Gaussian and SI unit.[9]

Quantity	Gaussian (cgs) units	SI Units	Conversion factors from cgs to SI unit
B	G	T	10^{-4}
H	Oe	A/m	$10^3/4\pi$
M	emu/cm^3	A/m	10^3
4πm	G	----	----
μ	Dimensionless	H/m	4π x 10^{-7-}
χ	emu/cm^3·Oe	Dimensionless	4π

1.2.2 Magnetic Classifications

Magnetic materials can be categorized as diamagnetic, paramagnetic, ferromagnetic, antiferromagnetic, or ferrimagnetic.[1,4-6,9,10] The two most common classification that account for most of the elements in the periodic table are either diamagnetic or paramagnetic (see Figure 1.3).[5,6,10] *Diamagnetic* materials do not have any unpaired electrons. Hence, there is no net moment in diamagnetic materials (Figure 1.4a). In response to an applied field, diamagnetic materials produce a weak

magnetization that opposes the applied field giving rise to a negative susceptibility. In *paramagnetic* materials, the magnetic moments are randomly oriented due to thermal agitation (Figure 1.4b). From the Curie Law (equation 1.5), we can see that the magnetic ordering of paramagnetic materials is influenced by temperature.[5,8,10]

$$\chi = \mathbf{C}/\mathbf{T} \quad (C = \text{the Currie Constant}) \tag{1.5}$$

Although magnetic moments in paramagnetic materials do not interact with each other, the Curie Law states that with increasing temperature, thermal agitation increases making the moments harder to align.[5,8,10] Hence, there is a small but positive susceptibility. The magnetic moments in *ferromagnetic* materials are aligned in parallel (Figure 1.4c). Due to their magnetic ordering, ferromagnetic materials exhibit magnetization even in the absence of a magnetic field. At or above the transition or Curie temperature (T_c), the magnetic ordering follows the Curie Weiss Law (equation 1.6)

$$\chi = \mathbf{C}/(\mathbf{T}\text{-}\boldsymbol{\theta}) \quad (\theta = \text{the Weiss constant}) \tag{1.6}$$

and moments becomes randomly oriented, behaving like paramagnetic materials.[5,8,10] Materials that are *antiferromagnetic* are similar to ferromagnetic materials. However, due to their exchange interaction between neighboring atoms, their magnetic moments are aligned anti-parallel to each other.[5,8,10] Above the transition temperature, (Neel temperature, T_N) moments cancel out and orient themselves the same way paramagnetic

materials do.[5,8,10] Similar to antiferromagnetic materials, the magnetic ordering of *ferrimagnetic* materials are anti-parallel but have different magnitudes or the number of anti-parallel moments is unequal. A summary of the different magnetic material and their magnetic properties can be found on table 1. 2.

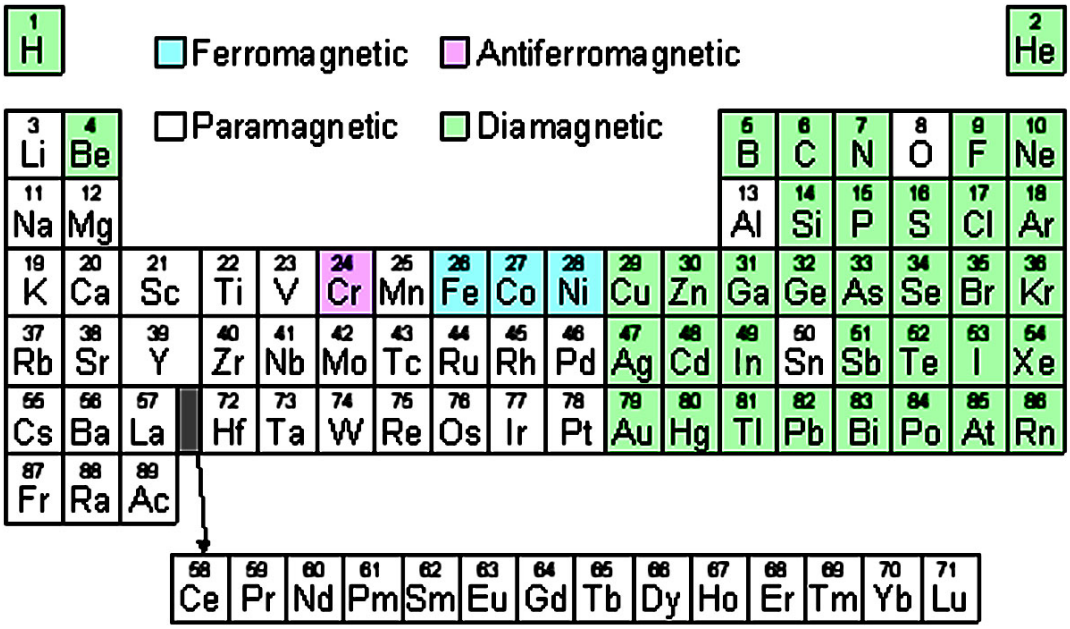

Figure 1. 3 Magnetism classifications of different elements.[9]

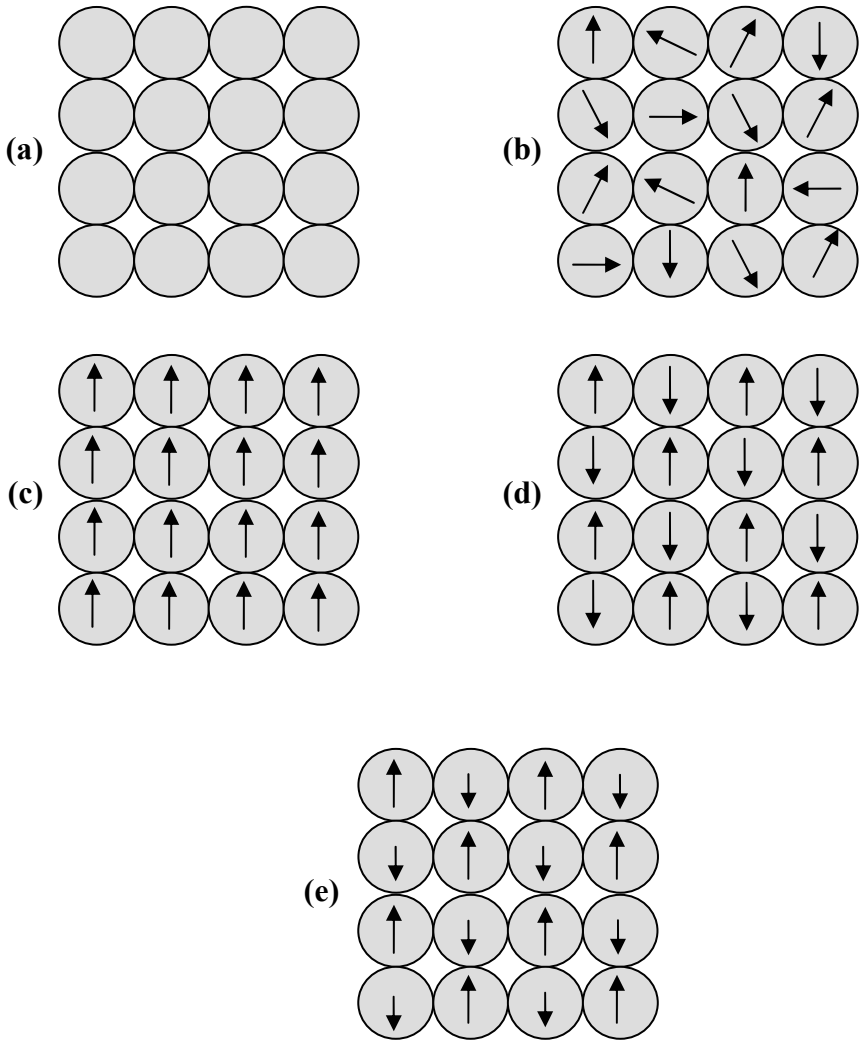

Figure 1.4 Magnetic moment ordering in (a) diamagnetics, (b) paramagnetics, (c) ferromagnetics, (d) antiferromagnetics, and (e) ferrimagnetics.

Table 1.2 Summary of the magnetic behavior of different magnetic materials.[9]

Types of Magnetism	Susceptibility	Magnetic Behavior
Diamagnetic	Small and Negative	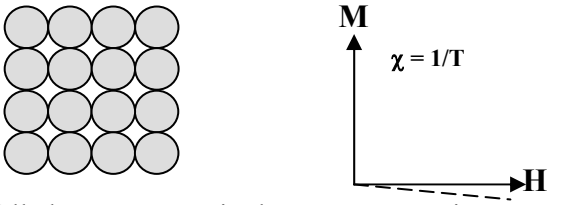 All electrons are paired. No net magnetic moment.
Paramagnetic	Small and Positive	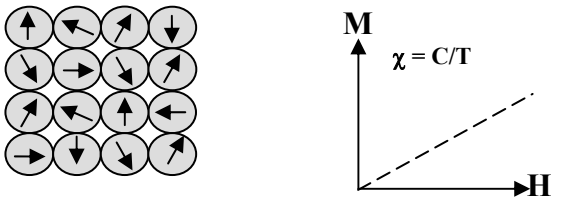 Magnetic moments are randomly oriented.
Ferromagnetic	Large and positive	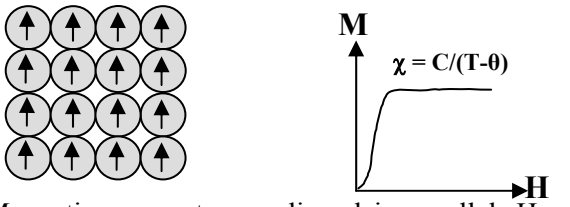 Magnetic moments are aligned in parallel. Have a net magnetization even without external magnetic field.
Anti-ferromagnetic	Small and positive	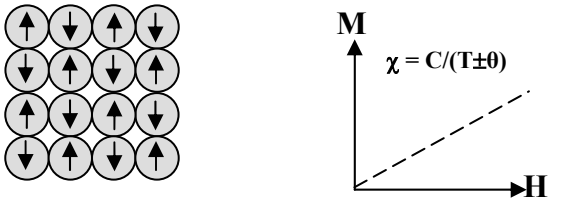 Magnetic moments are anti-parallel. No net magnetization in the absence of an external magnetic field.
Ferrimagnetic	Large and positive	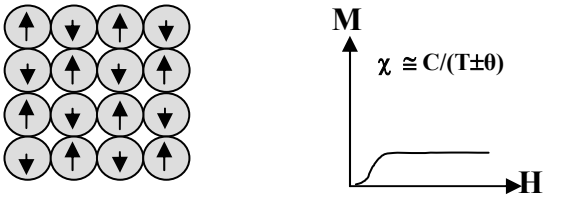 Magnetic moments are aligned anti-parallel. The numbers of opposite moments are not equal giving a net magnetization in the absence of an external magnetic field.

1.3 Superparamagnetism

1.3.1 Single Domain Behavior

In bulk magnetic materials, magnetic domains or large regions (up to several hundred nanometers in diameter) with uniform magnetization, separated by domain walls, exist to reduce the energy of the system.[4,11] Movement and nucleation of the domain walls minimizes the magnetostatic energy (see figure 1.5). When the size of the magnetic material decreases to a critical size (up to several hundred nanometer in diameter), the amount of energy to produce domain walls becomes greater than the reduction in magnetostatic energy making it unfavorable to support multiple domains. As a consequence, only a single domain is formed and supported. In a single domain system, the reversal of magnetization no longer occurs through domain wall motion but requires coherent rotation of the spins, resulting in larger coercitivities. The existence of single domain in particles was first predicted by Frenkel and Dorfman[12] in 1930 but it was well over a decade before Kittel[11] provided the first estimate of the critical size for single domain formation. This critical size can be estimated based on equation 1.7[11,13]

$$D_{cr} = 35\ (KA)^{1/2} / \mu_o M_s^2 \qquad (1.7)$$

where D_{cr} is the critical diameter, K is the anisotropy energy density, A is the exchange energy density, μ_o is the vacuum permeability, and M_s is the saturation magnetization.

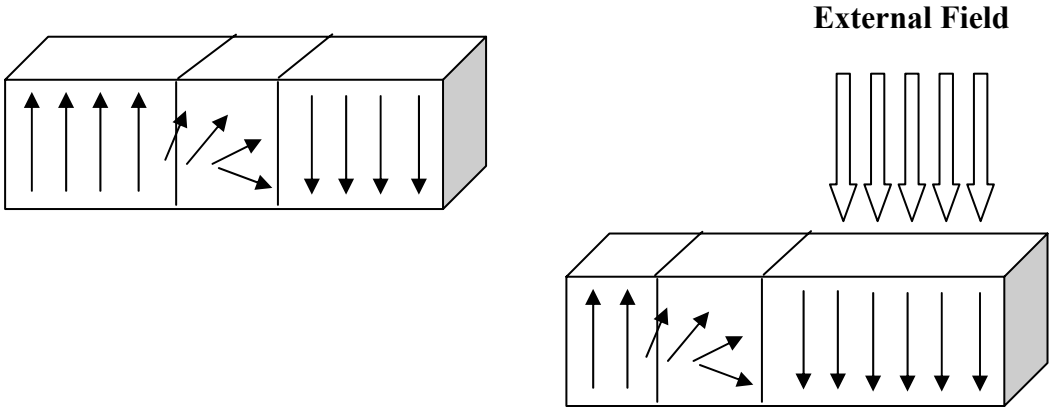

Figure 1.5. Schematic representation of domain wall moving as an external field is applied, minimizing the magnetostatic energy.

Through experimental observations, Kittel[11] summarized that the M_s of single domain ferromagnetic particles are unidirectional and magnetization changes only occur through spin rotation leading to high coercive forces since the spin rotation is opposed by anisotropy forces. In addition, Kittel[11] describes that the magnetization changes occurring at weak magnetic fields may be due to reversible spin rotation associated with a low initial permeability. Hence, D_c can be heavily influenced by M_s, K, and A. Although the range of D_{cr} can cover between 10-800nm, most of the critical diameters for common magnetic nanoparticles are below or around 100nm. For example, the D_c of Co is 70nm

while the D_c of Fe_3O_4 is 128nm.[4] Table 1.3 lists the D_c of some common magnetic materials.

Table 1.3 Examples of critical diameters of some common magnetic materials.[4,14]

Magnetic Material	**D_c (nm)**
Co	70
Fe	14
Ni	55
Fe_3O_4	128
$CoFe_2O_4$	128
$MnFe_2O_4$	50

1.3.2 Superparamagnetism

Superparmagnetism, a term coined by Bean, is unique to magnetic nanoparticles.[15,16] When the size of magnetic nanoparticle decreases below the D_c, magnetic moments become increasingly influenced by thermal fluctuation and the system becomes superparamagnetic. As a consequence there is an unstable magnetization and the

coercitivity approaches zero (see Figure 1.6). In superparamagnetic systems, the temperature at which moments are blocked or unable to relax is referred to as the blocking temperature, T_B. Above the T_B, moments can align with any crystallographic direction and behave like paramagnetic material but with much greater moments.[4,15-17] The criteria for superparamagnetism classification are (1) absence of hysteresis above their blocking temperature and (2) M vs. T must superpose M vs. H/T.[4] Like other magnetic material, the magnetization behavior of superparamagnetic nanoparticles can be influenced by anisotropic factors such as shape, stress, exchange, and crystal anisotropy. Shape anisotropy and crystal anisotropy are the two most common anisotropy effects and will be briefly overviewed in the following sections. For detailed development on superparmagnetism, please refer to classic reviews by Bean and Livingston[16] as well as Jacob and Bean.[17]

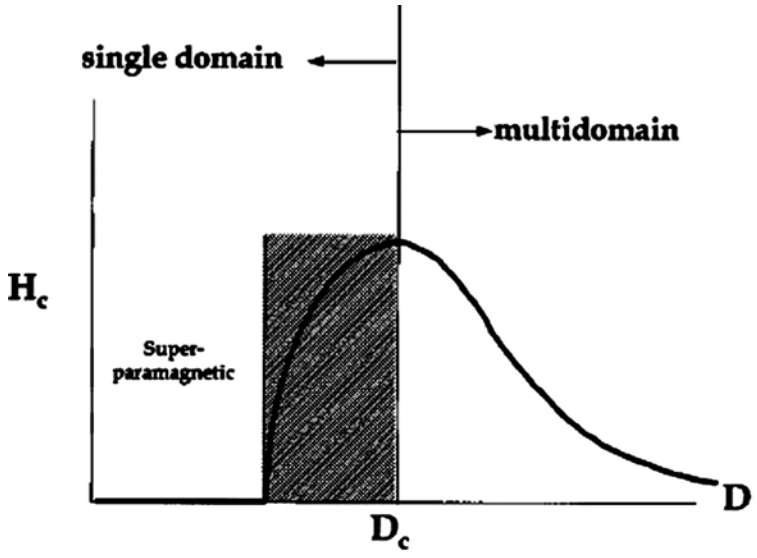

Figure 1.6 Correlation between particle size and domain classification and coercitivity.[4]

1.3.3 Stoner-Wohlfarth Theory and Néel Theory

One of the most recognized theories describing the assembly of non-interacting single domain magnetic nanoparticles with uniaxial anisotropy is the Stoner-Wohlfarth theory.[18] The simplest form to represent the energy barrier for magnetization reversal in single domain magnetic nanoparticles is by

$$E_A = KV \sin^2\theta \tag{1.8}$$

where E_A is the activation energy, K is the magnetic anisotropy of the nanoparticle, V is the volume of the nanoparticle, and θ is the angle between the easy axis and the moment of the nanoparticle.[18] Schematically, we can picture the E_A as the activation barrier in a potential well where the reversal of the moments requires overcoming the E_A with each minima (there are multiple) corresponding to different crystallographic directions (Figure 1.7).

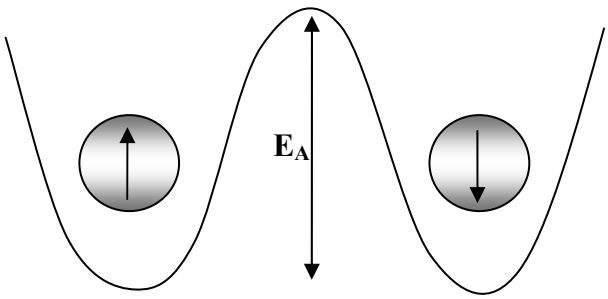

Figure 1.7 Schematic representation of energy barrier for magnetization reversal.

In 1949, Néel theorized that there is a time dependence on the reversal of magnetization.[19] This magnetic behavior is dependent on the relaxation time (τ) of the system and is given by equation 1.9

$$\tau = \tau_o \exp [KV/(k_BT)] \quad (1.9)$$

where τ_o is the frequency for magnetization vectors to flip, k_B is the Boltzmann's constant, and T is the temperature.[19] Although factors such as temperature, saturation magnetization, applied magnetic field, and volume of the particle can all affect τ_o, they are usually constant and are in the order of $10^{-9} – 10^{-13}$.[20-23] Relating this concept back to superparamagnetism, if the measurement time is shorter than τ then moments are blocked but if the measurement time is longer thanτ, moments are no longer blocked and particles become superparamagnetic. As an example, taking an arbitrary measurement time of 100s and $\tau_o = 10^{-9}$s, the condition for superparamagnetism becomes:

$$KV = k_BT \quad (1.10)$$

with $KV = 25\ k_BT$ for superparamagnetic conditions. When thermal energy is greater than E_A, coherent magnetization reversal occurs and the moments fluctuate to random crystallographic axes leading to paramagnetic behavior. Since each moment in superparamagnetic nanoparticles is coupled to many others, the moment per particle is much greater than that in paramagnetic materials where there is one single moment per atom.

1.3.4 Anisotropy

As previously mentioned, two common anisotropy factors that influence the magnetic behavior of superparamagnetic nanoparticles are shape anisotropy and crystallographic anisotropy.[4] Shape anisotropy arises from magnetostatic effects. It is predicted to produce large coercive forces and can affect the demagnetization energy, E_d (see equation 1.12)

$$E_d = K_f \sin^2\theta + (1/2)N_i\mu_o M_s^2 \qquad (1.12)$$

where the shape anisotropy, K_f, varies depending on shape ($K_f = \mu_o M_s^2/4$ for infinite wire but $K_f = \mu_o M_s^2/2$ for infinite disks).[24] For example, coercitivity increases by as much as four times when a spherical shape is deviated at aspect ratio of 0.4 in single domain Fe nanoparticles. Contrary to shape anisotropy, magnetocrystalline anisotropy is intrinsic to the material and is independent to the shape of the particle. Crystalline anisotropy or magnetocrystalline anisotropy comes from spin-orbit coupling and determines the magnetic orientation of the material.[24,25] Magnetocrystalline anisotropy is important because it determines whether a material correlates well to an application. Hard magnetic materials have very high coercitivity (1-5T)[26] to prevent reversal of magnetization with magnetic field. Since the coercitivity is proportional to the anisotropy constant,[18] a material with high magnetocrystalline anisotropy is attractive to applications utilizing hard magnets.

1.4 Applications

1.4.1 Ferrofluids

Many well known applications associated with magnetic nanoparticles are in ferrofluids. Basically, ferrofluids are magnetic fluids made up of small magnetic nanoparticles (mean diameter of 10nm) in a carrier liquid.[1,13] Magnetic nanoparticles in ferrofluids are superparamagnetic and the magnetic force is proportional to the magnetization [27]of the fluid. Therefore, even weak applied magnetic fields (order of a few mT) induce strong forces on ferrofluids. It is the combination of superparamagnetic behavior and normal liquid behavior that has led to their popularity.

There are thousands of applied and approved patents for applications of magnetic nanoparticles. The most recognized application is using ferrofluids in dampening devices. For example, the voice coils of loud speakers are often damaged through overheating as they oscillate between the poles of a circular magnet. Ferrofluids are filled in the gap of the permanent magnets of loud speakers, allowing the heat produced by the voice coil to be transmitted with an enhanced cooling rate (factor of 3).[27] They have also been used in inertia dampeners such as stepper motors where the ferrofluid acts to provide torque opposing the stepper motor to prevent "ringing".[27] Another popular application of ferrofluids is in sealing technology. They are used as exclusion seals for computer disk drives.[28] There, ferrofluids are used between the magnet and the highly permeable rotating shaft.[27,28] They are held in place by the magnetic field and the concentrated magnetic flux increases the magnetic field thereby, increasing the pressure capacity.

Ferrofluids have also worked their way into optical applications such as optical switches and shutters though there is a lot of room for improvement. In the realm of biology and biomedicine, ferrofluids have also established a place for their application. A more elaborate discussion of the biomedical applications of ferrofluids can be found in section 1.4.3.

1.4.2 Data storage

On September 13th, 1956, IBM introduced the 305 RAMAC (Random Acess Method of Accounting and Control) computer that had a magnetic storage that replaced magnetic drums and Edison cylinders.[29,30] The initiative was to maximize storage and minimize size. Compared to the standards of today, the magnetic storage capacity of 305 RAMAC (4.4MB; areal density of 2 kbits/in^2)[31] is miniscule. Since then, there has been a steady increase in storage capacity and decrease in physical size (Figure 1.8).[29,30]

By using CoPtCr granular media, an areal density in the order of ~40Gbit/in^2 can be achieved. The goal for future growth is to get to an areal density of one or greater than one terabit/in^2.[32,33] To do so, the size of the magnetic nanoparticles used have to decrease. From the Stoner-Wohlfarth theory (see section 1.3.3), when the anisotropy energy decreases, a reversal of magnetization occurs. So when the particle size decreases, thereby decreasing the sample volume, thermal activation can overcome the anisotropy barrier causing random magnetization directions. This becomes problematic because it essentially means that data will be lost due to heat and vibration. To resolve the limitation established by superparmagnetism, IBM has developed an atiferromagnetically coupled

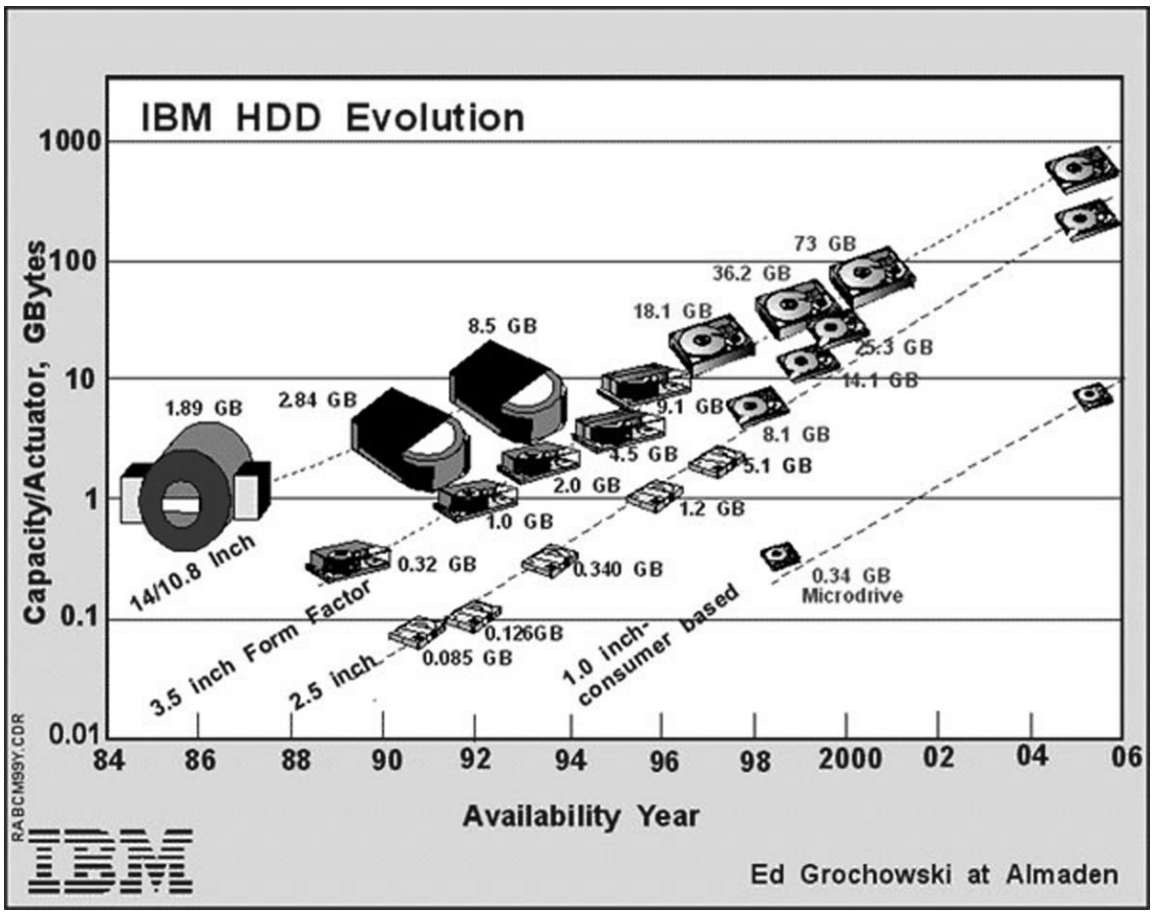

Figure 1.8 Diagram showing the steady increase in storage capacity and decrease in physical size hard disk drives after the commercialization of 305 RAMAC.[29]

(AFC) magnetic media that delays the effects of superparamagnetism allowing for storage of 100Gbit/in^2 and possibly more.[34,35] Basically, in an AFC media, the magnetic layers are separated by a non-magnetic (ruthenium) layer that is approximately 3 atomic layers thin. This allows the magnetic layers to couple antiparallel to each other at significantly higher magnetic densities by increasing the signal to noise ratio in transition regions. Although this is an improvement, the ruthenium layer is deposited with sputtering techniques and nanoparticles are not used. By using magnetic nanoparticles, with larger magnetocrystalline anisotropy, it has been estimated that the storage capacity

can increase by ten-fold relative to AFC media.[34,35] Hence, it is an open ended research field.

1.4.3 Magnetic Resonance Imaging (MRI) Contrast Enhancement

Magnetic Resonance Imaging (MRI) is a powerful technique that images the human body based on the principles of nuclear magnetic resonance.[36-38] It is the result of the difference in signal intensity that each tissue produces in response to a radio frequency pulse.[39-41] First, a strong magnetic field is used to partially polarize the moments of protons. A radio frequency (RF) pulse is then applied to alter the steady state orientation of the protons. During the RF pulse, some of the RF photons are absorbed by the protons causing them to flip from parallel to being antiparallel (higher energy state) to the magnetic field. At the end of the pulse, the relaxation of the protons back to a lower energetic state produces small amounts of electromagnetic radiation and this signal is then registered with the detection coils and converted into an image. The factors that govern MRI are basically proton density and the magnetic relaxation times.

There are approximately 6.6×10^{19} protons in a cubic centimeter of water and in the absence of a strong magnetic field, the moments are randomly oriented. However, when a strong magnetic field is applied, the moments will try to align with the field direction and to do so they will have to overcome the thermal factor that facilitates their random orientation. Though the number of moments that align with the field is only slightly higher than those that are opposite in direction, there is an imbalance of about 2

x 10^{14} protons per cubic millimeter of water. In MRI, the imbalance of proton density is detected and mapped into an image.

The two relaxation time constants associated with MRI, longitudal (T_1) and transverse (T_2).[40,41] The longitudal relaxation or spin-lattice relaxation time constant refers to the loss of energy to the "lattice" or the surrounding that results from the relaxation of proton nuclei to the lowest energy state. Basically, T_1 defines the z-axis.[40] Since the magnetic potential energy is proportional to projection of this axis, a change in magnetization implies that the spin has interacted with its surroundings. Hence T_1 can be considered to be a measure of the dipolar coupling of proton moments to their lattice. The transverse relaxation or spin-spin relaxation time constant refers to the effect in the relaxation process due to dephasing of the individual protons caused by a non-stationary magnetic field.[40] Each proton will experience the external, stationary magnetic field (B_0) along with magnetic field of neighboring protons. Since the angular frequency of a proton is proportional to the experienced magnetic field, the protons will precess at incoherent frequencies. When the protons precess at different frequencies it results in a net decrease of magnetic moment in the xy-plane with time. The time period from maximum value to zero is characterized by T_2.

The quality of the magnetic resonance image can be enhanced by contrast agents. The principle behind contrast agents is how they alter the T_1 and T_2 constants. By decreasing T_1, the signal is essentially amplified. By decreasing T_2, broader lines are generated but at decreased signal amplitudes. Most contrast agents are paramagnetic species with unpaired electrons that can affect T_1 and T_2. Contrast agents can be simple molecular oxygen, stable radicals or metal ions. Since radicals may cause damage to

tissues in general and that the paramagnetic effect of oxygen is weak, metal ions are the best options. The first proposed contrast enhancement agent was Chromium-EDTA but their long term stability prevented their use in clinical applications.[42] Although gadolinium – diethylenetriaminepentaacetic acid (Gd-DPTA)[43] has been approved by the US FDA and is currently marketed as Magnetvist, another class of contrast agents has demonstrated equivalent if not better enhancement to MR images. This other class of contrast enhancement agents belongs to the superparamagnetic family. Since superparamagnetic species do not have a hysteresis above their blocking temperature and behave like paramagnetic nanoparticles above their blocking temperature, they are attractive enhancement agents that do not leave remenance magnetization when the magnetic field is terminated.[40] In addition, their relaxation time is very high compared to paramagnetic species like Gd-DTPA. In fact, the most commonly used contrast enhancement agents now are superparamagnetic iron oxide nanoparticles. For example, Feridex I. V, marketed by advanced Magnetics Inc., is used to image liver or gallbladder disorders. Another marketed iron oxide contrast agent is Resovit®, used in imaging and detection of tumors.

1.4.4 Magnetic Hyperthermia

Hyperthermia is basically a heat treatment that induces necrosis or promotes adoptosis.[44] It can be considered a co-treatment, i.e. treatment in conjunction with other therapy or it can be considered a stand alone treatment. There are several modes of hyperthermia, radiofrequency capacitance hyperthermia (RFCH), microwave antennae

hyperthermia (MH), whole body hyperthermia (WBH), isolated hepatic perfusion hyperthermia (IHPH), and magnetic mediated hyperthermia (MMH).[45] Generally, the process involves heating tissues or cells above the therapeutic threshold temperature (42-46°C) for 30 minutes. However, all but MMH can risk necrosis to healthy tissues due to non-specific targeting abilities. Other techniques such as radiofrequency probe (RFP), microwave probe (MP), interstitial laser photocoagulation (ILP), and direct injection of hot water to tumors are specific targeting methods but require multiple repositioning due to limited heat diffusion.[45] The most promising hyperthermia treatment is with magnetic mediated hyperthermia.

Magnetic mediated hyperthermia was first addressed by Gilchrist, et al. in 1957 to treat lymphatic metastases of large bowel cancers.[46] The concept encompasses using a magnetic field to localize γ-Fe_2O_3 ferromagnetic nanoparticles within the target region and maintaining the field for a specified duration. They found that within 3 minutes at 200-240 Oe field strength, the lymph node tissue heated up to 14°C. Two years later, they demonstrated that by increasing the field strength to 470 Oe, total necrosis of the lymph node was accomplished. Since then, numerous studies have been published using different nanoparticles for MMH as well as different methods of delivery. Currently, most of the magnetic nanoparticles used for hyperthermia are superparamagnetic since they can generate more heat at lower magnetic fields than ferromagnetic nanoparticles.[40,45] The heating mechanism of ferromagnetic nanoparticles and superparamagnetic nanoparticles is reviewed elsewhere.[40,47]

1.4.5 Magnetic Separation

In biomedicinal studies, evaluating biological entities outside of their native environment can be important**.** Most of the time this is accomplished through multiple extractions and centrifugation processes. In the process, the concentration of targeted sample may be reduced from its actual concentration. A more efficient method is to use magnetic separation. Using the abundant linker groups commercially available, magnetic nanoparticles can be coupled to effectors or macromolecules. The resulting magnetic nanoparticle – macromolecule complex can then be separated magnetically or used to recognize counterparts then separated magnetically. For example, Pel Freez had developed a dextran-coated magnetic nanoparticle (magnetite) conjugated to a tetrameric antibody that recognizes dextran at one end and surface antigens on the cell at the other terminus.[48] With a weak magnetic field, cells recognized by this dextran coated magnetite – tetrameric antibody complex can be isolated from a mixture of cells without the complimentary antigen. Additionally, magnetic separation has been adapted for erythrocyte separation and quantification. In normal red blood cells, the organization of phosphatidylserine is oriented in such a way that it faces the cytoplasm. In damaged red blood cells, this organization is random and the distribution of phosphatidylserine is asymmetric.[49] An intracellular protein, Annexin V, has the capability to specifically bind to phosphatidylserine in the presence of Ca^{2+}. Hence, when coupled to magnetic nanoparticles, it provides a way to separate the damaged red blood cells from the normal red blood cells for further quantification. This is an important aspect since the number of damaged red blood cells has correlations to erythrocyte evolution in patients with

malaria and Alzheimer's disease.[50] Quantification of damaged red blood cells is also a marker for the quality of stored human blood in blood banks. The coupling of Annexin V to magnetic nanoparticles has demonstrated such promising applications that it has been patented and is being evaluated for market manufacture.[51] However, there are many more applications that can be associated with magnetic separation of macromolecules. For example, coupling magnetic nanoparticles with effectors that recognize unusual membrane modifications may provide information such as apoptosis and membrane organization that are all important to cancer research.[52]

1.4.6 Drug Delivery

When surgical removal of malignant tumors is not an option, chemotherapy and radiation are generally the choice of treatment for many patients. However, many of the side effects associated with chemotherapy and high dosage therapeutic drugs have introduced more complicated matters. Radiation therapy is not target specific therefore, destroying healthy cells along with cancerous cells. When cancer has spread throughout the body, other treatments such as chemotherapy are used. The main function of most chemotherapeutic reagents is to target and destroy cells that proliferate at an abnormally high frequency. Malignant cells proliferate at high frequency as well as hair follicle cells. With the non-specificity of chemotherapy, many patients will lose their hair on their head, lose their eyebrow, and even eye lashes. Another example is with patients that suffer from chronic inflammation. Many times, the treatment involves high dosages of therapeutic reagents. As the therapeutic reagent circulates through the body, the efficacy

of the drug is dramatically reduced. The side effects and reduced effectiveness of therapeutic reagents is attributed to the non-specific recognition of the therapeutic reagent.

To reduce side effects and maximize drug effectiveness, scientists have proposed the use of magnetic nanoparticles as carriers for therapeutic reagents. For example, Widder, et al. demonstrated that by administering magnetic carriers – doxorubicin (cytotoxic drug) to sarcoma tumors in rat tails, total remission occurred [53]non-magnetically did not show remission.[54] This concept has also been adapted by private companies such as FeRx, who have entered clinical phase II and III studies. Pending funding, this type of treatment may be the alternative to radiation and traditional chemotherapy to humans. The point is to be able to guide or localize the therapeutic reagent once in the system with a magnetic field. This prevents or reduces the amount of therapeutic reagent lost during circulation and localizes the treatment to a specified region.

1.5 Outlook of Magnetic Nanoparticles in Biology

The concept of using magnetic manipulation system for minimal invasive medical and biologically related applications has been around since the 1950s[55-59] and will continue to progress. There are many underlying issues that must be resolved and optimized. For example, magnetic carriers carrying therapeutic drugs are often administered intravenously or intra-arterially. Hence, factors such as the blood flow rate, magnetic nanoparticle concentration, circulation time, and tissue depth will all play a

major role in the development of future magnetic carriers. Another important factor is aggregation. It is extremely important that the intrinsic attraction of the magnetic nanoparticles do not form aggregates or the possibility of clotting may occur. Although there are mathematical models of hydrodynamics involved[60] as well as models for safe target specific treatment[61], none addresses all of the issues. Hence, there is ample room for improvement.

In MRI, novel magnetic nanoparticles with characteristics that will enhance the T_1 to T_2 ratio can further enhance the contrast during imaging. In drug delivery, different approaches of coupling therapeutic reagents to magnetic nanoparticles as well as the development of systems that will allow these conjugates to be safely administered *in vivo* will need to be optimized. With the expanding variety of magnetic nanoparticles and the versatility of its intrinsic properties with change in composition and size, magnetic nanoparticles can be tailored for specific functions and play a major role in magnetically localized therapeutic treatments.

1.6 References

(1) Livingston, J. D. *Driving Forces: The Natural Magic of Magnets*; Harvard University Press: Cambridge, 1996.

(2) http://www.tcd.ie/Physics/Schools/what/materials/magnetism/top.html.

(3) Frei, E. H.; Shtrikman, S.; Treves, D. *Phys. Rev.* **1957**, *106*, 446.

(4) Leslie-Pelecky, D. L.; Rieke, R. D. *Chem. Mater.* **1996**, *8*, 1770.

(5) Jiles, D. *Introduction to Magnetism and Magnetic Materials*; 2nd ed.; St. Edmundsbury Press: Suffolk, 1991.

(6) Cullity, B. D. *Introduction to Magnetic Materials*; Addison-Wesley Publishing Company: Menlo Park, 1972.

(7) http://www.geo.umn.edu/orgs/irm/hg2m/hg2m_index.html, 1991.

(8) Jakubovics, J. P. *Magnetism and Magnetic Materials*; Institute of Metals: London, 1987.

(9) http://www.aacg.bham.ac.uk/.

(10) Morrish, A. H. *The Physical Principles of Magnetism*; IEEE Press: New York, 2001.

(11) Kittel, C. *Phys. Rev.* **1946**, *10*, 965.

(12) Frenkel, J.; Dorman, J. *Nature* **1930**, *126*, 274.

(13) O'Handley, R. C. *Modern Magnetic Materials: Principles and Applications*; Wiley & Sons, Inc.: New York, 2000.

(14) Vestal, C. R. In *Chemistry and Biochemistry*; Georgia Institute of Technology: Atlanta, 2004.

(15) Bean, C. P. *J. Appl. Phys.* **1955**, *26*, 1381.

(16) Bean, C. P.; Livingston, J. D. *J. Appl. Phys.* **1959**, *30*, 1205.

(17) Jacobs, I. S.; Bean, C. P. In *Magnetism*; Rado, G. T. S., H.. Ed.; Academic Press: New York, 1963; Vol. III.

(18) Stoner, E. C.; Wohlfarth, E. P. *Philosophical Transaction of the Royal Society A* **1948**, *240*, 599.

(19) Neel, L. *Ann. Geophys (C. N. R. S.)* **1949**, *5*, 99.

(20) Dormann, J. L.; Fiorani, D.; Tholence, J. L.; Sella, C. *J. Magn. Magn. Mater.* **1983**, *35*, 117.

(21) Aharoni, A. In *Magnetic Properties of Fine Particles*; Dorman, J. L., Ed.; Elsevier Science Publishers: Amsterdam, 1992, p 3.

(22) Rondinone, A. J.; Liu, C.; Zhang, Z. J. *J. Phys. Chem.* **2001**, *105*, 7967.

(23) Rondinone, A. J.; Samia, A. C. S.; Zhang, Z. J. *Appl. Phys. Lett.* **2000**, *76*, 3624.

(24) Solzi, M. In *Fundamental Properties of Nanostructured Materials*; Fiorani, D. S., G., Ed.; World Scientific: River Edge, 1994.

(25) West, A. R. *Basic Solid Sate Chemistry*; 2nd ed.; John Wiley & Sons LTD: Chichester, 1999.

(26) Givord, D. *Europhysics News* **2003**, *34*, 219.

(27) Popplewell, J. *Phys. Technol.* **1984**, *15*, 1650.

(28) Raj, K.; Moskowtiz, R. *J. Magn. Magn. Mater.* **1990**, *85*, 233.

(29) http://www.pcguide.com/ref/hdd/hist-c.html, 2004; Vol. 1997-2004.

(30) Hayes, B. *American Scientist* **2002**, *90*, 212.

(31) Moser, A.; Takano, K.; Margulies, D. T.; Albrecht, M.; Sonobe, Y.; Ikeda, Y.; Sun, S.; Fullerton, E. E. *J. Phys. D: Applied Physics* **2002**, *35*, R157.

(32) Thompson, D.; Best, J. S. *IBM J. Res. Develop.* **2000**, *44*, 311.

(33) http://www.ibm.com.

(34) Fullerton, E. E.; Marguilies, D. T.; Schabes, M. E.; Carey, M.; Gumey, B.; Moser, A.; Best, M.; Zeltzer, G.; Rubin, K.; Doemer, M. *Appl. Phys. Lett.* **2000**, *77*, 3806.

(35) Lohau, J.; Moser, A.; Margulies, D. T.; Fulleron, E. E.; Schabes, M. E. *Appl. Phys. Lett.* **2001**, *78*, 2748.

(36) Wong, W. S.; Tsukuda, J. S.; Kortman, K. E.; Bradley, W. G. *Practical Magnetic Resonance Imaging: A Case Study Approach*; Aspen Publishers, Inc.: New York, 1987.

(37) Wehril, F. W.; McFall, J.; Newton, T. H.; Potts, D. G., Eds. *Advanced Imaging Techniques*; Clavadel Press: San Francisco, 1983; Vol. 2.

(38) Bradley, W. G. *Noninvasive Medical Imaging* **1984**, *1*, 193.

(39) Weitschies, W.; Philipp, K.; Kotitz, R.; Romanus, E.; Weber, P. *Proc. 2nd World Meeting APGI/APV* **1998**, 1145.

(40) Pankhurst, Q. A.; Connolly, J.; Joes, S. K.; Dobson, J. *J. Phys. D: Applied Physics* **2003**, *36*, R167.

(41) Bulte, J. W. M.; Cuyper, M. D.; Despres, D.; Frank, J. A. *J. Magn. Res. Imaging* **1999**, *9*, 329.

(42) Runge, V. M.; Clanton, J. A.; Lukehart, C. M. *A. J. R.* **1983**, *141*, 1209.

(43) Krasnow, N. *Biochem. Biophys. Acta* **1972**, *282*, 187.

(44) Rabine, Y.; EurekAlert, 2002.

(45) Moroz, P.; Jones, S. K.; Gray, B. N. *Int. J. Hyperthermia* **2002**, *18*, 267.

(46) Gilchrist, R. K.; Medal, R.; Shorey, W. D.; Hanselman, R. C.; Parrott, J. C.; Taylor, C. B. *Ann. Surg.* **1957**, *146*, 596.

(47) Rosenweig, R. E. *J. Magn. Magn. Mater.* **2002**, *252*, 370.

(48) www.Pel-Freez.com

(49) Bacri, J. C.; da Silva, R.; Perzynski, J. N.; Pons, A. A.; Rogers, D.; Sabolovi, D.; Halbreich, A. *Scientific and Clinical Applications of Magnetic Carriers: An Overview*; Plenum Publishing Corp.: New York, 1997.

(50) Sabolovic, D.; Roudier, M.; Boynard, M.; Pautou, C.; Sestier, C.; Fertil, B.; Geldwerth, J. R.; Pons, J. N.; Amri, A.; Halbreich, A. *J. Ger. Biol. Sci.* **1997**, *52A*, B217.

(51) Bee, A.; Boucharmi, T.; Brossel, R.; Cabuil, V.; Carpentier, M.; Fruchart, J. M.; Massart, R.; Neveu, S.; Pons, J. N.; Robineau, M.; Roger, J. In *EPC*: France, 1990.

(52) Roger, J.; Pons, J. N.; Massart, R.; Halbreich, A.; Bacri, A. *Eur. Phys. J. AP* **1999**, *5*, 321.

(53) Landwehr, G.; Dietrich, H.; Weber, H.; Bushmann, W.; Neubauer, H. *Opthamlic Res.* **1977**, *9*, 308.

(54) Widder, K. J.; Morris, R. M.; Poore, G. A.; Howard, D. P.; Senyei, A. E. *Eur. J. Cancer Clin. Oncol.* **1983**, *19*, 135.

(55) McCaslin, M. F. *Trans. Am. Opthalmol. Soc.* **1958**, *56*, 571.

(56) Tillander, H. *Acta. Radiol.* **1956**, *45*, 21.

(57) Tillander, H. *Acta. Radiol.* **1951**, *35*, 62.

(58) Devine, J. W.; Devine Jr., J. W. *Surgery* **1953**, *33*, 513.

(59) Gillies, G. T.; Ritter, R. C.; Broaddus, W. C.; Grady, M. S.; Howard III, M. A.; McNeil, R. G. *Rev. Sci. Instrum.* **1994**, *65*, 533.

(60) Cummings, L. J.; Richardson, G.; Hazelwood, L. *Proc. Mathematics in Medicine Study Group* **2000**, *1*, 69.

(61) Gallo, J. M.; Hafeli, U. *Cancer Res.* **1997**, *57*, 3063.

CHAPTER II

SPINEL FERRITES AND SYNTHESIS METHODS OF MAGNETIC NANOPARTICLES

2.1 Spinel Ferrites

The term spinel is named after the mineral, $MgAl_2O_4$. It has a general chemical formula of $A^{II}B_2{}^{III}O_4$, where A is a divalent cation (M^{2+}) and B is a trivalent cation (M^{3+}) (Figure 2.1).[1] There are two categories of spinel phases, normal and inverse spinels. In normal spinels, the A sites are tetrahedrally coordinated and the B sites are octahedrally coordinated. In reverse spinels, half of the tetrahedral sites are occupied by B^{II} and half by B^{III}. All of the octahedral sites of an inverse spinel are occupied by A^{III}. When M^{2+} and M^{3+} cations both occupy A and B sites, the system is a mixed spinel. The lattice characteristics of a spinel include a FCC site for the oxygen atoms and two cationic sites occupying the tetrahedral and octahedral interstices.[1-4] In a spinel, there are 64 tetrahedral sites, 32 octahedral sites, and 32 oxygen sites in a unit cell. Due to their exchange coupling, spinel ferrites are ferrimagnetically aligned where all of the moments of A sites

are aligned parallel with respect to one another (likewise moment alignment for B sites with respect to one another) while moments of A and B sites are antiparallel to each other.

The magnetic properties of spinel ferrites are greatly influenced by composition and cation distribution. Variation of the cation distribution between the cationic sites leads to different magnetic properties even if the composition of the spinel is the same. For example, a blocking temperature change of as much as 50°C has been observed in $MnFe_2O_4$ nanoparticles with a 29% inversion in distribution of cations.[2] When comparing similar systems with different composition such as $CoFe_2O_4$ and $MgFe_2O_4$, there is always a large difference in the blocking temperature (~150K) that can be attributed to the spin-orbital coupling of the cations as well as superparamagnetic properties. While there are three unpaired *d* electrons present in Co^{2+}, all of the electrons are paired in Mg^{2+}. So while Co^{2+} cations have a large spin-orbital coupling, the paired electrons of Mg^{2+} does not provide any contribution to the electron spin. Magnetocrystalline anisotropy arises from spin – orbit coupling.[5-7] If we relate the spin – orbit coupling factor to the Stoner – Wohlfarth theory, there would be an increased energy barrier. As a result, a larger blocking temperature is required to overcome this large anisotropy energy barrier. Hence, the influence of cation distribution and chemical composition can greatly influence the tunability of the magnetic properties of spinel ferrites.

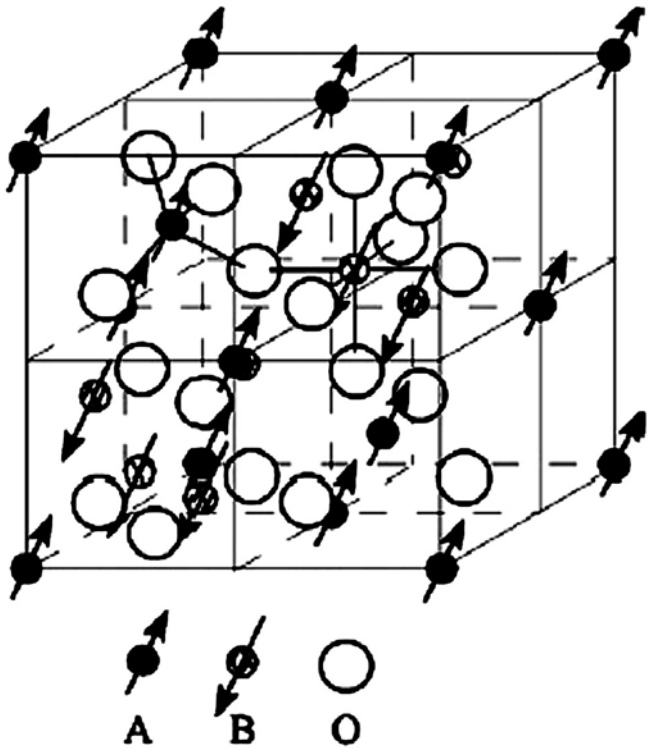

Figure 2.1 Partial unit cell structure of a typical spinel ferrite.[4]

2.2 Synthesis Methods of Magnetic Nanoparticles

2.2.1 Ball Milling

Ball milling is a mechanical alloying method used to manufacture oxide dispersion that are used to strengthen alloys.[8] The process involves vigorous mixing of the powder starting material and milling balls in a vial for several hours. The vigorous shaking action permits the starting material caught between milling balls to be crushed during collision of the balls. The repetitive collision generates enough energy to produce

non-equilibrated nanostructures, usually in an amorphous or quasi-crystalline state. Recently, this technique has been employed to synthesize magnetic spinel ferrites such as $ZnFe_2O_4$.[9] Although this is a method that can produce large quantities of nanomaterials with cost efficiency, it lacks the ability to produce monodispersed and crystalline magnetic nanoparticles. [10-13]

2.2.2 Sonochemical Method

Sonochemistry uses ultrasound to assist or enhance a chemical reaction. Nanoparticles can be produced using sonochemical methods that involve the process of cavitation.[14,15] Cavitation is best described as the formation, growth, and collapse of bubbles.[14,15] When acoustic waves are introduced in liquids, the decompression cycle of the acoustic waves can generate bubbles. During the decompression or expansion cycle, negative pressure exerted on the liquid pulls molecules apart and eventually exceeds the local tensile strength of the liquid creating a cavity or bubble. Bubbles then grow in the decompression phase by absorbing energy from the acoustic radiation. Once bubbles have grown to a critical size (varies with different liquid), they can no longer efficiently absorb energy and this allows the surrounding liquid to enter the bubble(compression) causing it to implode. During the implosion or collapse of these bubbles, a short-lived (μs) hot spot in the range of 5000°C and several hundred atmospheres can be generated.[14,15] The size of bubbles generated and the cavitation time scale can be best described through Figure 2.2. Through sonochemical methods, ferrites such as $NiFe_2O_4$[16]

and Fe_3O_4[17] have been produced. In most cases, the end product is amorphous and highly aggregated making it difficult to characterize individual particles.[18]

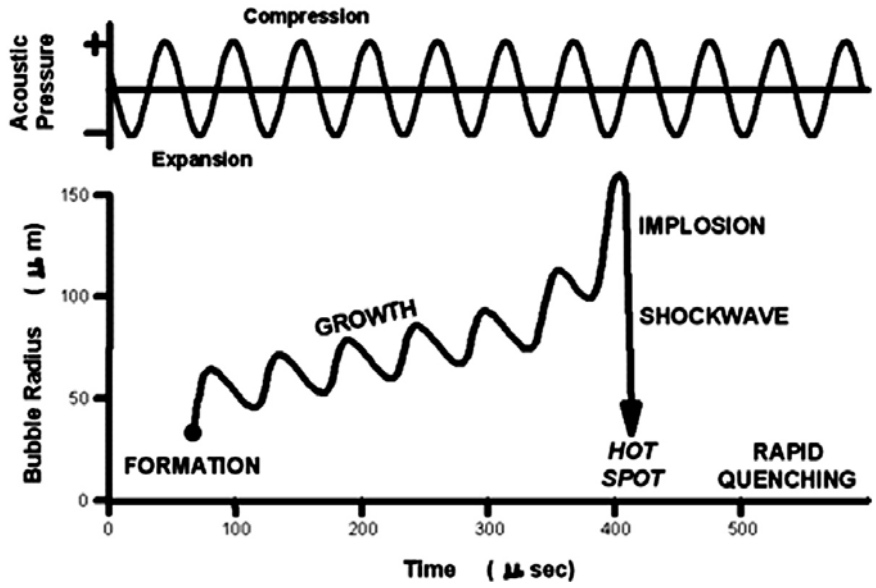

Figure 2.2 Cavitation process.[15]

2.2.3 Sol-gel Method

A sol can be defined as a colloid suspended in a liquid medium whereas a gel is a sol network interconnected to form a rigid framework. Since the colloids that make up the sol are between 1-100nm the gel they make up can have pores from the nanometer to micrometer dimension.[19,20] In addition to being a controllable and practical method to make glasses and ceramics, the mild condition of a sol-gel synthesis allows for the preparation of other unique materials such as films, fibers, coatings, and of particular

interest, nanoparticles (Figure 2.3).[21] For example, terbium doped cobalt spinel ferrite, $CoFe_{2-x}Tb_xO_4$, has been synthesized through a sol-gel process.[22]

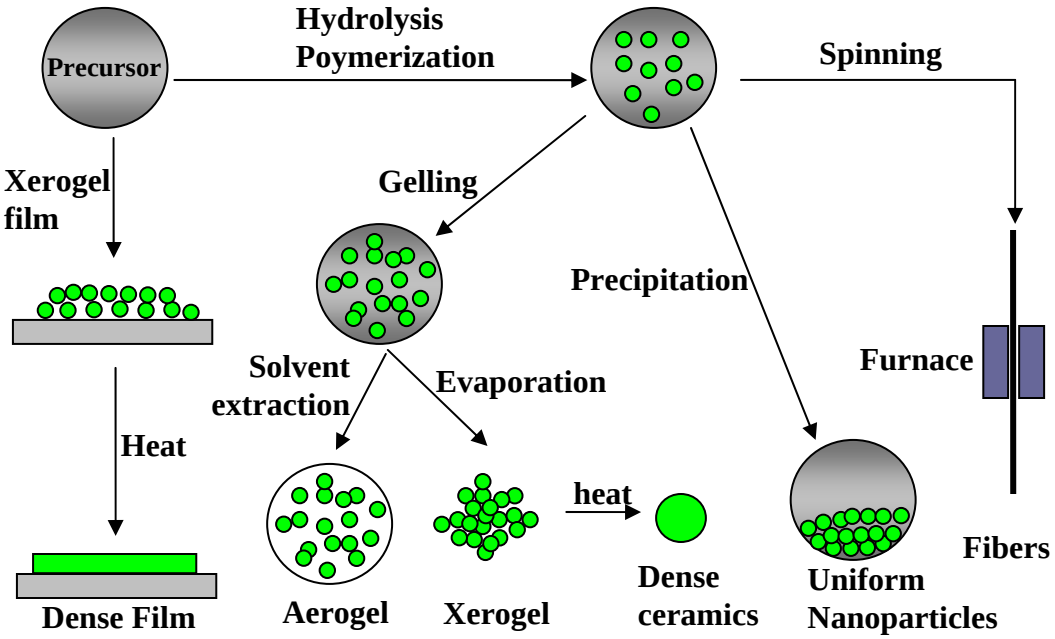

Figure 2.3 Products that can be formed through sol-gel synthesis.

Generally, the sol-gel process is classified as either inorganic based or alkoxide based. The synthesis of materials through a sol-gel process can be described in the following generalized steps. First, a sol is produced by reacting precursors (e.g. $Si(OR)_4$), solvent, and a catalyst. Hydrolysis in an aqueous solution followed by condensation allows a region of crosslinked metal-oxygen-metal (M-O-M) bonds to form a sol.[19] With

time, the sol particles grow into macroparticles and through condensation they form an elastic gel. Through polycondensation, the gel is then aged so that a more rigid framework is developed.[23-25] The gel is then dried by evaporation or through a supercritical drying process.

Although the sol-gel synthetic method can generate uniform nanoparticles, the difference in hydrolysis rates of precursors may result in chemical inhomogeneity and can lead to higher crystalline temperature and undesirable crystalline phases.[21] Depending on the drying method used, cracking of the gel and shrinking of the pores may occur making it difficult to target particle sizes.

2.2.4 Co-precipitation

The co-precipitation process of synthesizing nanoparticles can yield nanoparticles with a wide spectrum of sizes ranging from 5-180nm.[4,26] The process is relatively simple. Inorganic salts are mixed in an aqueous environment then precipitated out with hydroxide base. The resulting precipitate is then digested, filtered, then dried in a furnace. Using this method, magnetic nanoparticles such as magnetite,[27,28] manganese ferrite[2,29], and magnesium ferrites[30,31] have been produced. Parameters such as the ratio of starting materials and the oxidation state of starting materials can make a difference in the size of the resulting nanoparticle. For example, using ferric (Fe^{3+}) salts with other divalent ions can generate particles in the range of 5-25nm.[29] On the otherhand, through an Ostwald ripening process using ferrous salts with an oxidizing reagent, larger magnetic nanoparticles (up to 180nm) can be made.[29]

Although co-precipitation is a simple process, it has disadvantages. When compared to other synthetic methods such as microemulsion methods (see section 2.2.6), the resulting nanoparticle is strongly aggregated.[29,32] The aggregated particles limit further application that will require surface modification. Another disadvantage is the relatively non-uniform and metastable size distribution (especially sizes below 20nm)[33] as well as a mix of magnetic states. Studies have shown magnetite synthesized from co-precipitation methods usually have both clusters that are superparamagnetic and ferromagnetic simultaneously.[32] Following the digestion process, the method calls for heat treatment. The heat treatment itself may affect the size distribution and aggregate the sample.

2.2.5 Microemulsions

The magnetic properties of magnetic nanoparticles can be dramatically affected by the distribution of cations in the tetrahedral and octahedral sites. Thus far, all of the synthetic methods discussed produce amorphous magnetic nanoparticles and will require further heat treatment. Zhang, et al. demonstrated that the size of nanoparticles as well as the cation distribution is affected by high annealing temperatures.[2] Hence, any method that requires heat treatment does not offer size control or cation distribution control. A better method to synthesize nanoparticles is through microemulstion. By definition, a microemulsion is a dispersion of one liquid in another stabilized by an interfacial film of surfactants.[34,35] The dispersion can be classified as water-in-oil (reverse phase) or oil-in-water (normal phase). In both types of microemulsion (see figure 2.4a and 2.4b), the

amount of surfactant used is above their critical micelle concentration (cmc). The aggregation of surfactant forms 10-100nm micelles. Both types of dispersions can generate nanoparticles in the size range of 2-100nm.[36]

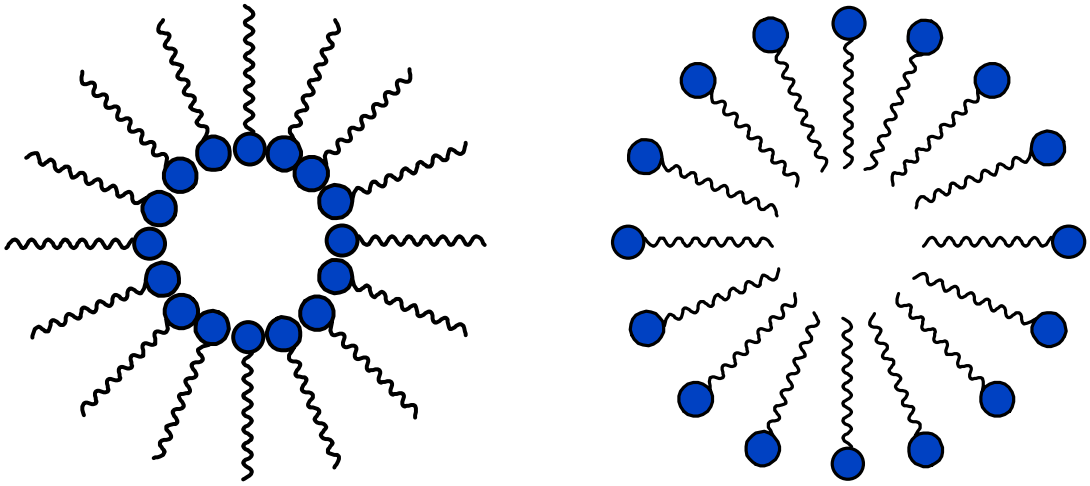

(a) **(b)**

Figure 2.4 General structure of a (a) reverse micelle and (b) normal micelle.

2.2.5.1 Reverse Micelle Method

Reverse micelles are water-in-oil droplets stabilized by surfactant molecules. The polar termni points in towards the hydrophilic interior of the micelle and the oily chains point out (see Figure 2.4a). These micelles are essentially nanoreactors. The reverse

micelle process has been used to make semiconductors with controllable size and high homogeneity as well as magnetic nanoparticles such as Fe_3O_4 and MFe_2O_4 (M = Co, Mg, Mn, Cu).[3,4,35,37-43] This method also allows for doped nanoparticles to form products such as $CoCrFeO_4$.[44] Generally, the process involves mixing divalent salts in a surfactant solution. Toluene or another organic solvent is then slowly added and reverse micelles are allowed to form. Upon complete formation, base is added to the solution to precipitate the particles. The volume is then reduced by refluxing and the particles are isolated through centrifugation. The reverse micelle method in general can produce controllable sizes and homogeneous nanoparticles.

Size control in synthesis of magnetic nanoparticles is an important parameter. The most reported method of varying the size of magnetic nanoparticles is by adjusting the surfactant to water ratio or water to organic solvent ratio to change the droplet size. For example, it has been shown that by adjusting the water to surfactant ratio, different sized $MnFe_2O_4$ can be made. By correlating the droplet size using the general formula of

$$D(nm) = 0.3w \qquad (2.1)$$

where $w = [H_2O]/ [AOT]$, Carpenter et al. were able to make 10nm $MnFe_2O_4$ when w = 10 and 5nm $MnFe_2O_4$ when w = 0.01.[41,43] While equation 2.1 address the Na(AOT)-water-isooctane system, similar principle is applied for other systems. For an example, by using

$$(93-x)/7/x \qquad (2.2)$$

where x corresponds to the cyclohexane/Brij/aqueous iron solution, Lopez-Perez were able to make Fe_3O_4 nanoparticles ranging from 1.9nm-7.3nm.[42] Though many ferrites can be accomplished through normal micelle methods as well, a successful normal micelle synthesis of $CuFe_2O_4$ and $MnFe_2O_4$ has never been reported[4] but can be synthesized through reverse micelle methods.[39]

2.2.5.2 Normal Micelle Method

A general structure of a normal micelle can be seen in Figure2.4b. The hydrophobic organic (oily) chain is directed to the core of the micelle and the polar terminus is oriented towards the outside or the perimeter of the micelle. Normal micelle have been successfully applied to prepare many spinel ferrite systems such as iron oxides, cobalt ferrites, and transition metal or lanthanide doped cobalt ferrites.[39,42,45-48] Generally, metal cations are mixed with a surfactant, typically sodium dodecylsulfate (SDS; $CH_3(CH_2)_{10}CH_2OSO_3^-Na^+$). The metal cations will associate with the polar head groups and above the critical micelle concentration, the surfactant molecules will aggregate to form micelles "confining" the metal cations in solution.[4] The critical micelle concentration for normal micelle synthesis is generally very low relative to co-precipitation methods. Typically it is in the 1.5mM range at room temperature. Nanoparticles are precipitated out with base then isolated through centrifugation then air dried.

Like the reverse micelle method, the normal micelle method offers control in the size of the nanoparticle. In order to vary the size of the particle, adjustments to the surfactant concentration, metal salt concentration, base concentration, and reaction temperature can be made. Rondinone, et al. demonstrated through chemometric modeling , the parameters that will correlate to a size change in $CoFe_2O_4$ nanoparticles.[48] A cross sectional three-dimension plot of the effects of metal salt concentration and base (methylamine) concentration at constant reaction temperature generated a saddle shaped graph (see Figure 2.5) implying a strong interaction between metal ions and base.[48,49] When the plot of the effects of metal salt concentration with varying temperature using a constant concentration of base was generated (Figure 2.6), the curve indicated that the parameters are independent of one another. Therefore, if the reaction temperature is increased at varying concentrations of metal salts, the size of the nanoparticles is increased. Likewise, when the salt concentration is increased at various reaction temperatures, the size of the nanoparticles also increases. Using the factors resolved by Rondinone, et al.[48], the magnetic nanoparticles synthesized in this thesis were all produced from a normal micelle method without any modifications or with slight modifications.

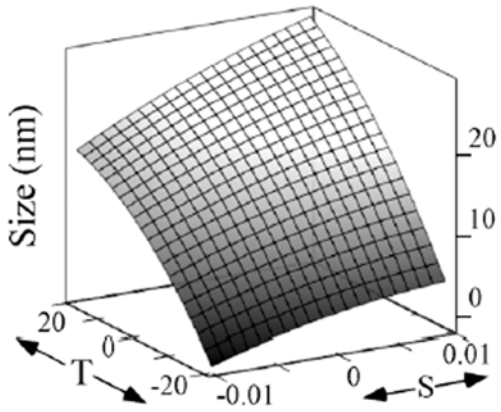

Figure 2.5 Three-dimensional cross section plot illustrating the effects of metal salt concentration [S(M)] and base concentration [A(M)] at constant temperature.[48]

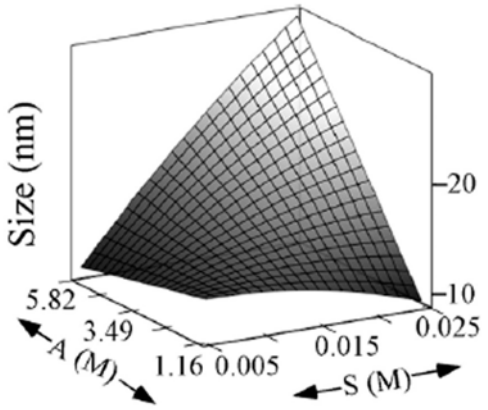

Figure 2.6 Three-dimensional cross section plot illustrating the effects of metal salt concentration [S(M)] and reaction temperature (T) using constant base concentration.[48]

2.2.6 Seed Mediated Thermal Decomposition Method

The drive to attain better control of size distribution and shape of magnetic nanoparticles is an ongoing process. Thus far, synthetic methods such as sol-gel, co-precipitation, and microemulsions have demonstrated their ability to produce nanosized particles with some control. However, none of the methods can provide shape control. Recently, Zhang and Song[50] as well as Sun et al.[33] developed, in parallel and independently, methods to produce magnetic nanoparticles with controllable size and shape. The basic strategy is to synthesize nanoparticles using coordinating metal precursors in a nonhydrolytic process then using the resulting magnetic nanoparticle as a seed for further growth. By adjusting the concentration of the precursor monodispersed nanocrystals of 3-9nm can be produced. Depending on the size of the seed nanoparticle, monodispersed nanocrystals up to 20nm have been synthesized.[33] Since the seed mediated growth takes place above the thermal decomposition temperature, the rate at which the growth occurs is the key factor to the resulting shape of the nanoparticle. For example, at a slow heating rate, a cubic shaped $CoFe_2O_4$ is produced versus a spherical $CoFe_2O_4$ at higher heating rates. The change in shapes has been attributed to the heating rate, availability of metal cations, and selective directional growth.[50]

The applications of monodispersed nanocrystals with controlled shape have strong grounds. It has been implied that MFe_2O_4 (M = Co, Li, Ni, Zn, Fe) can potentially be utilized in high-performance electromagnetic devices, and spintronic devices.[33] In addition, they can improve on many of the bio-applications currently available. To address the bio-applications, the nanocrystals must be hydrophyllic or through surface

modifications be made hydrophilic. It has been shown that through solvent extraction, hydrophobic nanocrystals, Fe_3O_4, can be made hydrophilic.[33] With the current development and future progress, bio-applications with magnetic nanoparticles with controllable size and shape will be possible.

2.2 References

(1) McCurrie, R. A. *Ferromagnetic Materials - Structure and Properties*; Hartcourt Brace and Company: London, 1994.

(2) Zhang, J. Z.; Wang, Z. L.; Chakoumakos, B. C.; Yin, J. S. *J. Am. Chem. Soc.* **1998**, *120*, 1800.

(3) Liu, C.; Zou, B.; Rondinone, A. J.; Zhang, J. Z. *J. Am. Chem. Soc.* **2000**, *122*, 6263.

(4) Vestal, C. R.; Zhang, J. Z. *Int. J. of Nanotechnology* **2004**, *1*, 240.

(5) Solzi, M. In *Fundamental Properties of Nanostructured Materials*; Fiorani, D. S., G., Ed.; World Scientific: River Edge, 1994.

(6) West, A. R. *Basic Solid Sate Chemistry*; 2nd ed.; John Wiley & Sons LTD: Chichester, 1999.

(7) Nedkov, I.; Ausloos, M., Eds. *Nano-crystalline and thin film magnetic oxides*; Kluwer Academic Publishers: Boston, 1999.

(8) Benjamin, J. S. *Metall. Trans.* **1970**, *1*, 2943.

(9) Goya, G. F.; Rechenberg, H. R. *Material Science Forum* **1999**, *302-303*, 406.

(10) Nicoara, G.; Fratiloiu, D.; Nogues, M.; Dormann, J. L.; Vasiliu, F. *Material Science Forum* **1997**, *235*, 145.

(11) Kaczmarek, W. A.; Ninham, B. W. *J. Phys. IV France* **1997**, *7*, C1.

(12) Horvath-Pardavi, M.; Takacs, L. *Scripta Metallurgica et Materialia* **1995**, *33*, 1731.

(13) Goya, G. F.; Rechenberg, H. R. *J. Magn. Magn. Mater.* **1999**, *203*, 141.

(14) Suslick, K. S. *Science* **1990**, *247*, 1439.

(15) Suslick, K. S., Ed. *Ultrasound: Its Chemical, Physical, and Biological Effects*; Wiley-VCH: New York, 1998.

(16) Shafi, K. V. P. M.; Koltypin, Y.; Gedanken, A.; Prozorov, R.; Balogh, J.; Lendvai, J.; Felner, I. *J. Phys. Chem. B* **1997**, *101*, 6409.

(17) Cao, X.; Koltypin, Y.; Katabi, G.; Prozorov, R.; Felner, I.; Gedanken, A. *J. Mater. Chem.* **1997**, *7*, 1007.

(18) Prozorov, T.; Prozorov, R.; Koltypin, Y.; Felner, I.; Gendanken, A. *J. Phys. Chem. B* **1998**, *102*, 10165.

(19) Davis, J. T.; Rideal, E. K. *Interfacial Phenomena*; Academic Press: New York, 1963.

(20) Hench, L. L.; West, J. K. *Chem. Rev.* **1990**, *90*, 33.

(21) Ghosh, N. N.; Pramanik, P. *Materials Science and Engineering C* **2001**, *16*, 113.

(22) Yan, C.; Cheng, F.; Liao, C.; Kuang, J.; Xu, Z.; Chen, L.; Zhao, H.; Liu, Z.; Wang, Y.; Zhu, T.; He, G. *J. Magn. Magn. Mater.* **1999**, *1999*, 396.

(23) Iler, R. K. *The Chemistry of Silica*; Wiley: New York, 1979.

(24) Iler, R. K. *Silica Chemistry*; American Chemical Society: Washington, D. C., 1982.

(25) Iler, R. K. In *Science of Ceramic Chemical Processing*; Hench, L. L., Ulrich, D. R., Ed.; Wiley: New York, 1986.

(26) Beck, H. P.; Eiser, W.; Haberkorn, R. *J. European Ceramic Soc.* **2001**, *21*, 687.

(27) Massart, R. *IEEE Transactions on Magnetics* **1981**, *Mag-17*, 1247.

(28) Papell, S. S.; Faber, O. C. *NASA Technical Note* **1968**, *NASA-TN-D-4676*, 25.

(29) Tang, Z. X.; Sorensen, C. M.; Klabunde, K. J.; Hadjipanayis, G. C. *J. Colloid Interface Sci.* **1991**, *146*, 38.

(30) Chen, Q.; Rondinone, A. J.; Chakoumakos, B. C.; Zhang, J. Z. *J. Magn. Magn. Mater.* **1999**, *194*, 1.

(31) Chen, Q.; Zhang, J. Z. *Appl. Phys. Lett.* **1998**, *73*, 3156.

(32) Petrera, M.; Gennaro, A.; Burriesci, N. *J. Mat. Sci.* **1982**, *17*, 429.

(33) Sun, S.; Zeng, H.; Robinson, D. B.; Raoux, S.; Rice, P. M.; Wang, S. X.; G., L. *J. Am. Chem. Soc.* **2004**, *126*, 273.

(34) Leung, R.; Hou, M. J.; Manohar, C.; Shah, D. O.; Chung, P. W. In *Macro- and Microemulsions*; Shah, D. O., Ed.; Academic Press: Washington, D. C., 1985.

(35) Pillai, V.; Shah, D. O. *J. Magn. Magn. Mater.* **1996**, *163*, 243.

(36) Sharma, M. K.; Shah, D. O. In *Macro- and Microemulsions*; Shah, D. O., Ed.; Academic Press: Washington, D. C., 1985.

(37) Pileni, M. P. In *Nanoparticles and Nanostructured Films*; Fendler, J. H., Ed.; Wiley: Weinheim, 1997, p 71.

(38) Li, Y.; Park, C. W. *Langmuir* **1999**, *15*, 952.

(39) Liu, C.; Zou, B.; Rondinone, A. J.; Zhang, J. Z. *J. Phys. Chem. B.* **2000**, *104*, 1141.

(40) Moumen, N.; Pileni, M. P. *J. Phys. Chem.* **1996**, *100*, 1867.

(41) Seip, C. T.; Carpenter, E. E.; O'Conner, C. J.; John, V. T. L., S. *IEEE Trans. Magn.* **1998**, *34*, 1111.

(42) Lopez-Perez, J. A.; Lopez-Quintela, M. A.; Mira, J.; Rivas, J.; Charles, S. W. *J. Phys. Chem. B* **1997**, *101*, 8045.

(43) Carpenter, E. E.; O'Conner, C. J.; Harris, V. J. *J. Appl. Phys.* **1999**, *85*, 5175.

(44) Vestal, C. R.; Zhang, J. Z. *Chem. Mater.* **2002**, *14*, 3817.

(45) Feltin, N.; Pilieni, M. P. *Langmuir* **1997**, *13*, 3927.

(46) Kahn, M. L.; Zhang, J. Z. *Appl. Phys. Lett.* **2001**, *78*, 3651.

(47) Moumen, N.; Veillet, P.; Pileni, M. P. *J. Magn. Magn. Mater.* **1995**, *149*, 67.

(48) Rondinone, A. J.; Samia, A. C. S.; Zhang, Z. J. *J. Phys. Chem. B.* **2000**, *104*, 7919.

(49) Samia, A. C. S. In *Chemistry and Biochemistry*; Georgia Institute of Technology: Atlanta, 2002.

(50) Song, Q.; Zhang, Z. J. *J. Am. Chem. Soc.* **2004**, *126*, 6164.

CHAPTER III

INSTRUMENTATION AND RELATED TECHNIQUES

3.1 Magnetic and Physical Characterization Instrumentation

3.1.1 Powder X-Ray Diffraction

X-rays, discovered by W. C. Röentegen in 1895, have led to the development of major characterization instrumentation utilizing the principles of the X-ray.[1-5] Three well known categories of instruments are X-ray fluorescence spectrometry, X-ray radiography, and X-ray crystallography. In X-ray fluorescence spectrometry, secondary radiation from materials excited by an X-ray source reveals the amount of a particular element in the material.[4] In X-ray radiography, the relationship between the density of the material and its X-ray absorptivity is revealed.[4,5] The most useful technique to identify the structure and crystallinity of material is through X-ray crystallography.[1,2,4,5] Powder X-ray diffraction (XRD) belongs to the family of X-ray crystallography and although it is an established technique for bulk materials, it is now commonly used to nondestructively

characterize nanostructures such as magnetic nanoparticles. The XRD used throughout this thesis for the characterization of magnetic nanoparticles is a Bruker D8 Advance X-ray diffractomer with CuK_{α} radiation.

To generate X-rays, a current is passed through a conducting wire or filament (tungsten filament) and due to the resistance of the filament, it will heat up. The heat generated is sufficient enough to eject electrons. A potential difference between the anode and the cathode will accelerate the free electrons towards the cathode, a copper target. If there is sufficient energy, the bombarding of electrons onto the anode may knock an outer electron of the anode out of its orbit generating an x-ray radiation.

When X-ray radiation strikes a powder sample, the layers of crystals of the sample act like weak mirrors that "reflect" the x-ray beams. The angle of "reflectance" equals to the angle of incidence for each row of atoms (Figure 3.1.). Interference then occurs between the beams reflecting off different rows of atoms in a crystal.[1,3,4] For constructive interference, the order of interference must be an integer. This results in Bragg's law given in equation 3.1.

$$n\lambda = 2d \sin\theta \quad (n = 1, 2, 3, \ldots.) \tag{3.1}$$

where n is the order of interference, λ is the wavelength of the incident x-ray beam, d is the distance between atomic layers in the crystal, and θ is the angle of incidence.

Data collected from XRD can be used to gather information about phase identification, phase purity, and crystallite size.[1,3,4] Experimental diffraction patterns can be compared to those in the JCPDS (Joint Committee on Powder Diffraction Standard) database for phase identification. The peak broadening of the experimental diffraction peak can also give us information of the diameter of the particle through the Scherrer formula (equation 3.2)

$$B = 0.89\lambda / t \cos\theta \qquad (3.2)$$

where B is the broadening of the XRD peak at full width half maximum, λ is the wavelength of the incident x-ray beam, θ is the diffraction angle, and t is the diameter of the nanoparticle.[1,3,4]

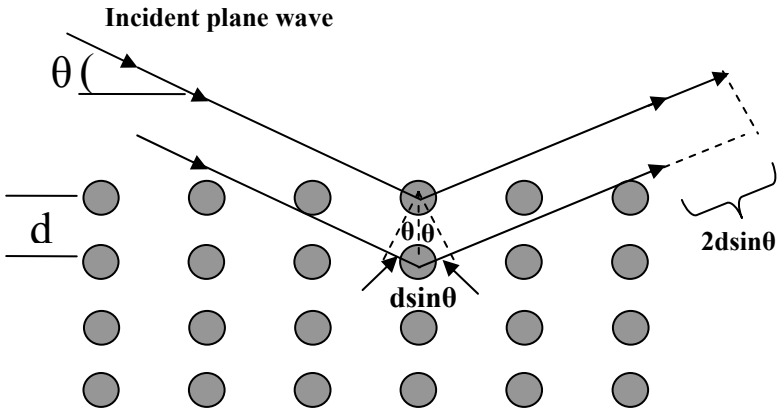

Figure 3.1 Interference between x-ray beams scattering rows of atoms in a crystal. Figure adapted from reference 5.

3.1.2 SQUID Magnetometry

SQUID (Superconducting QUantum Interference Device) magnetometry is governed by two principles, the Josephson's effect and the quantization of magnetic flux of a superconducting ring.[4, 6-10] It is one of the most sensitive instruments available for magnetic measurements yet it can also operate at 10 tesla.[11] The nominal resolution of SQUID is about 1fT and it has a threshold of 10^{-15} – 10^{-16}T. SQUID magnetometers can measure the magnetic flux of one flux quantum (magnetic flux of Earth's magnetic field through a 7 micron human red blood cell) and has been used to measure the magnetic field of the brain of a mouse to test whether the magnetic field in their brain is enough to assist their internal compass.[8] Table 3.1 puts the sensitivity of SQUIDs in perspective, comparing earth's magnetic field with magnetic fields of the body. The sensitivity of the SQUID is attributed to the Josephson junction that allows the detection of changes in the magnetic field associated with one flux. One flux is quantified as:

$$\Phi_0 = 2h/2e \cong 2.0678 \times 10^{-15}\ \mathrm{T \cdot m^2} \qquad (3.3)$$

In a Josephson junction (Figure 3.2), two superconductors are separated by thin insulating layers, thin enough to allow Cooper pairs (bosons or bound electrons formed by electron-photon interaction) propagating through the superconductor to tunnel through the insulating layer to the other superconductor.[8] Magnetic samples passing through the

Table 3.1. A comparison between the magnetic field of Earth, human body, and the threshold of SQUID.[8-10]

	Magnetic Field (T)
Neutron stars	10^{8}
Strongest destructive pulsed magnet at NHMFL – Los Alomos	850
High energy particle accelerators	10
Magnetic Resonance Imaging	0.5-5
One horsepower electric motor	0.1-0.2
Refrigerator Magnets	$10^{-4} – 10^{-3}$
Earth's Magnetic Field	5.0×10^{-5}
Human heart's magnetic field	$10^{-9} – 10^{-8}$
Intergalactic and Interstellar magnetic field	10^{-11}
Human brain's magnetic field	10^{-13}
Threshold of SQUID	10^{-14}

SQUID coil induces an electrical current. The change in current in response to the magnetic flux of the sample generates a phase difference across the Josepheson junction. Since the current is quantized, the interference between the two junctions ultimately changes the current passing through the superconducting circuits. The changes are detectable and can be correlated to the magnetic flux.

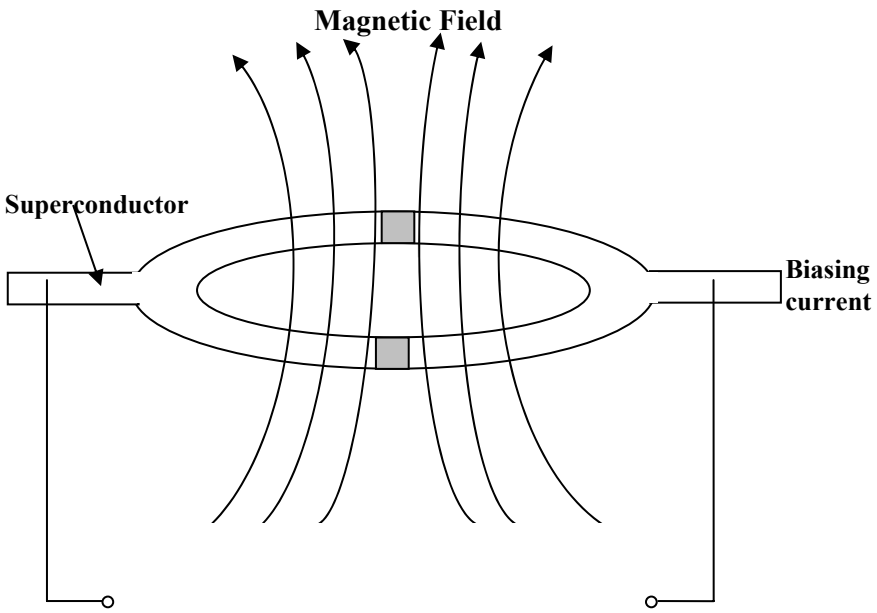

Figure 3.2 Josephson Junction. Figure adapted from reference 8.

There are two types of magnetic measurements that can be made by the SQUID. The first type of measurement is field dependent and temperature independent, M(H). The second type of measurement is temperature dependent and field independent, M(T). Both types of measurements can be performed through a zero field cooled (ZFC) or field cooled (FC) method. In the ZFC method, a sample at room temperature is cooled to a designated temperature in the absence of a magnetic field. As a magnetic field is applied, the magnetization is recorded as the temperature is steadily ramped. In the FC method, like the name implies, the sample is cooled from room temperature in the presence of a magnetic field. In this thesis, measurements are taken using a Quantum Design MPMS-5S SQUID magnetometer and the ZFC method was used. The parameters of temperature

dependent measurements were conducted from 5-700 K with a constant magnetic field of 100 G. Field dependent measurements were conducted at ±5 T with a constant temperature of 5K.

3.1.3 Transmission Electron Microscope (TEM)

Transmission Electron Microscopy (TEM) operates on principles similar to that of the optical microscope.[12,13] The sample illumination source in a TEM is a beam of electrons. This beam of electrons travels through a column under vacuum and is then focused into a very narrow beam with electromagnetic lenses. Some electrons will scatter and those that do not scatter strike a fluorescent screen giving rise to a contrast image based on sample density. Since the limit of resolution is in the order of a few angstroms, it is a very useful and powerful tool for nanoparticle characterization. Low resolution TEM can generally provide information regarding the size and overall shape of the sample and is routinely used to elucidate such information. The TEM used in this thesis was a JEOL 100C at 100 kV. All samples were dispersed in either water or ethanol onto holey carbon grids.

3.1.4 Inductively-Coupled Plasma Optical Emission Spectrometry (ICP-OES)

Elemental analysis has always been important in Analytical chemistry as well as environmental sciences. In the 1940s, arc and high-voltage spark spectrometry were commonly used for elemental analysis.[14,15] As time progressed, flame emission

spectrometry was introduced but was shadowed by atomic absorption spectrometry. It was not until the 1970s when inductively coupled plasma optical emission spectrometry was introduced.[15] Since its introduction, rapid progress on the development and commercialization of ICP-OES has established it a standard technique for mulit-element analysis. This technique is now used more than most other analysis techniques for trace metal analysis.[15-17]

Inductively coupled plasma optical emission spectrometry (ICP-OES) is sometimes referred to as inductively coupled plasma atomic emission spectrometry (ICP-AES).[15] Since most particles in the plasma are ions and since AES can also represent Auger Electron Spectroscopy, the proper terminology is ICP-OES. However, it has been recommended by ISO12235 that "O" be dropped and the technique to be termed ICP-ES.[15] In literature, ICP-AES, ICP-OES, and ICP-ES are used interchangeably. In this thesis, the technique will be referred to as inductively coupled plasma optical emission spectrometry (ICP-OES).

A typical ICP-OES instrument will be comprised of a sample introduction system, torch, generator, optics, spectrometer, and a computer interface (See Figure 3.3). Sample

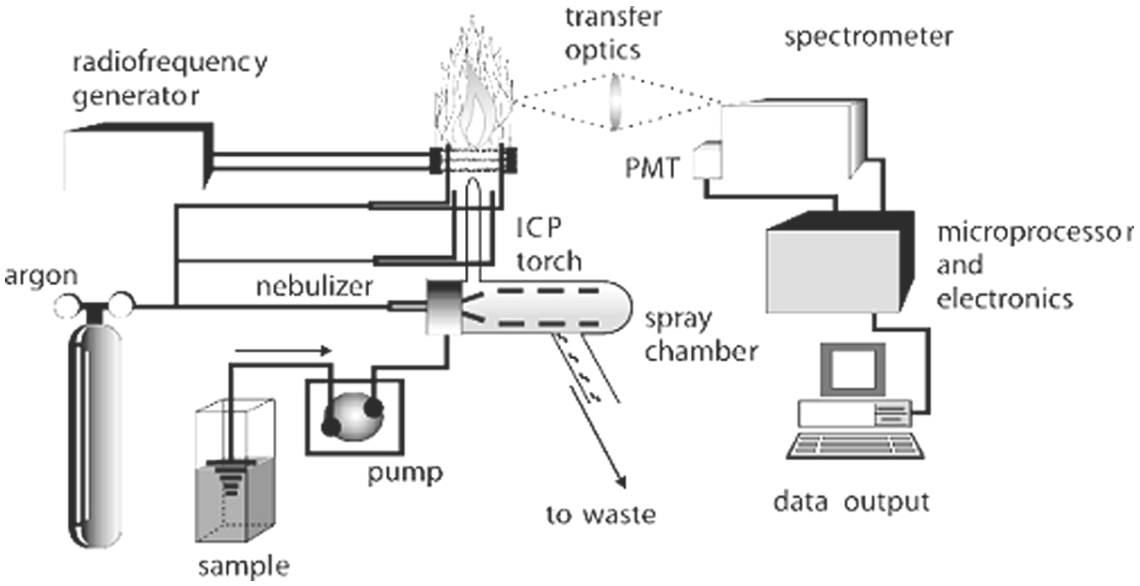

Figure 3.3 Schematic representation of an Inductively Coupled Plasma Spectrometer.[16] Basic components include sample introduction system, torch, generator, optics, spectrometer, and a computer interface.

is introduced into the ICP through an introduction system to the torch where the plasma, at several thousand Kelvin (5000-1000 K), breaks down the sample into its elemental form.[14-17] Therefore, the chemical bonds or the chemical composition of the sample do not influence the analytical result. The hot plasma produces enough energy to excite atoms and ions of the element.[15,17] This is why ICP is sometimes thought of as a hot flame emission spectrometry technique. The emission of electromagnetic radiation from these atoms and ions as they decay to ground state are then resolved through optics and quantified and identified with a detector.[15,17] Data collected is then compared to one generated by a standard series and the concentration of each element in the analysis is then extrapolated. The ICP-OES system used throughout the compiled studies of this thesis is a Perkin Elmer Optima 3000 ICP-OES.

3.2 Biologically Related Instrumentation and Techniques

3.2.1 Laser Scanning Confocal Microscopy (LSCM)

In conventional wide field or brightfield microscopy, a specimen is illuminated with light from either a mercury or xenon source.[18] The image is captured directly as either photographs or displayed on an image capturing device.[18,19] Though simple and convenient to use, wide field microscopes becomes problematic with fluorescent and/or thick samples (>2 μm).[18,19] When background fluorescence is emitted by the specimen, the luminescence may interfere with the focused specimen. On the contrary, with confocal microscopy, specimens are illuminated by beam(s) of laser(s) scanning across the surface.[18,19] This enables the region scanned by the laser(s) to be in focus and excludes all images that are out of the focal plane of interest (See Figure 3.4).

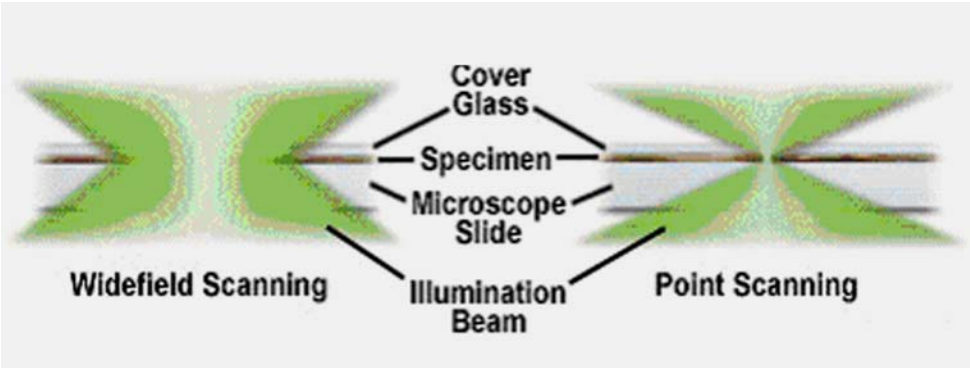

Figure 3.4 Illumination difference between conventional wide field microscopes and laser scanning confocal microscopes.

The creation of confocal microscope is accredited to Marvin Minsky whom invented the concept in 1955 and patented it in 1957.[18-20] The evolution of this instrument was to capture biological occurrences *in vivo*. Minsky placed an actual pinhole in front of the light source. The light was then focused by an objective onto the specimen at the point of interest. As light is reflected and transmitted, the transmitted light is focused by a second objective that has the same focus (defined as confocal). Once again light is either reflected or transmitted. The light that is transmitted through the second focal point strikes a photomultiplier which amplifies the signal to be processed. A schematic of the basic components of and light path in a confocal microscope can be found in Figures 3.5 and 3.6.

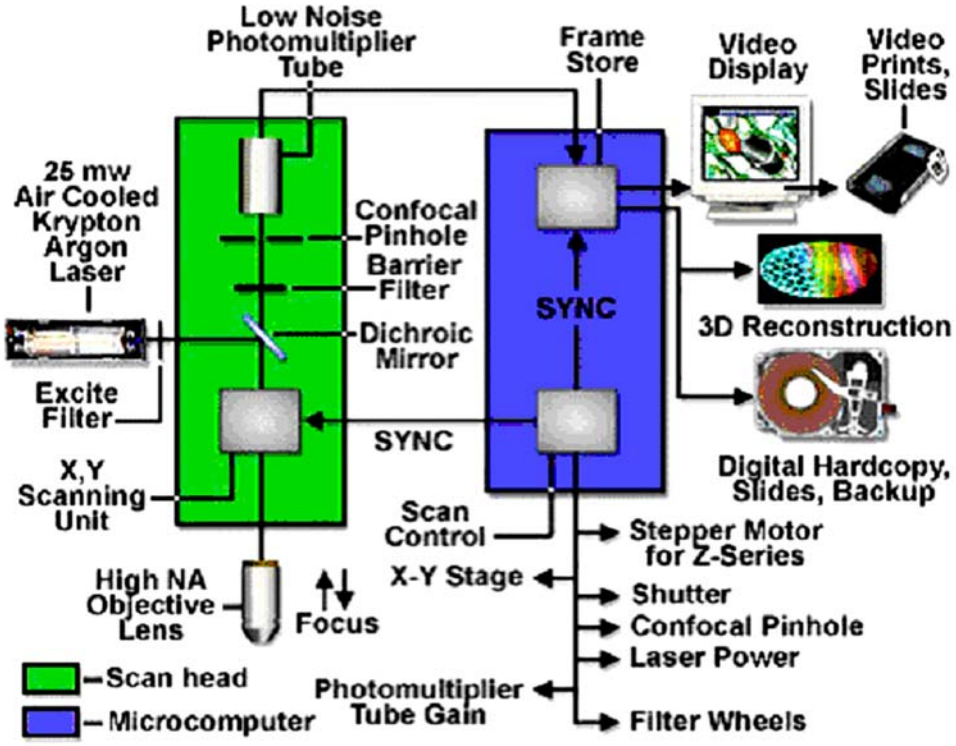

Figure 3.5 Schematic representations of the components of a typical confocal microscope. A laser is used as a light and excitation source. The beam of laser is focused onto the sample. Light signal hits the low noise photomultiplier tube and is then amplified, processed, then displayed.[19]

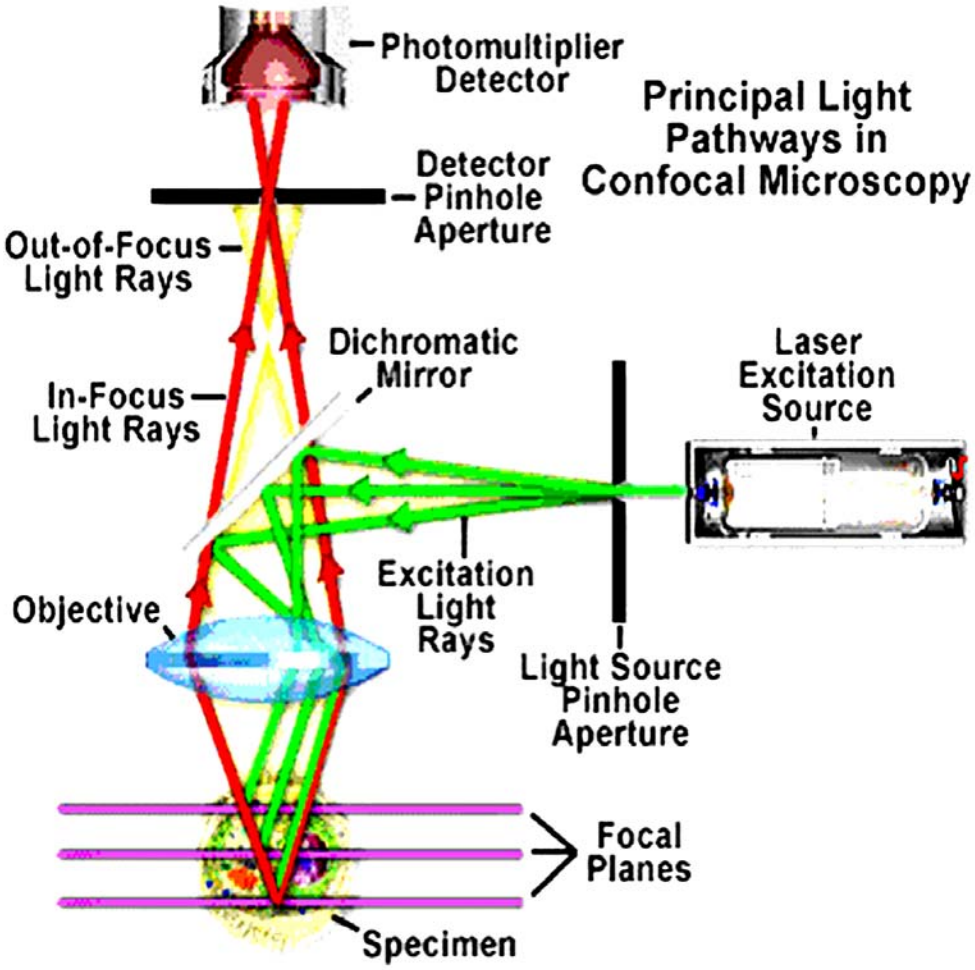

Figure 3.6 Flow of laser beam through confocal microscope.[19]

3.2.2 Dark Field Microscopy

Generally, dark field microscopy is used to visualize transparent materials or materials that have a refractive index close to their environment making them hard to visualize under bright field microscopy. Contrary to bright field microscopy, where the central light passes through and around the specimen of interest (Figure3.4), dark field microscopy, only permits oblique or indirect rays at every azimuth to strike the specimen.[21,22] The components of a dark field microscope are very similar to that of a bright field microscope. The difference is the use of high numerical aperture dark field condenser/ objective pair (Figure 3.7). The light stop of the condenser prevents central rays from striking the specimen. The striked rays are then scattered in different manners by optical discontinuities.[21,22] For example, different organelles of the cell will scatter at different wavelengths. At regions where no specimen is present, the field of view will be dark. Only the scattered regions will show up as illuminated structures. In this thesis an Olympus IX70 inverted microscope housed with a 100X dark field condenser / objective pair was used.

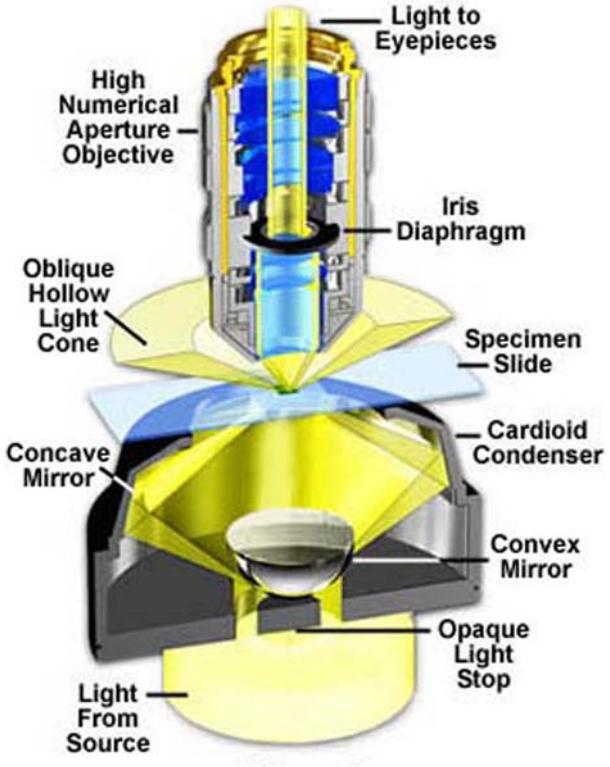

Figure 3.7 Dark field condenser / objective pair.[21]

3.2.3 Flow Cytometer

Flow cytometry is essentially an extension of fluorescence microscopy. It is defined as the detection of cells as they flow rapidly through an orifice in a single file.[23-25] The development of flow cytometry began in 1934 when Andrew Moldavan suggested taking a static microscopy technique and implementing it towards a flowing system.[23] This idea was advanced by Wallace Coulter as he developed a Coulter technique that allowed the quantification of cells in a flowing liquid stream. Further advancements by Louis Kamentsky and Myron Melamed in 1967 as well as contributions from other

research progress by Mack Fulwyler, P.J . Crosland-Taylor, and Marvin Van Dilla, facilitated the development of the flow cytometer that is commonly used in hospital labs and research laboratories today.[23] What started as a technique to count red blood cells is now applicable to differentiate various types of cells.

The components common to most flow cytometers include a light source, stage, lens, filters, and a detector. A general schematic of the components can be seen in figure 3.8. The light source in a flow cytometer is typically a laser or multiple lasers. A laser produces an intense beam of monochromatic light that is usually very important for the excitation of specific dyes. On the contrary to static microscopy techniques, the stage on a microscope is basically a flow cell where a flowing stream of cells are scanned/counted as they pass by the analysis point. Normally, the flow cells will have a nozzle size between 50-250 μm; a non-sorting flow cytometer nozzle size tolerates 50-100 μm and sorting flow cytometers have nozzle sizes from 150-250 μm. As the laser beam projects, it is aligned and focused with a lens or a series of lenses. Likewise, the light that emerges from the intersection of the sample stream and analysis point is collected with lenses that surround the analysis point. The light is then focused onto the detector, usually a photodiode or photomultiplier tube, where the light signals is converted into an electrical signal. Depending on the position of the detector, either forward scattering signal (FSC) is collected, side scattered signal (SSC) is collected, or both. When the detector sits in the path of the illuminating beam then the light that emerges from the analysis point, bending around the cell, will be forward scattering. This type of data is useful if the cross-sectional area, size, or volume of the cell is of interest. Light that is emerges pass the analysis point at a right angle are fluorescent signals. Through color filters, specific

wavelengths can be selected to be detected by the photodectors. Most current models, there equipped with multiple photodectors and multiple filters for multianalysis.

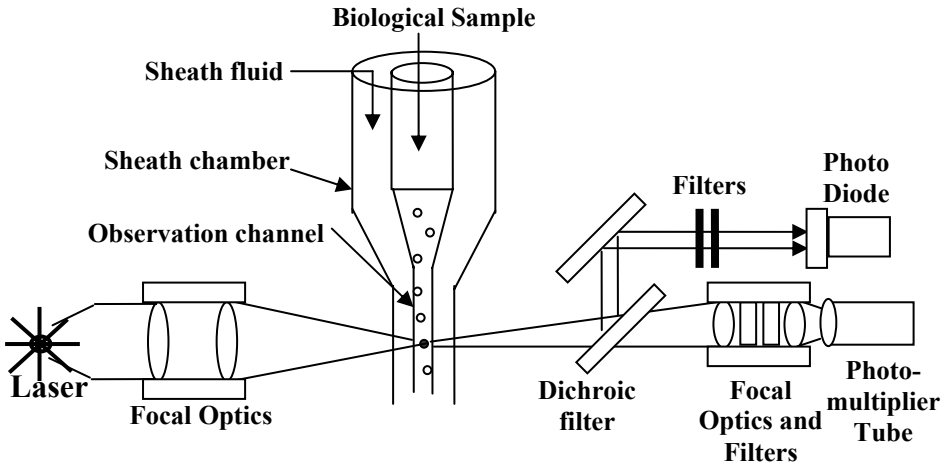

Figure 3.8 Basic components of a flow cytometer include laser(s) as an illuminating source, flow cell to house the capillary that cells flow through in a single file, lenses to focus laser(s) and to focus the signal, filters to select specific wavelength(s) for detection, and photodiode or photomultiplier tube detectors. Figure adapted from reference [26].

3.2.4. Cell Culture Techniques

3.2.4.1 Introduction to Cell Culture

Tissues extracted from an animal are enzymatically digested and then dispersed into cell culture.[25] Daughter cultures can then be formed by seeding from the original culture. This is the process of passaging. Through multiple daughter cultures, a cell line is developed. A cell line can be classified as either primary, secondary, or immortal.[25] Primary cells are taken directly from tissues of a donor organism and are not continuous cell lines. They are only capable of a couple of cycles of cell division but can sustain viability for a long time given proper conditions. Primary cell lines are good representation of *in vivo* systems.[25] Secondary cells are also explanted directly from donor organisms but can divide through multiple generations (50-100).[25] Eventually, secondary cells will begin to change physically and die. Immortal cells on the other hand, will continue to grow and proliferate indefinitely given the optimal conditions. Typically, an immortal cell line consists of cells that have been transformed.[25] This means that its growth properties have been changed by methods such as infection or gene manipulation. In this thesis, transfection is conducted on both primary and immortal cell lines.

3.2.4.2 Transfection

Transfection is a DNA transfer process through which nucleic acids are delivered into cells by non-viral methods (infection). There are two categories of transfection, physical and chemical.[27] Physical methods include direct microinjection,[28] electroporation[29,30], and biolistic particle delivery[31,32]. Chemical methods include using chemical reagents such as dimethylaminoethyl-Dextran (DEAE-Dextran)[33,34], calcium phosphate[35,36], and artificial liposomes[25,37]. Though both categories of transfection methods are effective, physical methods tend to be laborious and are limited to transfecting only a small number of cells. For an example, it would be very cumbersome to inject (microinjection and biolistic delivery) every cell in a cultured plate. Additionally, with methods like electroporation, tuning and optimization of the strength and duration of the electrical pulse must be adjusted for each different cell line (typically used in plant cell lines). Hence, a chemical method of transfection was used in this thesis.

Since the cell membrane is negatively charged, the transport of negatively charged species across the membrane is either prohibited or retarded. Chemical methods take advantage of introducing net positive charges to allot for the transport across the membrane. When using DEAE-Dextran, the cationic polymer associates tightly with the backbone of DNA and facilitates the transport via endocytosis. Genes and gene fragments can also be precipitated with calcium phosphate co-precipitation methods where the precipitate is taken up through endocytosis or phagocytes. The most effective chemical method for transfection is through lipofection where nucleic acids are transported into

cells through complexing with artificial liposomes. A unique property of using artificial liposomes over other chemical reagent transfection methods is that it is applicable *in vivo*.

Lipofection was first introduced by Felgner et al. in 1987.[37] Originally, a monocationic lipid was used to complex with DNA introducing a net positive charge on the complex. Through endocytosis the positively charged complex is taken up by the cells. This method was later improved by replacing the monocationic lipid reagent with a polycationic lipid[38] or Lipofectamine.[39] Lipofectamine is a liposome composed of polycationic lipid, 2,3-dioleyloxy-*N*-[2-(sperminecarboxamido)ethyl]-*N*, *N*,-dimethyl-1-propanaminium tryfluoroacetate (DOSPA) and a neutral lipid, dioleoyphosphatidylethanol-amine (DOPE).[25] It is proposed that the polycationic lipid's role is to complexes with the backbone of the DNA introducing the positive charge while the neutral lipid's role is to act as a "fusongenic", enabling the release of nucleic acids from the endsomes in cell.[40]

Although the main purpose of transfection is to transfer DNA or fragments of DNA into cells, we have utilized this property to facilitate the delivery of our magnetic nanoparticles conjugated to oligonucleotides (mnp-oligo) into mammalian cells.

3.3 References

(1) Cullity, B. D. *Elements of X-ray Diffraction*; Addison-Wesley Publishing Co.: Reading, 1978.

(2) http://www.matter.org.uk/diffraction/Default.htm.

(3) Klug, H. P.; Alexander, L. E. *X-ray Diffraction Procedures*; 2nd ed.; John Wiley: New York, 1974.

(4) West, A. R. *Basic Solid State Chemistry*; 2nd ed.; Wiley: New York, 1999.

(5) http://hyperphysics.phy-astr.gsu.edu/hbase/quantum/bragg.html.

(6) Jenks, W. G.; Thomas, I. M.; Wikswo, J. J. P. In *Encyclopedia of Applied Physics*; VCH Publishers, Inc.: New York, 1997; Vol. 19, p 457.

(7) Rondinone, A. J.; Zhang, J. Z. In *Handbook of Nanophase and Nanostructured Materials*; Wang, Z. L., Liu, Y., Zhang, Z., Eds.; Kluwer Academic: New York, 2003; Vol. III, p 252.

(8) Rohlf, J. W. *Modern Physics from α to Z^0*; Wiley: Indianapolis, 1989.

(9) Inan, U. S.; Inan, A. S. *Engineered Electromagnetics*; Addison Wesley Longman, Inc.: Upper Saddle River, 1999.

(10) Herlack, F. *Physica B.* **2001**, *500-504*, 294.

(11) Livingston, J. D. *Driving Force: The Natural Magic of Magnets*; Harvard University Press: Cambridge, 1996.

(12) De Graef, M. *Introduction to Conventional Transmission Electron Microscopy*; Cambridge University Press: Melbourne, 2003.

(13) www.matter.org.uk/etm/.

(14) Skoog, D. A.; Holler, F. J.; Nieman, T., A. *Principles of Instrumental Analysis*; 5th ed.; Thomposon Learning, Inc.: Independence, 1998.

(15) Nolte, J. *ICP Emission Spectrometry*; Wiley-VCH Verlag GmbH & Co.: Weinheim, 2003.

(16) Ryden, L.; Migula, P.; Andersson, M., Eds. *Environmental Science - Understanding, Protecting, and Managing the Environment in the Baltic Sea Region*; Baltic University Press: Uppsala, 2003.

(17) Montaser, A., Ed. *Inductively Coupled Plasma Mass Spectrometry*; Wiley-VCH, Inc.: New York, 1998.

(18) Paddock, S. w., Ed. *Confocal Microscopy - Methods and Protocols*; Humana Press: Totowa, 1999.

(19) www.microscopyu.com/articles/confocal/confocalintrobasics.html.

(20) Kraeft, S.-K.; Hafeli, U. O.; Chen, L. B. In *Scientific and Clinical Applications of Magnetic Carriers*; Hafeli, U. O., Shutt, W., Teller, J., Zborowski, M., Eds.; Plenum Press: New York, 1997, pp 149.

(21) http://olymusmicro.com.

(22) Capadona, L. A. In *Chemistry and Biochemistry*; Georgia Institute of Technology: Atlanta, 2004.

(23) Givan, A. L. *Flow Cytometry - First Principles*; Wiley-Liss, Inc.: New York, 2001.

(24) Jaroszeski, M. J.; Heller, R., Eds. *Flow Cytometry Protocols*; Humana Press: Totowa, 1998.

(25) Freshney, I. R. *Culture of Animal Cells - A Manual of Basic Technique*; Wiley-Liss, Inc.: New York, 2000.

(26) www.engin.umich.edu/alumni/engineer/02SS/protective/MIFCBasic.gif.

(27) www.promega.com.

(28) Cappechi, M. R. *Cell* **1980**, *22*, 479.

(29) Shigekawa, K.; Dower, W. J. *BioTechniques* **1988**, *6*, 742.

(30) Wong, T. K.; Neumann, E. *Biochem. Biophys. Res. Commun.* **1982**, *107*, 584.

(31) Klein, T. M.; Wolfe, E. D.; Wu, R.; Sanford, J. C. *Nature* **1987**, *327*, 70.

(32) Ye, G. N.; Danielle, H.; Sanford, J. C. *Plant. Molec. Biol.* **1990**, *15*, 809.

(33) Vaheri, A.; Pagano, J. S. *Virology* **1965**, *27*, 434.

(34) McCutchan, J. H.; Pagano, J. S. *J. Natl. Cancer. Inst.* **1968**, *41*, 351.

(35) Graham, F. L.; van der Eb, A. J. *Virology* **1973**, *52*, 456.

(36) Loytner, S.; Scangos, G. A.; Ruddle, R. H. *Proc. Natl. Acad. Sci. USA* **1982**, *79*, 422.

(37) Felgner, J.; Bennett, F.; Felgner, P. L. *Proc. Natl. Acad. Sci. USA* **1987**, *87*, 7413.

(38) Hawley-Nelson, P.; Ciccarone, V.; Gebeyehu, G.; Jessee, J.; Felgner, P. L. *Focus* **1993**, *15*, 73.

(39) Shih, P.; Evans, K.; Schifferli, K.; Ciccarone, V.; Lichaa, F.; Masoud, M.; Lan, J.; Hawley-Nelson, P. *Focus* **1997**, *19*, 52.

(40) Farhood, H.; Servina, N. S.; Huang, L. *Biochim. Biophys. Acta* **1995**, *1235*, 289.

CHAPTER IV

MODULATING THE MAGNETIC PROPERTIES OF COBALT SPINEL FERRITE NANOPARTICLES WITH SAMARIUM

ABSTRACT

Varying concentrations of samarium have been doped into cobalt spinel ferrites to produce magnetic nanoparticles with the composition of $CoSm_xF_{2-x}O_4$. X-ray powder diffraction patterns of $CoSm_xF_{2-x}O_4$ with an average particle size of 7.2nm did not reveal any significant changes in diffraction patterns relative to the native $CoFe_2O_4$ spinel structure. With varying doping percentages, insignificant changes in magnetic properties were observed. When compared to the native $CoFe_2O_4$ magnetic nanoparticle, a significant decrease in the saturation magnetization and increase in coercitivity was observed. A size variation study of Co $Sm_{0.19}Fe_{1.81}O_4$ revealed a parallel increase in blocking temperature, T_b, and saturation of magnetization, M_s, but a non-linear trend in coercitivity, H_c. This study elucidated the tunability of the magnetic properties of cobalt

spinel ferrites via compositional changes by incorporation of rare earth metal such as Sm and by size variation of the magnetic nanoparticle.

4.1 Introduction

The fundamentals and applications of nanoparticles have been explored extensively.[1-4] Magnetic nanoparticles are typically known for information storage, magnetic resonance imaging (MRI), and more recently for a number of biological applications (see chapter 2 and references within). It is the unique superparamagnetic properties that render magnetic nanoparticles attractive for different application and investigation. Superparamagnetic properties such as their blocking temperature, coercitivity, and their saturation magnetization can be modulated by varying the compositional make up and the size of nanoparticles'.[5-7] The ability to control the magnetic properties of nanoparticles is of fundamental interest in developing new and innovative materials.

Rare earth metals, well known for their interesting optical properties and chemical stability, have been noted as good candidates for the growing development of new and innovative magneto-optical recording media.[7,8] The 14 inner transition elements are all chemically and structurally similar with a partially filled 4*f* shell with the exception of La and Lu.[8] The magnetic moment of lanthanides can range from 0-10.5 μ_B and their variation in *f* electron configuration can introduce interesting magnetic interactions.[8-14] Optically, some lanthanide ions have an unusually long Stokes shift rendering them good

candidates for luminescence probes. For example, Eu^{3+} and Tb^{3+} luminesces green and red respectively when excited at wavelengths of about 296 nm.[15] Additionally, Eu^{2+} luminesces blue. With different luminescence colors upon excitation, these lanthanide elements make good probes for oxidation states of targeted species.[16]

Of particular interest in this chapter is samarium. Like Eu^{3+} and Tb^{3+}, Sm^{3+} have a long stoke shift as well and are used to as fluorescence markers when bound to chelating molecules.[15] Samarium has five unpaired 4*f* electrons and has been used in applications ranging from carbon arc lighting for motion pictures to roles in stimulating metabolism.[8] Other examples include, samarium – cobalt magnets as one of the strongest types of magnets with an intrinsic coercive force that can be as high as 2200 kA/m.[17] In addition, samarium oxide has been used in optical glass to absorb infrared light and for catalytic purposes to dehydrate and dehydrogenate ethanol.[8] It has been shown that thin films of rare earth doped cobalt ferrites possess different magnetic properties of native cobalt ferrite films. For example, Cheng et. al. observed that there is an antiparallel relationship between the Curie temperature and the concentration of rare earth doped in cobalt spinel ferrite films prepared by sol-gel methods.[7] They also observed a reduction in magneto – optical rotation with increasing doping percentages of rare earth metals. More recently, our group began investigating methods of controlling the magnetic properties of cobalt spinel ferrite nanoparticles using rare earth metals through an oil-in-water synthesis method. Previously, we demonstrated that a set of lanthanides (Sm, Ce, Eu, Gd, Er, Dy) doped in cobalt spinel ferrites resulted in dramatic variation of magnetic properties when different lanthanide ions were incorporated.[6] The variation of blocking temperature, saturation magnetization, and coercitivity with different doped lanthanide ions prompted

a further interest for a systematic study. In addition, we recognized that samarium, like other rare earth metals, are less likely to be present in biological buffers, making them a unique marker when they are present. In this chapter, a systematic study on samarium doped cobalt spinel ferrite nanoparticles to probe the magnetic modulational control will be elaborated.

4.2 Experimental

4.2.1 Synthesis

Cobalt spinel ferrites, $CoFe_2O_4$, were synthesized using a normal micelle method previously described.[18] Cobalt-samarium spinel ferrites were also synthesized using the normal micelle method with slight modification.[6,18] Briefly, stoichiometric amounts of $CoCl_2 \cdot 4H_2O$: x $SmCl_3 \cdot 6H_2O$: 2-x $FeCl_2 \cdot 4H_2O$ (x = 0 – 0.187) were mixed in sodium dodecyl sulfate (SDS) then chilled to 10°C in an ice bath. Aqueous methylamine (~11mol) was added at 10°C and the mixture was then heated to 75°C ± 5°C for two to three hours. Nanoparticles were then isolated via centrifugation followed by washing with distilled water then with a 20% v/v aqueous ethanoic solution. The final product was then magnetically separated and dried at 110°C.

4.2.2 Instrumentation

X-ray powder diffraction patterns of $CoFe_2O_4$ and $CoSm_xFe_{2-x}O_4$ were collected using a Bruker D8 Advance Diffractometer with a CuKα line. Transmission electron micrographs were primarily taken to verify the size estimated by XRD. Magnetic properties of $CoFe_2O_4$ and $CoFe2_{-x}Sm_xO_4$ spinel ferrite nanoparticles were measured using a Quantum Design MPMS-5S superconducting quantum interference device (SQUID). An applied field of 100G was applied in susceptibility experiments that swept from 5-300K or 300-500K. Hysteresis measurements were measured at 5T at 5K unless otherwise designated. Doping percentages were confirmed by digesting $CoSm_xFe_{2-x}O_4$ with 40% nitric acid (trace metal grade) then diluting to 1% HNO_3 final concentration before introducing into a Perkin-Elmer Optima 3000 ICP-OES system.

4.3 Results and Discussion

This systematic study was broken down into two categories, variation in percent composition and size variation studies. In the first category, the average size of the particle was kept constant (average particle size of 7.2nm) while the percent composition of the magnetic nanoparticle was varied resulting in the formula of $CoSm_xFe_{2-x}O_4$ (x = 0 – 0.19). In the second category, the percent composition of the magnetic particles was kept constant, x = 0.19, while varying the size (4.7nm – 12.5nm) of the magnetic nanoparticles.

4.3.1. Composition variation

X-ray powder diffraction patterns of $CoSm_xFe_{2-x}O_4$ were collected at the 2θ range of 15-85°. The diffraction pattern indicated a spinel phase and mirrored that of $CoFe_2O_4$ (Figure 4.1). Therefore, the introduction of Sm^{3+} did not change the lattice constant. Size of the nanoparticles determined from the peak broadening using Scherrer's equation correlated well with size determined through TEM images. The average size of $CoSm_xFe_{2-x}O_4$ used for comparison was 7.2nm with a size distribution up to 15%. The chemical composition of $CoSm_xFe_{2-x}O_4$ was determined with ICP-OES. Elemental analysis data collected for $CoSm_xFe_{2-x}O_4$ identified x = 0 – 0.19.

Magnetic characterization of $CoSm_xFe_{2-x}O_4$ (x = 0 – 0. 19) illustrated that there is a general consistency of T_b within the samples examined (See Table 4.1 and Figure 4.2). In Figure 4.2, the peak of each individual curve represents the blocking temperature. Above this temperature, magnetic moments have enough thermal activation to overcome the energy barrier for magnetization reversal. Hence above the T_b the susceptibility begins to decrease as moments behave like paramagnetic materials but with stronger magnetization. From Table 4.1 and Figure 4.3, information regarding the M_s (magnetization saturation) and H_c (coercitivity) of $CoSm_xFe_{2-x}O_4$ is revealed. As the magnetic field is ramped from zero to 50,000 Oe then back to zero, remnant magnetization forms a "memory" effect, hysteresis. An opposite field is required to force the magnetization back to zero with an opposite field. The amount of magnetic field required to return the magnetization to zero is referred to as coercitivity. When all of the moments align with the field, magnetization saturation is reached. Within the Sm doped

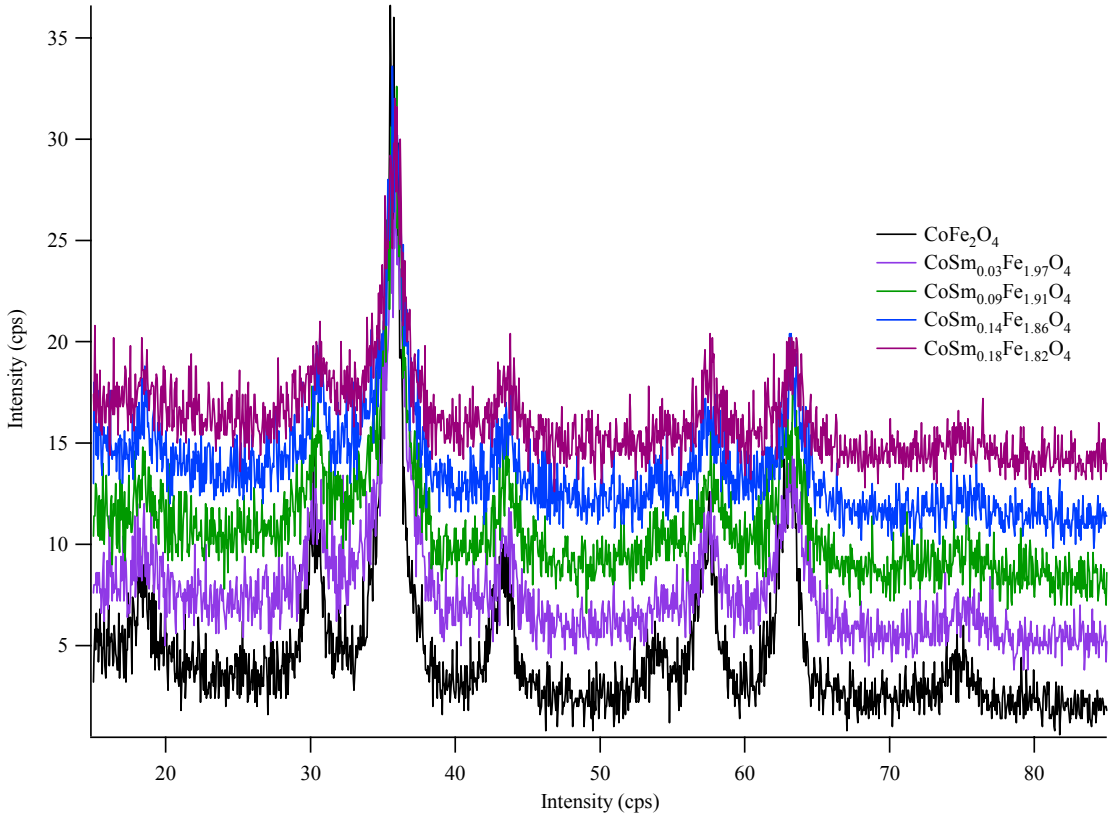

Figure 4.1 XRD pattern of $CoSm_xFe_{2-x}O_4$ compared to native $CoFe_2O_4$. Diffraction patterns of $CoSm_xFe_{2-x}O_4$ do not show any significant difference when compared to $CoFe_2O_4$ indicating that a correct spinel phase has been accomplished. Intensities were intentionally offset to demonstrate the similarity in patterns between samarium doped cobalt spinel ferrites and native cobalt spinel ferrite magnetic nanoparticles.

Sm doped cobalt spinel ferrite samples, a relatively small change in M_s and H_c was observed (see Table 4.1 and Figure 4.3). However, when the M_s and H_c of doped particles were compared to native particles, $CoFe_2O_4$, there is a clear difference. The M_s of the 7.2 nm sized $CoSm_xFe_{2-x}O_4$ were all in the general range of about 34 – 40 emu/g·Oe which is a marked decrease when compared to the M_s of $CoFe_2O_4$ at 68.4 emu/g·Oe. Even if 10-15% instrument error is accounted for, the doped and undoped M_s values differ dramatically. The H_c of this series of $CoFSm_xe_{2-x}O_4$ had less than one kOe change within samples ranging from x>0 but is on average about 4.9 kOe higher than that of $CoFe_2O_4$ (H_c = 11.0 kOe). When measurements are made at temperatures above the blocking temperature, hysteresis disappears (Figure 4.4) because there is enough energy to overcome the magnetization reversal energy barrier allowing moments to line up with the direction of the magnetic field. This is characteristic of superparmagnetic nanoparticles.

Table 4.1 Summary of magnetic characteristics of $CoSm_xFe_{2-x}O_4$.

Sample	**T_b (K)**	**M_s (emu/g)**	**H_c (KOe)**
$CoFe_2O_4$	305.6	69.8	11.0
$CoSm_{0.03}Fe_{1.97}O_4$	273.4	39.6	15.8
$CoSm_{0.05}Fe_{1.95}O_4$	271.6	39.3	15.1
$CoSm_{0.14}Fe_{1.86}O_4$	322.7	34.4	15.7
$CoSm_{0.19}Fe_{1.81}O_4$	283.4	37.5	15.7

From the Stoner – Wohlfarth theory[19], we know that the energy barrier for magnetization reversal can be represented by

$$E_A = KV\sin^2\theta \qquad (4.1)$$

where E_A is the energy barrier for magnetization reversal, K is the magnetocrystalline aniosotropy constant, V is the volume of the nanoparticle, and θ is the angle between the direction of magnetization and the easy axis of the nanoparticle.[19] Since the blocking temperature is the threshold and the point at which magnetic nanoparticles become superparamagnetic, it will be reflected by nanoparticle size. The evaluated samples in this category were of very similar sizes and hence, the volume of these nanoparticles is very similar. Therefore, the insignificant changes in T_b were expected and correlated well with theory.

The large coercive force of $CoFe_2O_4$ has been proposed to originate from the single-ion anisotropy of Co^{2+} ions in the octahedral sites.[7] Neutron diffraction study show that $CoFe_2O_4$ is a mixed spinel with approximately 72% inversion for cation occupancy.[18,20] Since most lanthanide ions have relatively large absorption cross sections, common neutron scattering studies for Sm^{3+} were not done. Previous neutron diffraction studies of La^{3+} doped cobalt spinel ferrites showed that all of the doped ion resides in the octahehral sites and replaced only Fe^{3+} ions. [18,20] Since the ionic radius of La^{3+} (117 pm)[16] is similar to the ionic radius of Sm^{3+} (110 pm)[16], we postulate that all of the Sm^{3+} ions doped are replacing Fe^{3+} ions residing in octahedral site. Samarium has a strong

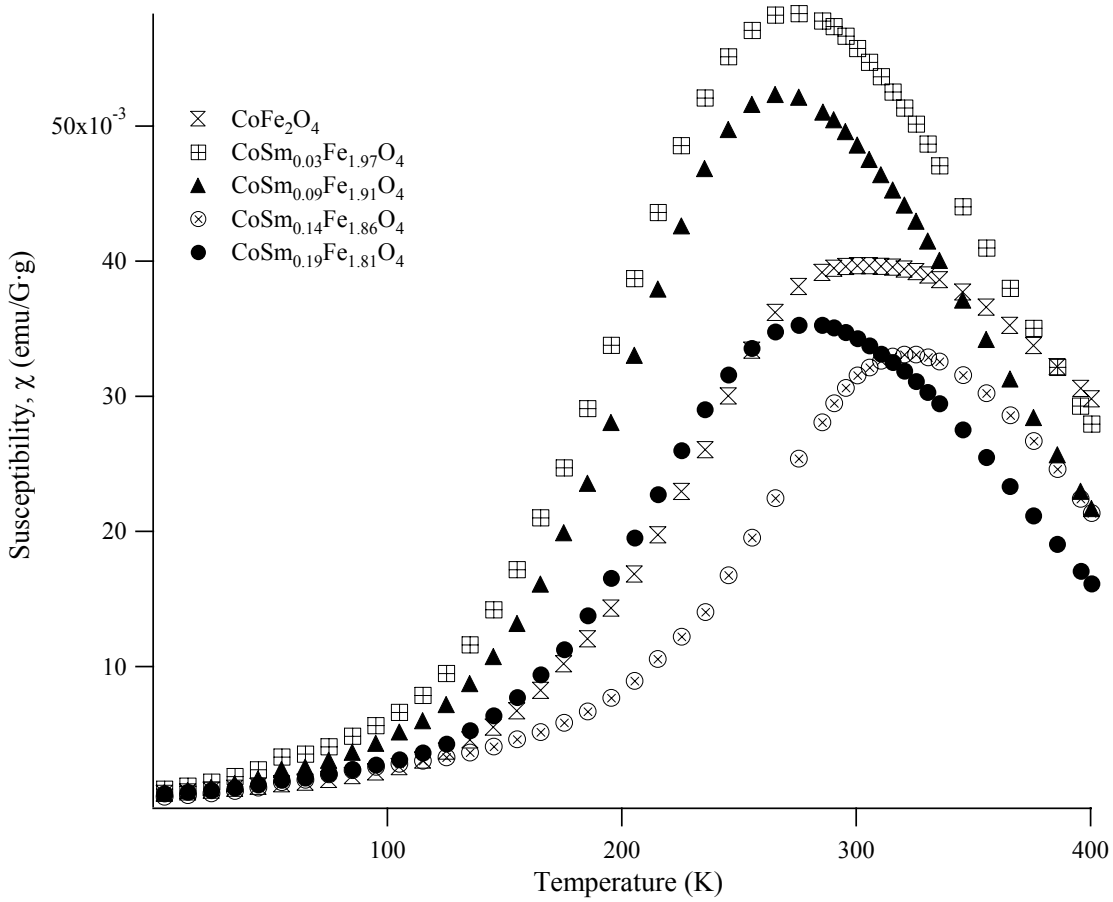

Figure 4.2 Varying percent Sm doped susceptibility vs. temperature plot of a series of 7.2nm $CoSm_xFe_{2-x}O_4$ (x = 0, 0.03, 0.09, 0.14, 0.19) magnetic nanoparticles. The blocking temperature correlates to the peak or maximum susceptibility point of each curve.

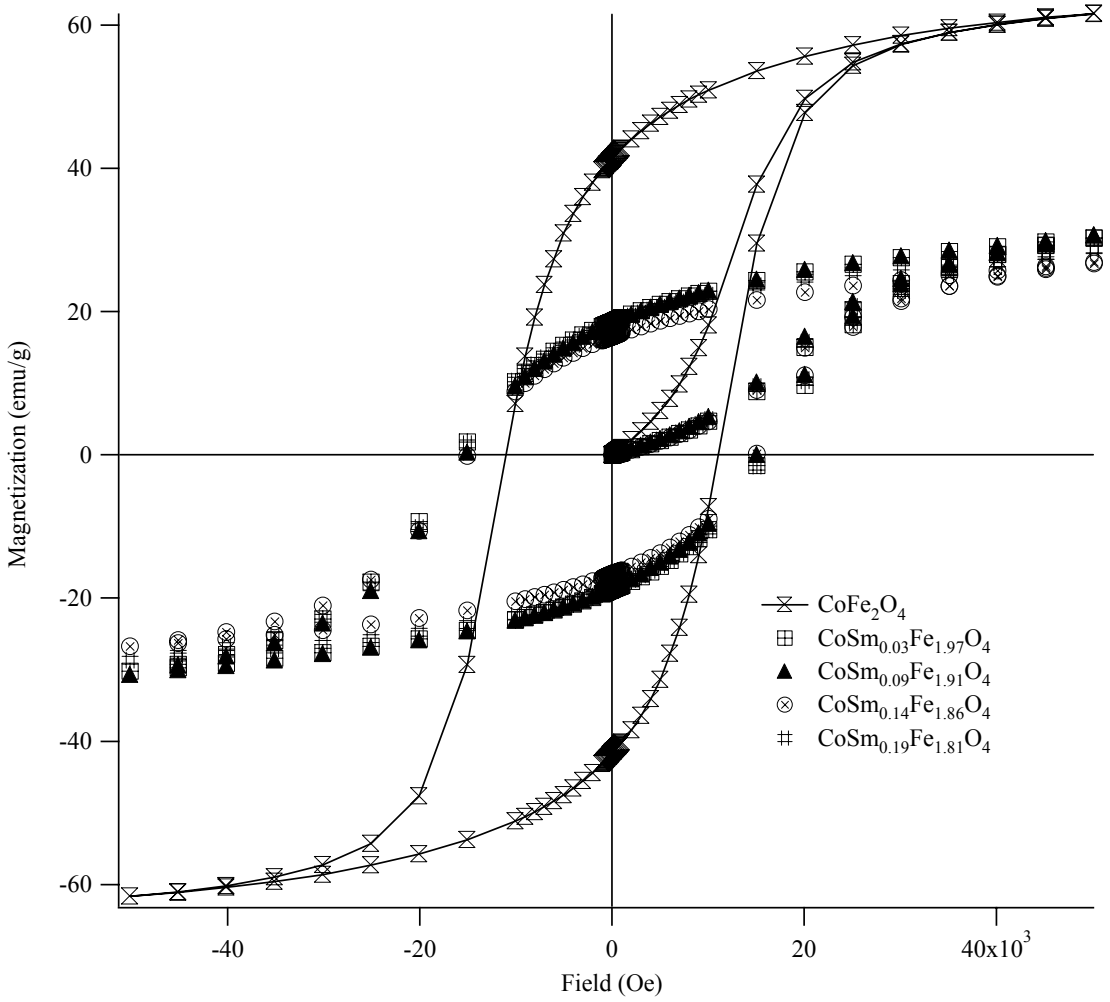

Figure 4.3 Hysteresis loop of 7.2nm $CoSm_xFe_{2-x}O_4$ magnetic nanoparticles at 5K. The magnetic field is ramped from zero to 50 kOe then to the same magnitude but in a different direction. Once at the magnetization saturation point, where moments align with the direction of the applied field, the reversal of magnetic moments generates a hysteresis loop. The introduction of samarium into cobalt spinel ferrite reduces the M_s and increases the H_c due to high coercive forces from samarium.

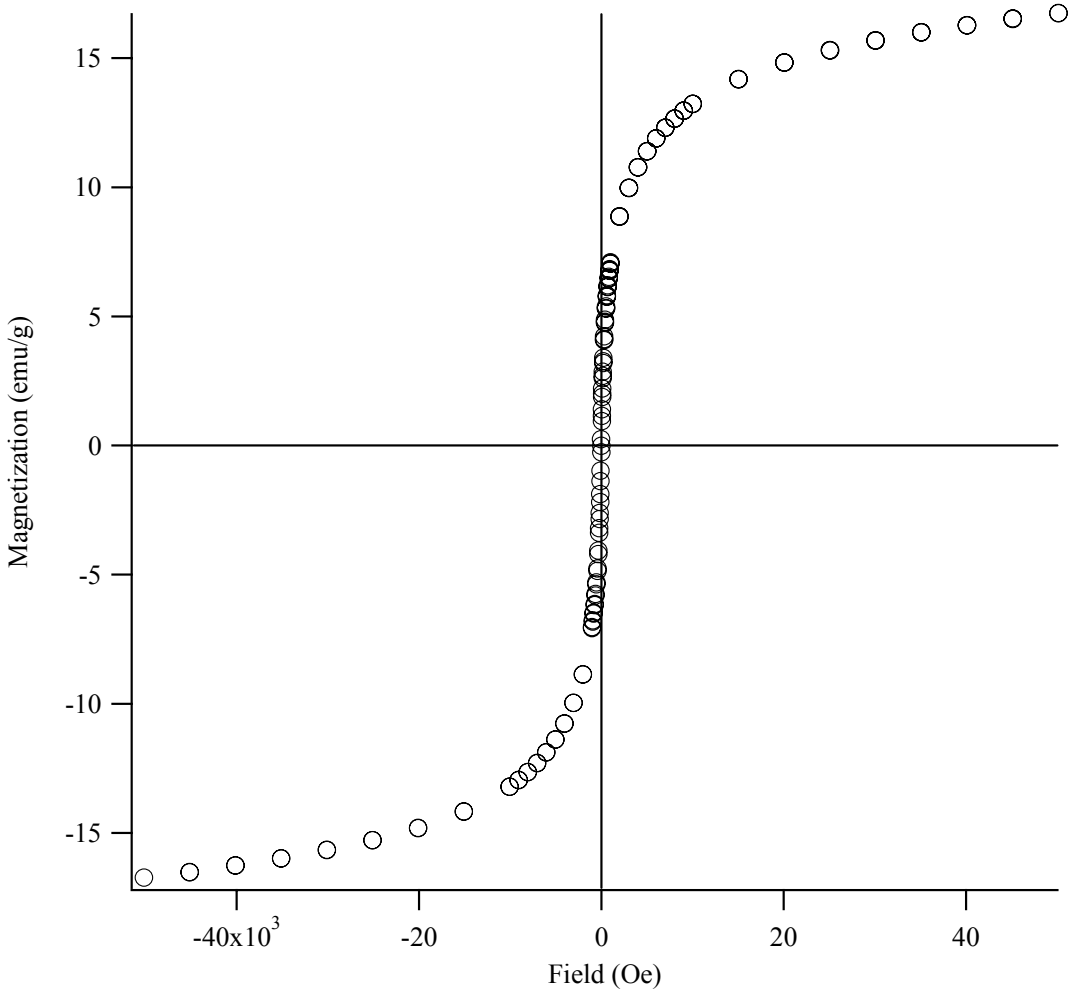

Figure 4.4 Hysteresis measurement of $CoSm_{0.19}Fe_{1.81}$ at 300K. Above the blocking temperature of $CoSm_{0.19}Fe_{1.81}$ (283.4K), there is enough thermal energy to overcome the E_A allowing reversal of magnetization, hence there is an absence of hysteresis.

spin-orbit coupling that leads to large magnetocrystalline aniosotropy.[8] Hence, Sm^{3+}has a very high coercive force and adds to the coercive forces of cobalt spinel ferrites. Results showed an increase in coercitivity when $CoSm_xFe_{2-x}O_4$ is compared to $CoFe_2O_4$. Within varying amounts of Sm^{3+} ion doped, an negligible change in coercitivity was observed. Since the doping concentration change of Sm^{3+} is relatively small, the change in coercitivity is not as obvious and most likely insignificant. When hysteresis measurements are made above the blocking temperature, hysteresis disappears as evident in Figure 4.4, which is characteristic of superparmagnetic nanoparticles. Above the blocking temperature, there is enough energy to overcome the magnetocrystalline anisotropy barrier allowing the moments to align with the magnetic field.

Abstracting from the Stoner – Wolhfarth theory, the coercitivity of nanoparticles can be determined by

$$H_c = 2K/(\mu_0 M_s) \tag{4.2}$$

where K is the magnetocrystalline anisotropy constant and μ_0 is a universal constant of permeability in vacuum. So if we rearrange this equation to

$$M_s = 2K/(\mu_0 H_c) \tag{4.3}$$

then a decrease in M_s is expected with an increase in H_c. Observation definitely showed a decrease in M_s when samarium doped cobalt ferrite was compared to the undoped cobalt ferrite but less defined changes in the M_s were observed within doped samples. Once

again, since the difference between the concentration of Sm^{3+} doped in $CoFeSm_xFe_{2-x}O_4$ is relatively small, the changes in saturation magnetization are relatively small and negligible.

4.3.2 Size variation

In this second category, the size of $CoSm_{0.19}Fe_{1.81}O_4$ was varied from 4.7nm - 12.5nm. Elemental analysis with ICP-OES confirmed the composition ratio of $CoSm_{0.19}Fe_{1.81}O_4$. X-ray diffraction patterns (Figure 4.5) mirrored those of native $CoFe_2O_4$ (refer to Figure 4.1 for native $CoFe_2O_4$ diffraction pattern) indicating the presence of the spinel phase. Since the diffraction patterns were essentially the same, we can assume that introduction of Sm^{3+} did not change the lattice constant. Sizes of $CoSm_{0.19}Fe_{1.81}$ nanoparticles were determined from the peak broadening in XRD patterns using Scherrer's equation and correlated well to sizes determined with TEM images. Size control of cobalt spinel ferrites has been established in previous studies[18] and similar synthetic procedures were used to vary the sizes of $CoSm_xFe_{2-x}O_4$. To determine the blocking temperature of these magnetic nanoparticles, a low temperature range, 5K-300K, at 100G, was applied. Additionally, for the 12.5nm $CoSm_{0.19}Fe_{1.81}O_4$, a high temperature range, 400K-500K, at 100G was used.

From the results (see Table 4.2 and Figures 4.6-4.7), we can draw that there is an increase T_b parallel to the increase in nanoparticle size. Likewise there is a increase in M_s with increased size. A non-linear trend was observed for H_c with size variation. Initially,

there is an increase in H_c with increasing size but then it decreases with further increase in size of the magnetic nanoparticles.

The increase in T_b with increasing size is an anticipated increase based on the Stoner-Wohlfarth theory (see equation 4.1). From equation 4.1 we can see the correlation between size and E_A. An increase in the size of nanoparticles will increase volume, hence, it will increase the E_A. Likewise, a decrease in the volume of the nanoparticle will decrease E_A of the system. The results obtained correlates well with theory.

Table 4.2. Magnetic characteristics of $CoSm_{0.191}Fe_{1.809}O_4$ of various sizes.

Size (nm)	**T_b**	**M_s**	**H_c**
4.7	201.9	21.7	8.8
7.0	272.4	31.5	16.9
10.0	346.6	59.5	10.9
12.5	424.3	65.6	8.9

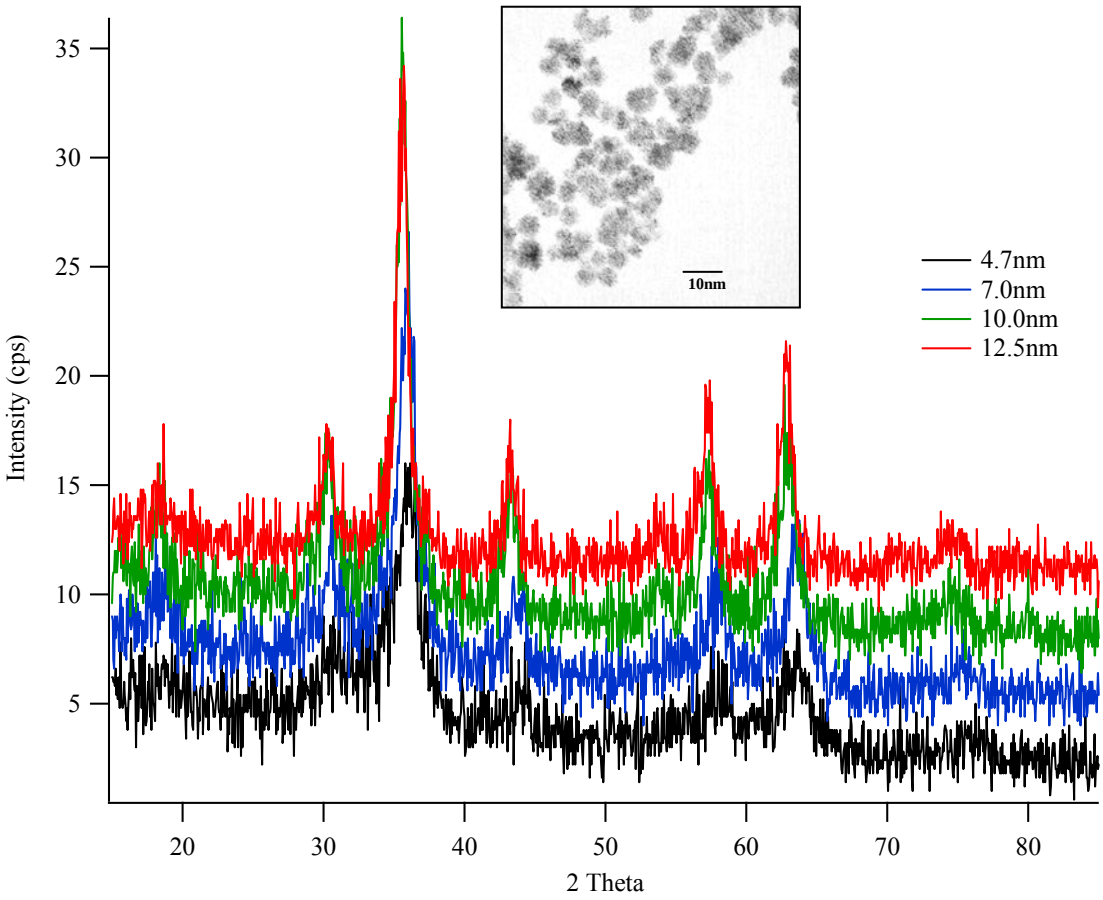

Figure 4.5 XRD pattern of various sized $CoSm_{.0191}Fe_{1.981}O_4$. The intensities were intentionally offset to demonstrate the similarity in patterns. Inset shows a TEM micrograph of a sample of approximately 7.2nm diameter at 100K magnification.

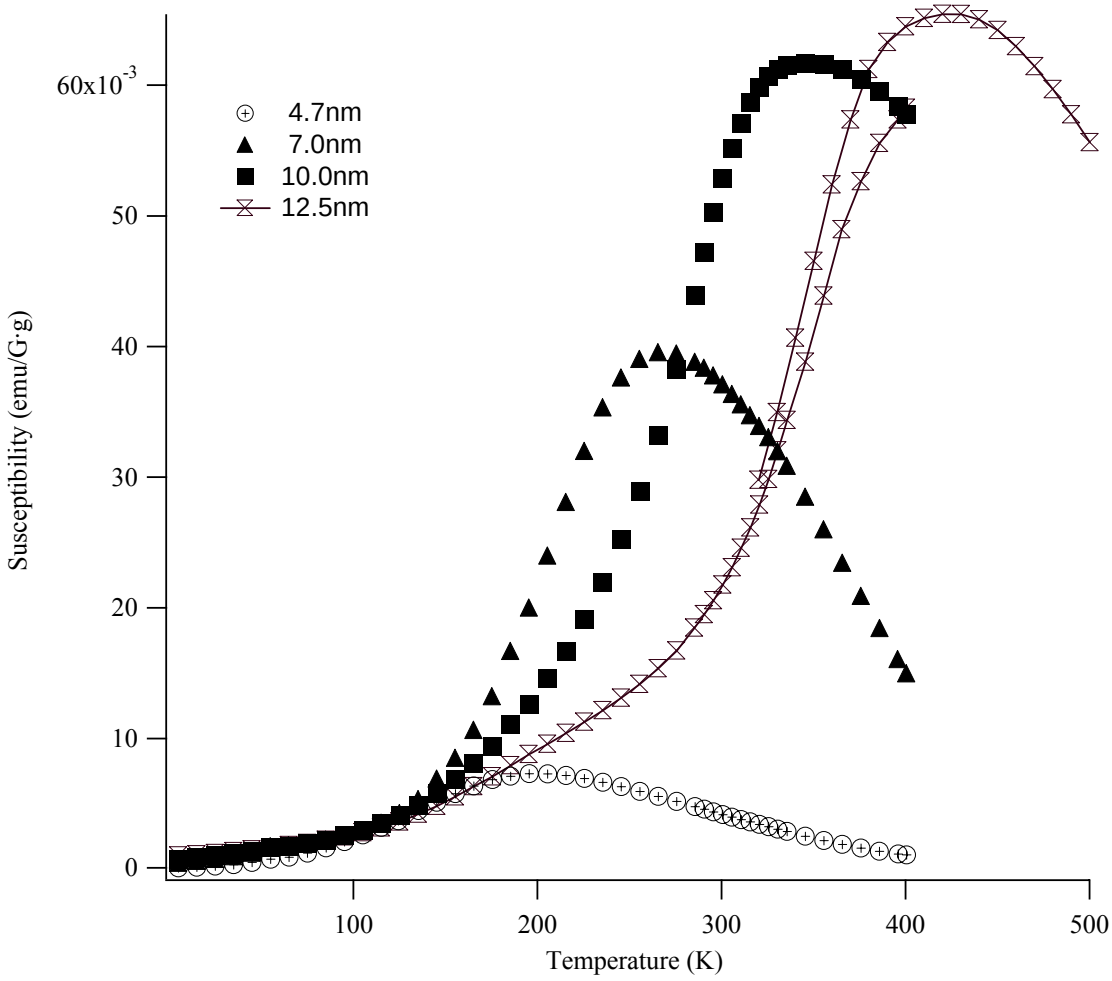

Figure 4.6 Size variation susceptibility vs. temperature plot of $CoSm_{.019}Fe_{1.81}O_4$. For the 12.5 nm $CoSm_{0.19}Fe_{1.81}O_4$ curve, it is actually made up of two curves, one ranging from 5-400K and another from 400-500K. The maximum susceptibility point or peak of the curve correlates to the blocking temperature of different sized $CoSm_{.019}Fe_{1.81}O_4$.

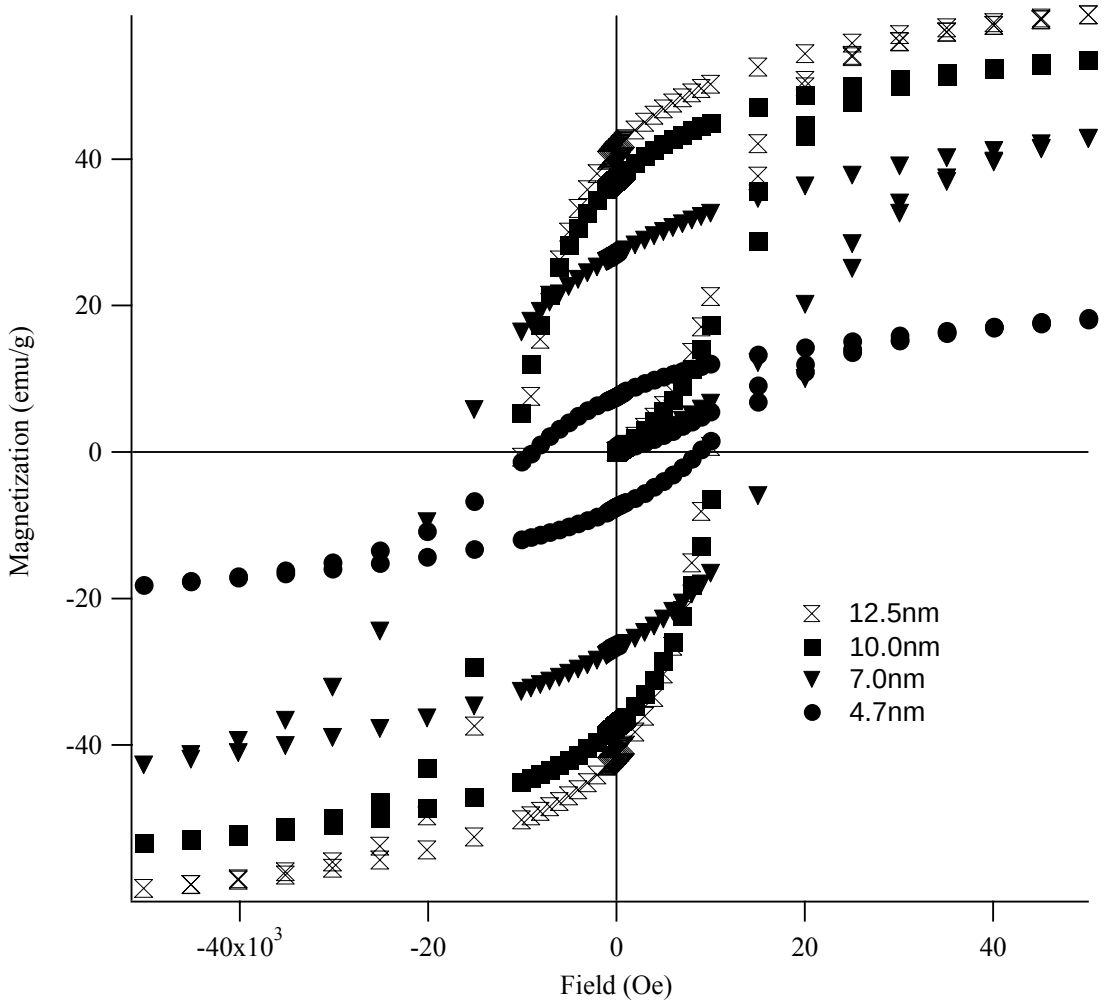

Figure 4.7 Hysteresis loop of various sized $CoSm_{.0191}Fe_{1.981}O_4$ at 5K, 5T. The magnetic field is ramped from zero to 50 kOe then to the same magnitude but in a different direction. Once at the magnetization saturation point, where moments align with the direction of the applied field, the reversal of magnetic moments generates a hysteresis. From the different hysteresis loops, there is a direct correlation between size and M_s. An increase in size produced higher magnetization saturation points and vice versa for smaller sizes. Coercitivity initially increases with size then decreases with increasing size. This may be attributed to initial coherent rotation of magnetic moments followed by spin canting.

As the size of the magnetic nanoparticles is decreased, the anisotropy is decreased. The decrease in anisotropy should decrease the H_c but this linear trend was not observed. From the hysteresis loop (Figure 4.7), an initial increase followed by decrease in H_c was observed. This initial increase may be due to coherent magnetization while the eventual decrease may be attributed to other surface effects. This type of H_c trend was also observed in $CoFe_2O_4$ systems synthesized through seed mediated non-hydrolytic process.[21] The saturation magnetization decreased with decrease in size of the nanoparticles and can be attributed to spin-canting where the magnetic disorder of the moment increases when the particle size decreases and the surface to volume ratio increases.[22-24] The observed M_s data corresponded well to other reported saturation magnetization trends showing a parallel change in saturation magnetization with change in size[22-26].

4.4 Conclusions

We have shown here a method of modulating the magnetic properties of $CoFe_2O_4$. By doping $CoFe_2O_4$ with rare earth metals like samarium, we can alter the blocking temperature and its saturation magnetization as well as its coercitivity through composition and size change. Using different samarium doping percentages, saturation magnetization can be altered by as much as 35.3 emu/g.Oe and the coercitivity can be altered by as much as 4.8 kOe relative to the undoped particle while maintaining similar blocking temperatures. By changing the size of the nanoparticle and maintaining a

constant composition, the blocking temperature can be tuned as well. This systematic study proves that the magnetic behavior and intrinsic properties of $CoFe_2O_4$ can be tuned by addition of samarium. Fundamentally, the ability to finely tune the magnetic properties is of importance. However, the importance of utilizing these tunable magnetic nanoparticles for developing novel materials with adjustable parameters should not be underestimated. There is ample room to explore the properties of novel materials with magnetically and optically tunable properties for biological and physical applications.

4.5 References

(1) Schmid, G. *Clusters and Colloids*; VCG: Weinheim, 1994.

(2) Weller, H. *Angew. Chem. Int. Ed.* **1996**, *35*, 1079.

(3) Shi, J.; Gider, S.; Babcock, K.; Awschalom, D. *Science* **1996**, *271*, 937.

(4) Niemeyer, C. M. *Angew. Chem. Int. Ed.* **2001**, *40*, 4128.

(5) Cullity, B. D. *Introduction to magnetic materials*; Addison-Wesley Publishing Company, Inc.: Reading, 1972.

(6) Kahn, M.; Zhang, J. Z. *Appl. Phys. Lett.* **2001**, *78*, 3651.

(7) Cheng, F.-X.; Jia, J.-T.; Xu, Z.-G.; Zhou, B.; Liao, C.-S. *J. Appl. Phys.* **1999**, *86*, 2727.

(8) Rhyne, J. J.; McGuire, T. *IEEE Transaction of Magnetics* **1972**, *MAG-8*, 105.

(9) Koehler, W. C.; Child, H. R.; Wollan, E. O.; Cable, J. W. *J. Appl. Phys.* **1963**, *34*, 1335.

(10) Behrendt, D. R.; Legvold, S.; Spedding, F. H. *Phys. REv.* **1958**, *109*, 1544.

(11) Strandburg, D. L.; Legvold, S.; Spedding, F. H. *Phys. Rev.* **1962**, *127*, 2046.

(12) Green, R. W.; Legvold, S.; Spedding, F. H. *Phys. Rev.* **1961**, *122*, 827.

(13) Richards, D. B.; Legvold, S. *Phys. Rev.* **1968**, *186*, 508.

(14) Koehler, W. C. *J. Appl. Phys.* **1965**, *36*, 1078.

(15) Lakowicz, J. R., Ed. *Principles of Fluorescence Spectroscopy, 2nd Edition*; Kluwer Academic/Plenum Publishers: New York, 1999.

(16) West, A. R. *Basic Solid State Chemistry, 2nd Edition*; John Wiley & Sons, LTD: New York, 1999.

(17) Gu, H.; Xu, B.; Rao, J.; Zheng, R. K.; Zhang, X. X.; Fung, K. K.; Wong, C. Y. C. *J. Appl. Phys.* **2003**, *93*, 7598.

(18) Rondinone, A. J.; Samia, A. C. S.; Zhang, Z. J. *J. Phys. Chem. B.* **2000**, *104*, 7919.

(19) Stoner, E. C.; Wohlfarth, E. P. *Philosophical Transaction of the Royal Society A* **1948**, *240*, 599.

(20) Rondinone, A. J.; Samia, A. C. S.; Zhang, J. Z. *J. Phys. Chem. B.* **1999**, *103*, 6876.

(21) Song, Q.; Zhang, J. Z. *J. Am. Chem. Soc.* **2004**, *126*, 6164.

(22) Berkowitz, A. E.; Kodoma, R. H.; Makhlouf, S. A.; Parker, F. T.; Spada, F. E.; McNiff Jr., E. J.; Foner, S. *J. Magn. Magn. Mater.* **1999**, *196-197*, 591.

(23) Hochepied, J. F.; Bonville, P.; Pileni, P. *J. Phys. Chem. B.* **2000**, *104*, 905.

(24) Vestal, C. R.; Zhang, J. Z. *Int. J. Nanotechnology* **2004**, *1*, 240.

(25) Coey, J. M. D. *Phys. Rev. Lett.* **1971**, *27*, 1140.

(26) Morrish, A. J.; Haneda, K. *J. Appl. Phys.* **1981**, *52*, 2496.

CHAPTER V

CELLULAR UPTAKE AND MAGNETIC MANIPULATION OF COBALT SPINEL FERRITE – OLIGONUCLEOTIDE CONJUGATES

ABSTRACT

Through surface modifications, magnetic cobalt spinel ferrite nanoparticles, $CoFe_2O_4$, have been conjugated to oligonucleotides and transfected into African green monkey kidney cells (CV-1) and Henrietta Lacks cervical cancer cells (HeLa) using Lipofectamine^{TM}. Sectional laser scanning confocal microscopy studies indicate that transfected $CoFe_2O_4$-oligonucleotide conjugates are localized within the cell. An adverse effect on cell growth was not observed up to 250 hours post transfection. Movement of transfected cells in buffer solution towards an external magnetic field as well as fluorescent illumination in the middle sections of cells demonstrates the feasibility of using $CoFe_2O_4$ for magnetic manipulation of cells. Quantification of cellular uptake

efficiency of $CoSm_{.0.14}Fe_{1.86}O4$ – oligonucleotide conjugates using ICP-OES as a model, demonstrated a four fold increase compared to current literature.

5.1 Introduction

Cellular trafficking is of great importance in the fundamental understanding of cell biology and plays a central role in the delivery of drugs into living cells. A variety of techniques have been developed to improve the transport of poorly permeable molecules across the cell membrane. Protein transduction has been demonstrated to be a promising method for delivering a variety of objects such as small molecule drugs, proteins, and even nanoparticles. Conjugation with peptides and oligocarbamates effectively enhances the uptake of model drugs into cells.[1,2] Gold nanoparticles with a diameter of 20 nm were transported into HepG2 cells after being coated with a shell of bovine serum albumin conjugated to a variety of peptides.[3] Similarly, by using a HIV-tat protein peptide derivative, dextran-coated magnetic nanoparticles of iron oxides were introduced into several cell types such as lymphocyte and HeLa cells. Upon uptake of magnetic nanoparticles, the labeled cells can be readily tracked in vivo by magnetic resonance imaging (MRI).[4-6] Magnetic labeling of cells offers a number of other applications including bio-distribution studies of nanoparticulate carriers *in vivo*[7,8] and cell separation *in vitro* or *in vivo*.[9-12]

With the increasing focus on drug and gene delivery, magnetic nanoparticles have great potential for site specific targeting. Using an external magnetic field, magnetic nanoparticles carrying cargos such as drugs or genes can potentially be guided to or close

to the site of target cells *in vivo*. An added benefit of using magnetic carriers is the possibility of localizing or restricting the bioconjugates to a specified region with an external magnetic field. Recently, an increasing number of studies have been directed towards the investigation of the cellular uptake of magnetic nanoparticle-protein[13,14] and magnetic nanoparticle-peptide[4-8,15-18] conjugates. However, the magnetic nanoparticles used were typically magnetite, Fe_3O_4, or other less defined magnetic nanoparticles. Although magnetite nanoparticles have displayed interesting and useful properties as MRI contrast enhancement agents (e.g. Feridex®), they are relatively weak magnetically when compared to other spinel ferrite nanoparticles like $CoFe_2O_4$ and $MnFe_2O_4$. Using nanoparticles with weak magnetic responses could introduce difficulties when magnetic manipulation and control is necessary. Although $CoFe_2O_4$ and $MnFe_2O_4$ nanoparticles clearly posses advantages in terms of magnetic properties and magnetic interaction, only a few studies on their application in biological systems and their possible adverse effects on living organs have been explored.

This chapter focuses on the potential of $CoFe_2O_4$ nanoparticles as magnetic carriers for therapeutic reagents, specifically, oligonucleotides. Transfection of cobalt spinel ferrite, $CoFe_2O_4$, magnetic nanoparticle-oligonucleotide conjugates into African green monkey kidney epithelial cells (CV-1) and Henrietta Lack human cervical cancer epithelial cells (HeLa) will be discussed. Results illustrate that lipofection, as a method of cationic lipid-mediated DNA transfection, is an effective way to deliver nanoparticles into cells. Observations show that $CoFe_2O_4$ – oligonucleotides did not affect the proliferation cycle or induce any obvious morphological changes. The magnetic response

of $CoFe_2O_4$ internalized by cells is clearly defined by the synchronized cellular movement in buffer with an external magnetic field.

5.2 Experimental

5.2.1 Cell Lines and Medium Preparation

Henrietta Lacks cervical cancer cells, HeLa, were first isolated from the cervix of Henrietta Lacks back in 1951. Since then numerous research studies have been conducted sometimes with unreliable data. Since HeLa cells are immortal cells and grow very rapidly in cell cultures, they tend to invade other cell lines if careful aseptic practice is not observed. Karyotype analysis show that there are actually multiple different HeLa cell types. This can be attributed to the malignancy of the cell and it progress in different environment. Due to the variables that can be generated from one batch of cells to another in malignant cells, most cellular analysis experiments are now conducted with both malignant and non-malignant cells for comparison.

African green monkey cells, CV-1, are cultivated from the kidney epithelial cells of male African green monkeys. These are non-malignant primary cells that have been cultivated to grown continuously through several generations. Since they are primary cell lines, after a finite number of generations, CV1 cells will no longer proliferate normally or may cease to proliferate. However, since they are non-malignant and easy to transfect, they are good candidates for cellular analysis experiments.

Green monkey kidney cells and human cervical cancer cells were grown and passaged in Dubelcco's Modified Eagles Medium (DMEM) supplemented with 10% defined bovine calf serum (CBS) and 1% penicillin streptomycin. Both basal mediums were sterile filtered with a 0.2μm pore size filter. During transfection, an indicator free media with significantly reduced serum, OptiMem, was used to reduce possible reactions with sera proteins.

5.2.2 Preparation of Magnetic Nanoparticle – Oligonucleotide Conjugates

The target is to functionalize cobalt spinel ferrite or samarium doped cobalt spinel ferrite nanoparticles with a functional group that will act as a point of attachment to macromolecules like DNA. Superparamagnetic $CoFe_2O_4$ and $CoSm_{0.14}Fe_{1.86}O_4$ nanoparticles were synthesized using a normal micelle method (see Chapter 4.2.1).[19] The surface of 10nm magnetic nanoparticles were first activated with concentrated NaOH then functionalized with epichlorohyrin followed by amination with NH_4OH. Amine functionalized magnetic nanoparticles were then isolated through several washes with DMSO and magnetic separations. Subsequently, a commercially available linker group, *N*-succinimidyl 3-2[pyridyldithiol]proprionate (SPDP), was attached to the surface through an amide bond. Magnetic nanoparticles-SPDP conjugates were then subjected to several washes with phosphate buffered saline (PBS), magnetically separating after each wash. Thiol-terminated oligonucleotide with a random sequence of 5'-HS-$(CH_2)_6$-GTA AAA CGA CGG CCA GAG-3' (oligonucleotide **1**) or oligonucleotide **3** (5'-HS- AAA CGA CGG CCA GAG-3'-FAM) were reduced with Cleland's reagent (immobilized

dithiolthreitol) and then attached to the surface through a thiol exchange reaction with the surface crosslinker overnight. Oligonucleotides of the magnetic nanoparticle – oligonucleotide **1** conjugates were then hybridized with their complimentary strand tagged with fluorescein, 5'-CAC TGG CCG TCG TTT TAC – 3' – FAM (oligonucleotide **2**) in PBS at temperatures above is melting temperature (T_m = 60°C) for 30 minute and then allowed to cool to room temperature slowly so the two strands can anneal. Hybridized magnetic nanoparticle – oligonucleotide **1-2** conjugates resulted in a total of DNA concentration of 300ng.

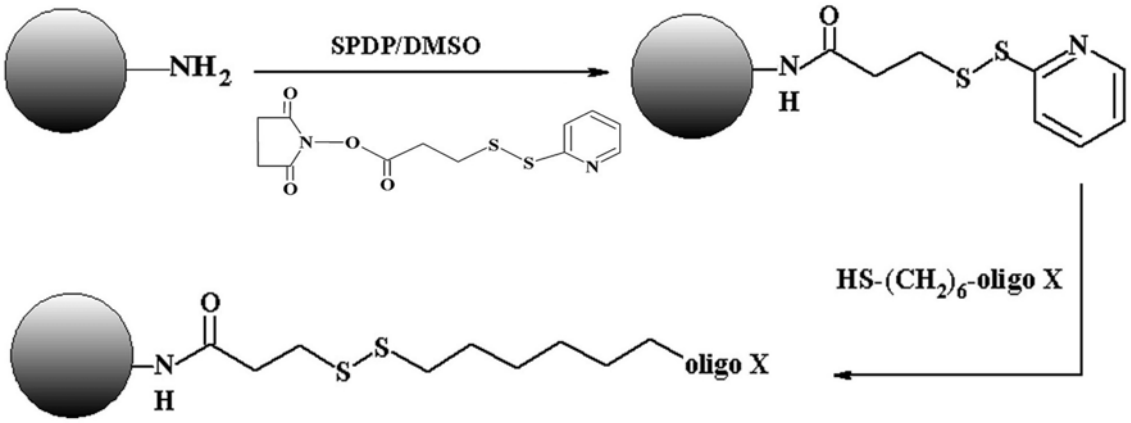

Figure 5.1 Schematic representation of the crosslinking chemistry behind mnp-oligo conjugates. An amino functionalized magnetic nanoparticle is reacted with the maleimide group of SPDP leaving the thiol reactive terminus of the crosslinker exposed and unreacted. In the presence of reduced thiol-terminated oligonucleotides, a thiol-thiol exchange between the thiol terminus of the oligo and the disulfide bond of the crosslinker occurs forming a new disulfide bond.

the formula of $CoFe_2O_4$ – oligo **1-2** or $CoSm_{0.14}Fe_{1.86}O_4$– oligo **1-2** (see Figure 5.1). Magnetic nanoparticle – oligonucleotide **3** was transfected along with and additional 100ng of β-Galactosidase reporter gene for a total of 300ng of DNA.

5.2.3 Transfection of Magnetic Nanoparticle – oligonucleotide conjugates into Cells.

As specified earlier, there are multiple methods for cellular delivery of genes. We have chosen to use transfection. There are two classes of transfection, physical and chemical transfection. Direct microinjection, electroporation, and biolistic particle delivery are all physical methods. With direct microinjection, as its name implies, genes are directly injected into cells. For example, Cappechi demonstrated that using microinjection methods, DNA can be transferred to stem cells.[20] Electroporation is primarily used for plant cells where an electrical pulse is used to perturb the membrane for DNA transfer.[21] In bioloistic methods, genetic material is transferred into recipient cells via a high velocity microprojectile.[22] Physical transfection relies on physically transferring the DNA into individual cells and is labor intensive, especially for a high cell count. Chemical transfection is more appropriate for DNA transfer into many cells. Examples of chemical transfection include DEAE-dextran association, co-precipitation with calcium phosphate, and transfection facilitated by artificial liposomes. Using DEAE-dextran, an excess of positive charge is introduced allowing DNA electrostatically associated with DEAE-dextran to be chaperoned into cells.[23,24] Through enodcytosis, calcium chloride / DNA co-precipitates can be taken up. Artificial liposomes, introduced

in the late 1980s, offer high transfection efficiency and can be used with cell lines that do not tolerate other chemical transfection reagents.[25] Due to the high popularity of artificial liposome, readily available protocols and reagents have been established.[26,27]

Lipofectamine™, a commercially available synthetic polycationic lipid was used as the transfecting agent to facilitate the transport of cobalt spinel ferrite – oligo conjugates and samarium doped cobalt spinel ferrite – oligo conjugates across the cell membrane. Lipofectamine™ has a chemical makeup of 3:1 ratio 2,3-dioleylexy-N-[2(sperminecarboxamideo)ethyl]-N,N-dimethyl-1-propanamium trifluoroacetate (DOPA) and dioleyl phophatidylethanolamine (DOPE).[28] Lipofectamine™ is supplied as a concentrated solution so it was diluted with OptiMem (a reduced serum media) before use then allowed to complex electrostatically with the oligonucleotides on the surface of $CoFe_2O_4$. This complex was then introduced to cells grown on glass coverslips in a reduced serum media for approximately 7-10 hours at 37°C and 5% CO_2. After internalization, the media was replaced with a growth media, DMEM supplemented with 10% Calf Bovine serum and 1% Penicillin Streptomycin glutamate. An illustration of the transfection method used can be seen in Figure 5.2. For the 96hr and 250 hr studies, cells were trypsinized then passaged and grown in a new plate on coverslips.

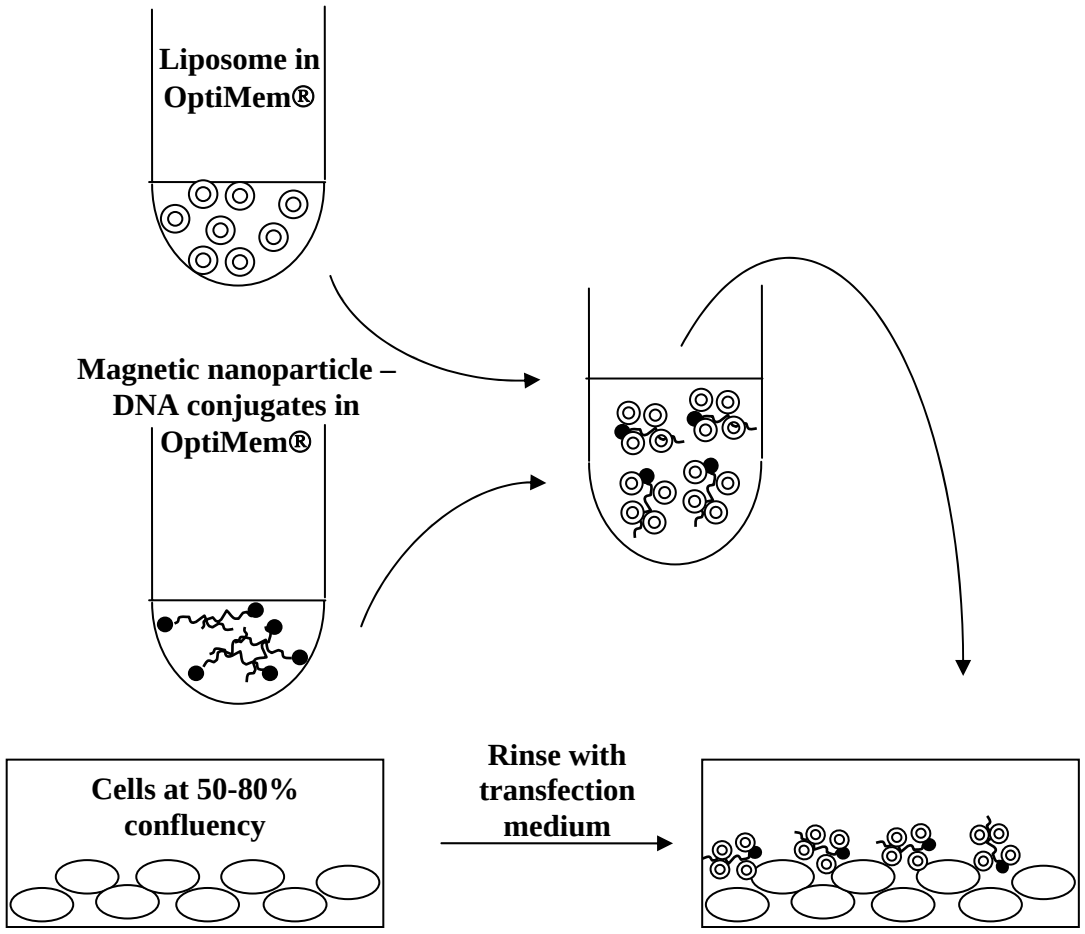

Figure 5.2 Illustration of the general protocol for transfection with Lipofectamine™. Figure adapted from reference 28.

5.2.4 Transfection Control Experiments

Several sets of control experiments were conducted to ensure that observations and interpretations made were conclusive. To demonstrate that transfection reagents are required to transport negatively charged species across the membrane, control experiments were carried out without Lipofectamine.™ In the first category, CV -1 cells were incubated with either (a) $CoFe_2O_4$ nanoparticles, (b) $CoFe_2O_4$ mixed with fluorescein labeled oligonucleotides, or (c) cobalt spinel ferrite conjugated to fluorescein labeled oligonucleotide were incubated with cells in OptiMem®. To demonstrate that only $CoFe_2O_4$ – oligonucleotide conjugates were being taken up by cells when Lipofectamine™ is used, (a) $CoFe_2O_4$ nanoparticles, (b) $CoFe_2O_4$ mixed with oligonucleotides, or (c) fluorescein labeled oligonucleotides were allowed to complex with Lipofectamine™ then incubated with CV -1 cells in OptiMem®.

5.2.5 Confocal Microscopy and Dark Field Microscopy

To ensure that cells grown on coverslips retain their cellular constituents, "fixation" is required. When cells are removed from their native or optimal condition, autolysis initiates. In autolysis, intracellular enzyme begins to breakdown the proteins in the cell eventually liquefying the cell.[29,30] There are many choices of fixatives available, such as aldehydes, osmium tetroxide, chromic acid, alcohol, mercuric chloride, and acetone. The most commonly used fixative is a low concentration formaldehyde solution.

A 4% *p*-formaldehyde solution was used in this study. The fixation mechanism is not well understood but proposed to be some sort of crosslinking reaction between the aldehyde and proteins through amino acids and functional groups such as amido, guanidyl, carboxyl, SH, and hydroxyl groups on protein surface.[29] The crosslinking provides mechanical strength retaining cellular constituents during progressive experimental steps. In the experiments described in this chapter, growth medium is removed then cells are washed with PBS. Next, they are immersed in a buffered 4% paraformaldehyde, gently agitated for 15-20 minutes, and then rinsed with PBS before mounting onto microscope slides with Paramount G (to reduce in photobleaching of fluorescence). A Zeiss confocal microscope housed with Argon laser was used for imaging cells transfected with magnetic nanoparticle – oligo conjugates. Since confocal microscopy allots for multiple plane focusing, z-stack or z-sectional images were collected at set micron increments, typically at 1.0 – 2.0 μm increments. This provided information on the approximate location of the $CoFe_2O_4$ – oligo conjugates in the cell. Sample preparation for darkfield microscopy was essentially the same as those for confocal microscopy except coverslips were directly mounted onto microscope stage. Dark field micrographs of the native cells, $CoFe_2O_4$ – oligo conjugates, and of cells transfected with $CoFe_2O_4$ – oligo conjugates were taken with a Olympus IX 70 inverted microscope housed with a darkfield condenser / objective pair.

5.2.6 Inductively Coupled Plasma – Optical Emission Spectrometry of Uptaken Magnetic Nanoparticle.

CV-1 cells transfected with $CoSm_{0.14}Fe_{1.86}O_4$– oligoX (X = **1-2** or **3**) were washed thoroughly, trypsinized, suspended in buffer, then manually counted on a hematocytometer (see Figure 5.3). Cell suspensions were then stored in a freezer overnight then thawed before use. This extreme change in environment causes cells to lyse. Cell suspensions were then magnetically separated, washed with 1% HNO_3, and magnetically separated. The magnetically separated precipitate was then digested in a parbomb with HNO_3 (trace metal grade) at 120°C for 24 hours. The digested sample was then diluted 1:100 or 1:200 with optima grade water before ICP-OES analysis.

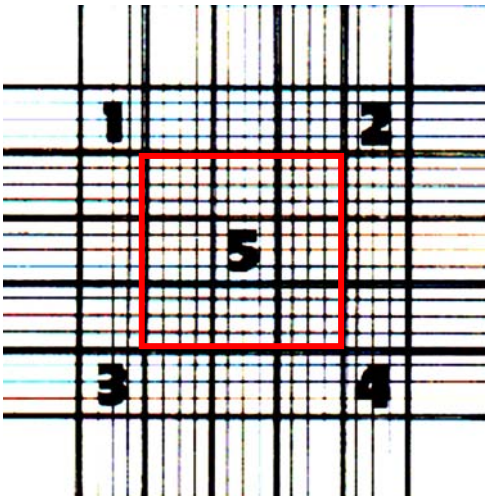

Figure 5.3 Grids of a hemacytometer. The number of cells in region 5 represents the number of cells, n, present in 0.1 μL. Hence, the total number of cells per 1 mL is n x 10^4.

5.3 Results and Discussion

5.3.1 Crosslinking of $CoFe_2O_4$ to oligonucleotides

Using a commercially available heterofunctional crosslinker, SPPD, with amine and thiol reactive termini, we have crosslinked oligonucleotides to the activated surface of magnetic nanoparticles. As mentioned in the section 5.2.2, activation $CoFe_2O_4$ followed by reacting with epichlorohydrin then amination with NH_4OH yielded magnetic nanoparticles with an amine functionalized surface. Amine is then reacted with the maleimide group of SPDP leaving the thiol terminus reactive. Oligonucleotides with thiol modifications were then reduced and attached to the surface through a thiol-thiol exchange. We did not verify the surface coverage of oligonucleotides on $CoFe_2O_4$ nanoparticles but estimate that it should resemble the grafting density of benzoic acid on $CoFe_2O_4$ nanoparticles (1.20 molecules/nm^2).[31]

5.3.2 Lipofection of $CoFe_2O_4$ – oligonucleotide conjugates into HeLa and CV-1 cells

The internalization of $CoFe_2O_4$ – oligonucleotide conjugates by HeLa and CV-1 cells were monitored by the fluorescence from the fluorescein tag on oligonucleotides. Using a confocal microscope, z-stack images were taken at 1-2 μm interval starting from the bottom portion of the cell to the top portion of the cell. From the overlaid (fluorescence over brightfield) image in figure 5.4., the presence of fluorescence at the

middle sections of the cell and the absence of fluorescence at the beginning and latter sections of the cell indicated that $CoFe_2O_4$-oligonucleotides are internalized by HeLa cells. Similarly, the same pattern of luminescence can be observed in CV-1 cells (Figure 5.5). For comparison purposes, native HeLa and CV-1 cell confocal micrographs are shown in Figures 5.6 and 5.7. To verify that the dark spots, seen in the cytoplasm, in all of the confocal overlay images were aggregates of $CoFe_2O_4$, we repeated the transfection experiment and took darkfield micrographs of native CV-1 cells, $CoFe_2O_4$ – oligo clusters, and CV – 1 cells transfected with $CoFe_2O_4$ – oligos (Figure 5.8). Based on the darkfield micrographs, it is clear that the dark spots we see in confocal micrographs correlates to clusters of aggregated magnetic nanoparticles. Additionally, we also transfected CV-1 cells with $CoFe_2O_4$ – oligo conjugates where oligonucleotides were not fluorescently labeled. Confocal micrograph taken at 1μm interval showed dark spots within the cytoplasm and around the nucleus (see Figure 5.9) similar those seen in other confocal micrographs of cells transfected with $CoFe_2O_4$ – oligo conjugates.

To verify that the $CoFe_2O_4$ – oligo conjugate remained intact during lipofection and to demonstrate the magnetic control, parallel experiments were carried out but instead confocal images, brightfield and/or fluorescent images were collected. Cells were detached from the coverslip to form a suspension then magnetically separated and washed with PBS. Using a small laboratory Nd-Fe-B magnet, brightfield images of cells moving in response to a magnetic field was observed (Figure 5.10). We repeated the experiment taking several hundred frames (millisecond intervals) of the cells responding to the magnetic field and collectively constructed a short movie in Figure 5.11 (heintz_eva_l_200412_phd_magneticmovement1.mpg). Since these frames were

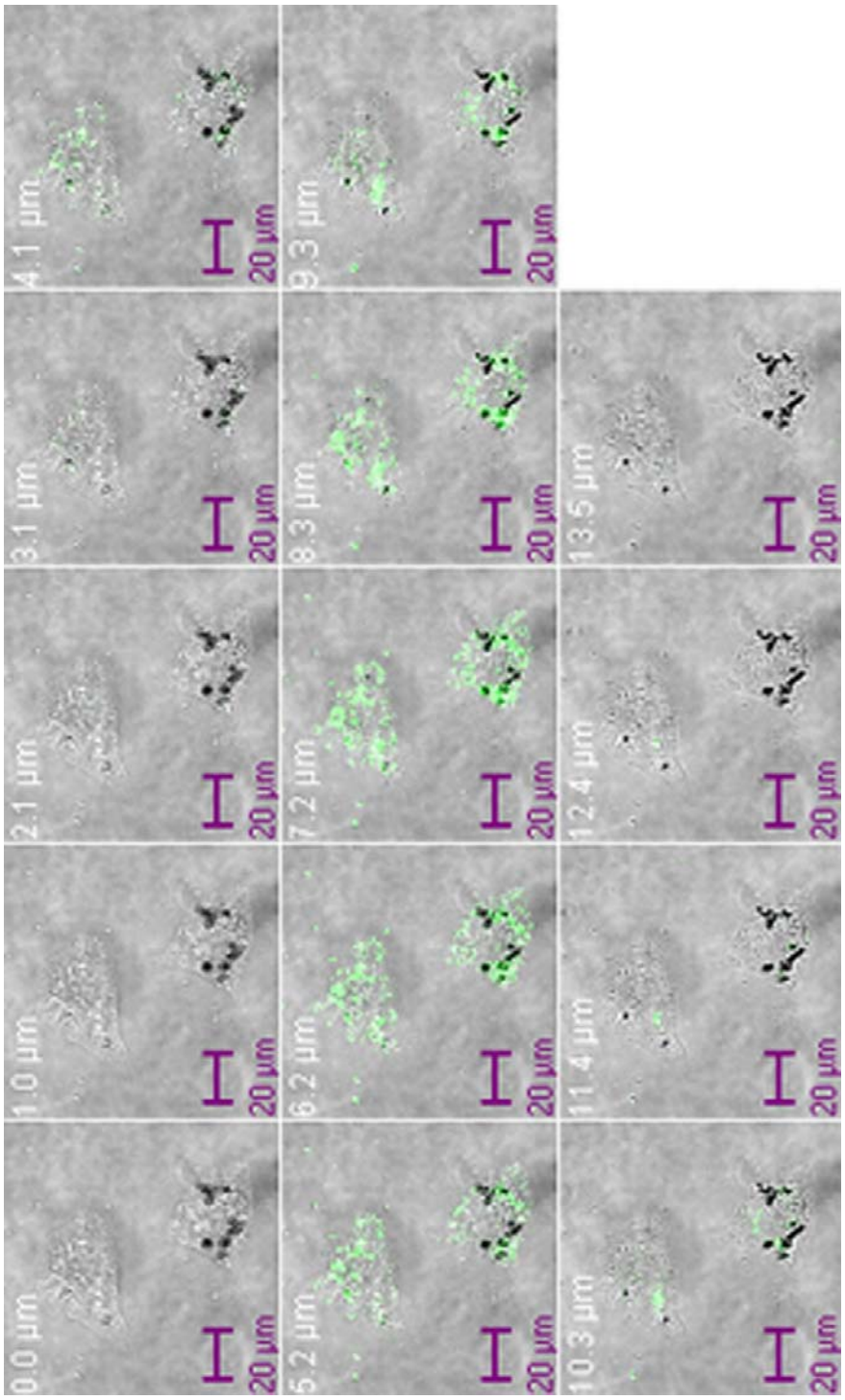

Figure 5.4. HeLa cells transfected with $CoFe_2O_4$ – oligonucleotide **3**

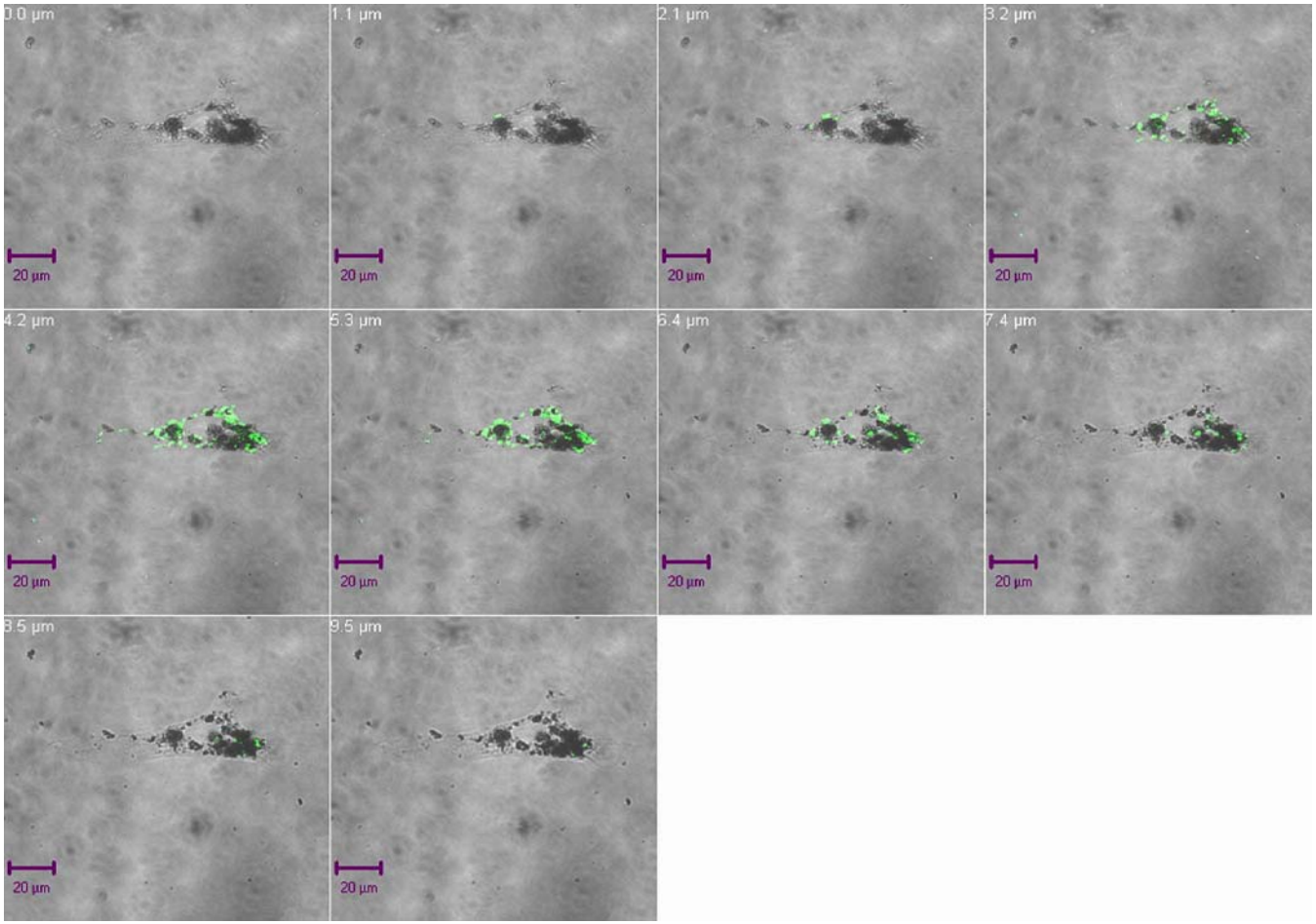

Figure 5.5 CV-1 cells transfected with $CoFe_2O_4$ – oligonucleotide **3**

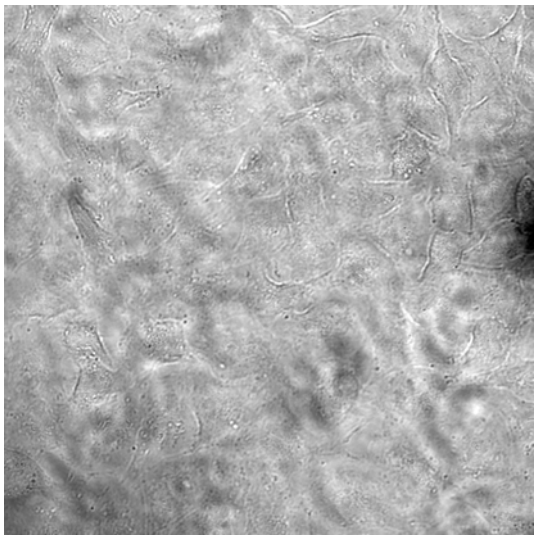

Figure 5.6 Confocal image of native HeLa cells.

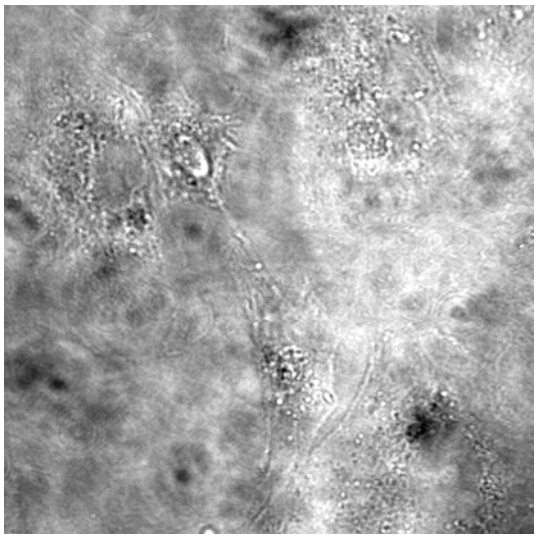

Figure 5.7 Confocal image of native CV1 cells.

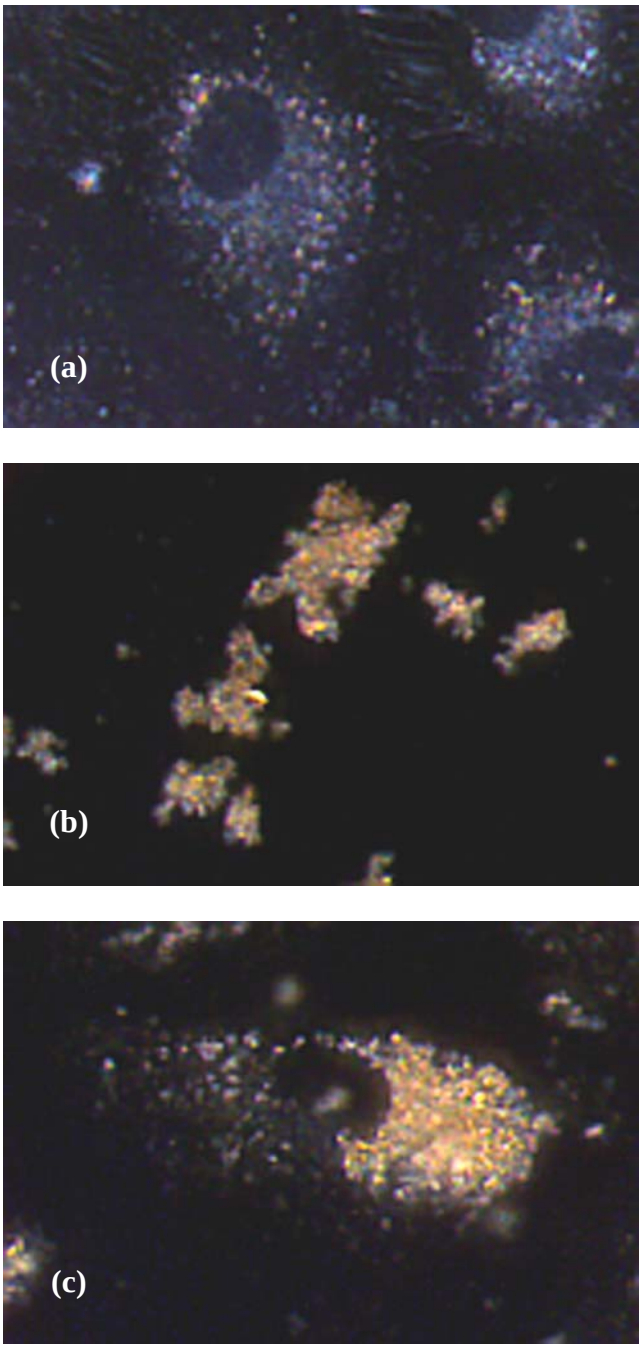

Figure 5.8 Darkfield micrographs of (a) native CV – 1 cells, (b) $CoFe_2O_4$ – oligo clusters, (c) CV – 1 cells transfected with $CoFe_2O_4$ – oligos.

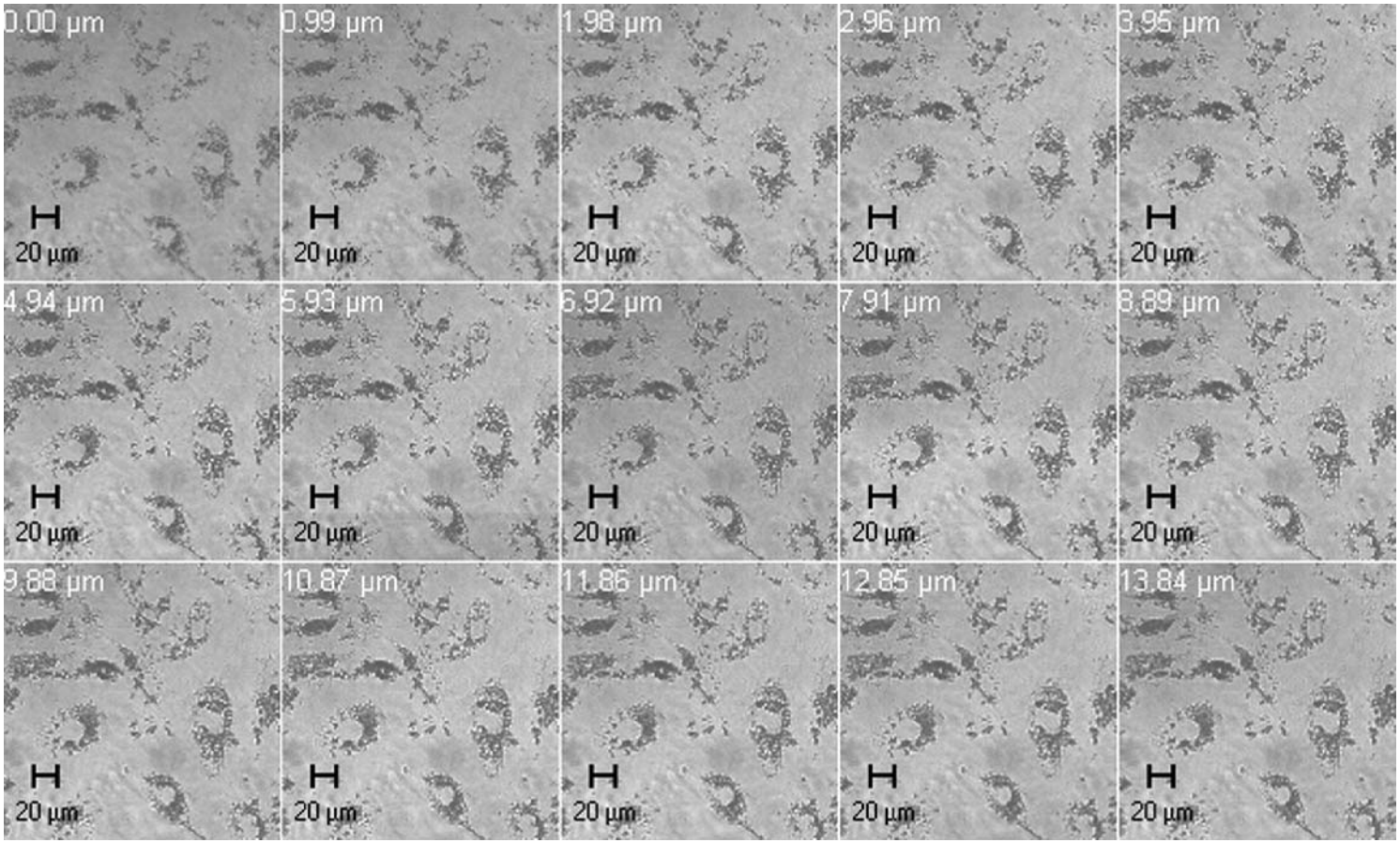

Figure 5.9 Confocal Micrograph of CV-1 cells transfected with $CoFe_2O_4$ –oligo conjugates where oligonucleotides were not fluorescently labeled.

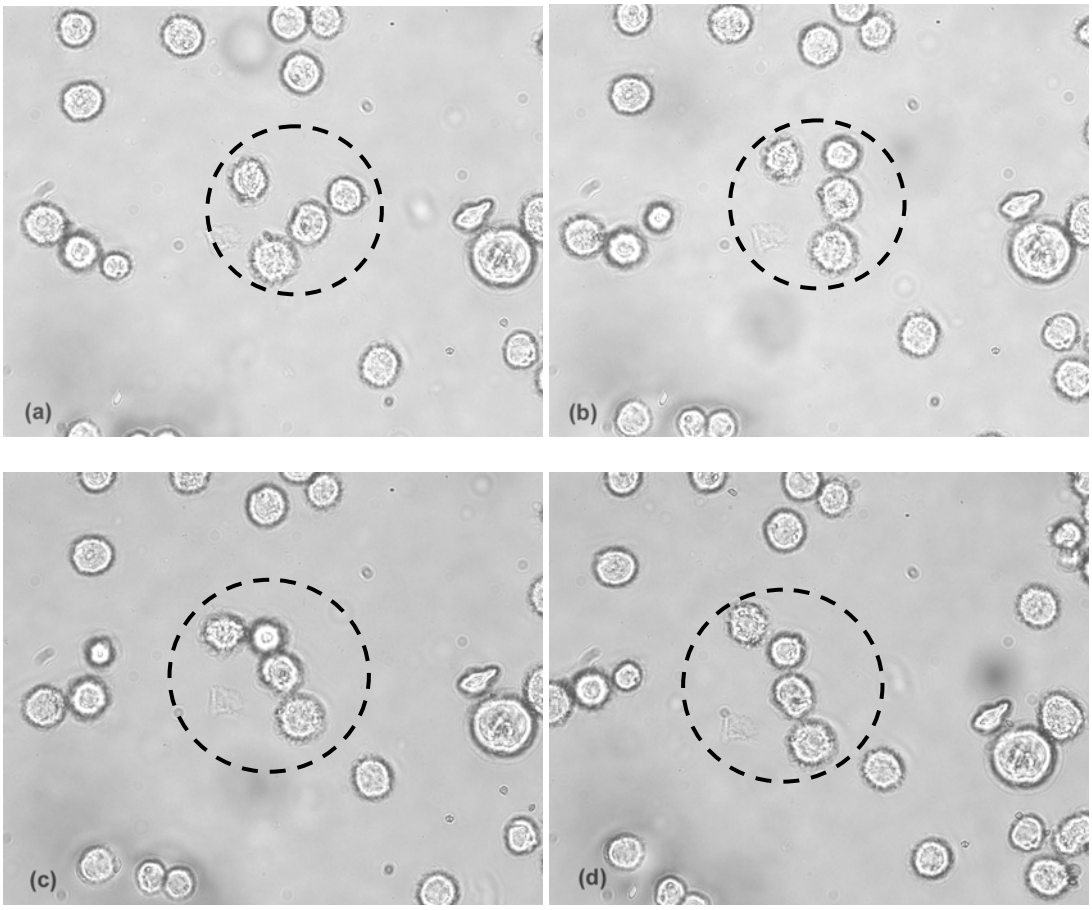

Figure 5.10 Synchronized movement of HeLa cells
(transfected with $CoFe_2O_4$ – oligonucleotides) with external magnetic field

Figure 5.11 Movie of cells responding to the magnetic field.
(heintz_eva_l_200412_phd_magneticmovement1.mpg Click tag)

collected with a fluorescence microscope, the presence of green luminescence in the cells confirms that the oligonucleotides remained intact during transfection. Based on calculations (see Appendix A), the amount of magnetic force exerted by the magnet on each cell 5.08 cm away (magnetic gradient of 6.4 T/m) in a static environment is estimated to be 61.1 x 10^{-17} N. The hemadynamic force that counteracts the magnetic force is estimated to be 1.42 nN. Hence, it is not likely that these magnetic nanoparticles can be controlled in a flowing system. The proximity of the source of magnetic field to the target needs to closer (around 1 cm) and the applied field must be greater than 0.3 T for localization of magnetic carriers in a blood capillary flow rate.

Several sets of control experiments were conducted to ensure proper interpretation of data. When $CoFe_2O_4$ nanoparticles were incubated with CV -1 cells in OptiMem® without Lipofectamine™, uptake was not observed by the absence of movement with an external magnetic field. When $CoFe_2O_4$ nanoparticles were mixed with fluorescence labeled oligonucleotides or conjugated to fluorescence labeled oligonucleotides then incubated with cells in OptiMem® without Lipofectamine™, absence of movement with magnetic field was observed. In addition, fluorescence was not observed in any confocal micrographs. These results indicate that a facilitating reagent like Lipofectamine™ is required to deliver negatively charged species across the membrane.

When $CoFe_2O_4$ nanoparticles were mixed with Lipofectamine™ then incubated with cells in OptiMem®, a magnetic response to an external magnet was not observed indicating that nanoparticles were not taken up by cells. This means that $CoFe_2O_4$ nanoparticles are not be complexed to the liposomes, hence, they are not transported into cells. As discussed in the section 5.2.3, Lipofectamine™ facilitates the transport of genes.

To confirm that Lipofectamine™ is not facilitating in the transport of $CoFe_2O_4$ nanoparticles in the presence of free oligonucleotides, $CoFe_2O_4$ nanoparticles were mixed with fluorescein labeled oligonucleotides, complexed to Lipofectamine™, then incubated with host cells. Confocal micrograph (Figure 5.12) showed luminescence but a cell suspension for this control experiment did not exhibit any magnetic response. Hence, the oligonucleotide is taken up by cells but not the nanoparticles.

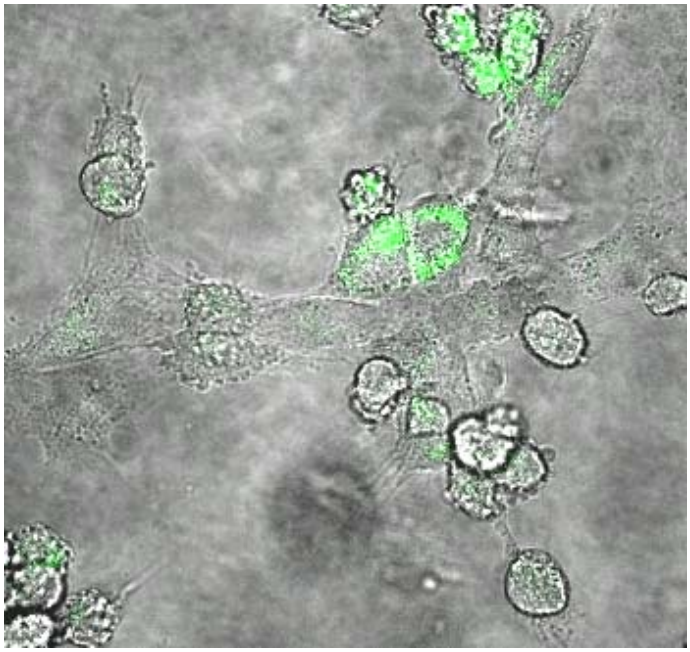

Figure 5.12 Confocal micrograph of CV-1 cells incubated transfected with $CoFe_2O_4$ nanoparticle mixed (not conjugated to) with fluorescein labeled oligonucleotides.

For further verification and comparison, fluorescein labeled oligonucleotides without nanoparticle were allowed to complex to liposomes then incubated with host cells. Once again, the confocal micrograph indicated fluorescence (Figure 5.13) and as expected, the cell suspension of this control experiment did not exhibit a magnetic response to an external magnet.

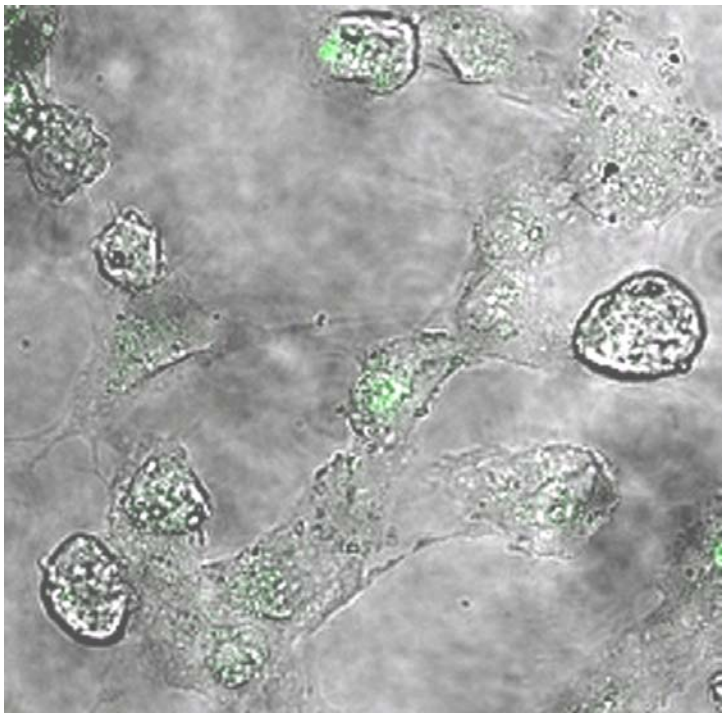

Figure 5.13 Confocal micrograph of CV-1 cells transfected with fluorescein labeled oligonucleotides without the presence of magnetic nanoparticles.

To investigate the transfection efficiency, transfection experiments of $CoFe_2O_4$ – oligonucleotide conjugates were repeated. Based on visual inspection with fluorescence image shown in Figure 5.14, an efficient transfection can be estimated. Initial quantification by flow cytometry of fluorescence population versus native cells provided inconclusive results. Furthermore, flow cytometry relies on fluorescence. We are primarily interested in the number of nanoparticles taken up along with the oligonucleotides attached. To quantify the efficiency, lipofection of $CoSm_{0.145}Fe_{1.855}O4$– oligo conjugates into CV-1 cells was carried out to mimic the transfection of $CoFe_2O_4$ – oligonucleotide conjugates. Samarium doped cobalt spinel ferrites, $CoSm_{0.145}Fe_{1.855}0_{4,}$ were chosen since Sm ions are not present in the medium that cells are cultivated in and behave similarly to $CoFe_2O_4$. From ICP results, we calculated based on Co and Fe that the number of $CoSm_{0.14}Fe_{1.86}O4$ taken up by CV-1 cells is 2.74×10^8 particles and 2.89×10^8 particles respectively. That is a ten fold increased efficiency compared to the reported $1.27 X10^7$ Fe particles per cell.[32] However, since, ICP is a trace metal analysis instrument, the possibility of preexisting Co and Fe present may inflate the actual concentration of Co and Fe detected. To eliminate such erroneous results, we chose to detect samarium. From ICP-OES, we calculated that the amount of Sm present in each cell is 4.44×10^7 $CoSm_{0.14}Fe_{1.86}O_4$. This is almost a four time improvement to the highest reported uptake value.

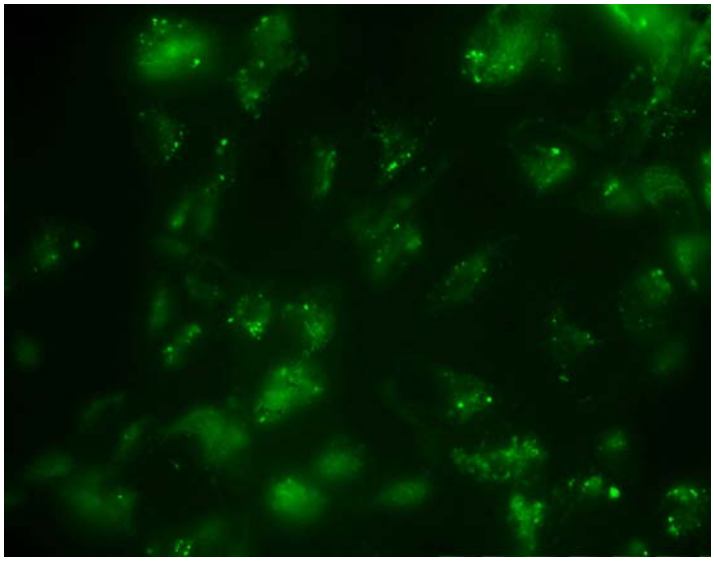

Figure 5.14 Fluorescence micrograph of CV-1 cells transfected with $CoFe_2O_4$ – oligonucleotide conjugates demonstrating the transfecting efficiency.

For the purpose of monitoring possible adverse effects that may be imposed on cells post transfection, confocal micrographs of transfected cells were taken 24hrs, 48hrs, 96hrs, and 250hrs post transfection (see Figure 5.15). By comparing Figures 5.15a-d, it is obvious that morphological change is not present. However, there is a slight dilution of fluorescent luminescence in cells that have been transfected and passaged multiple times.

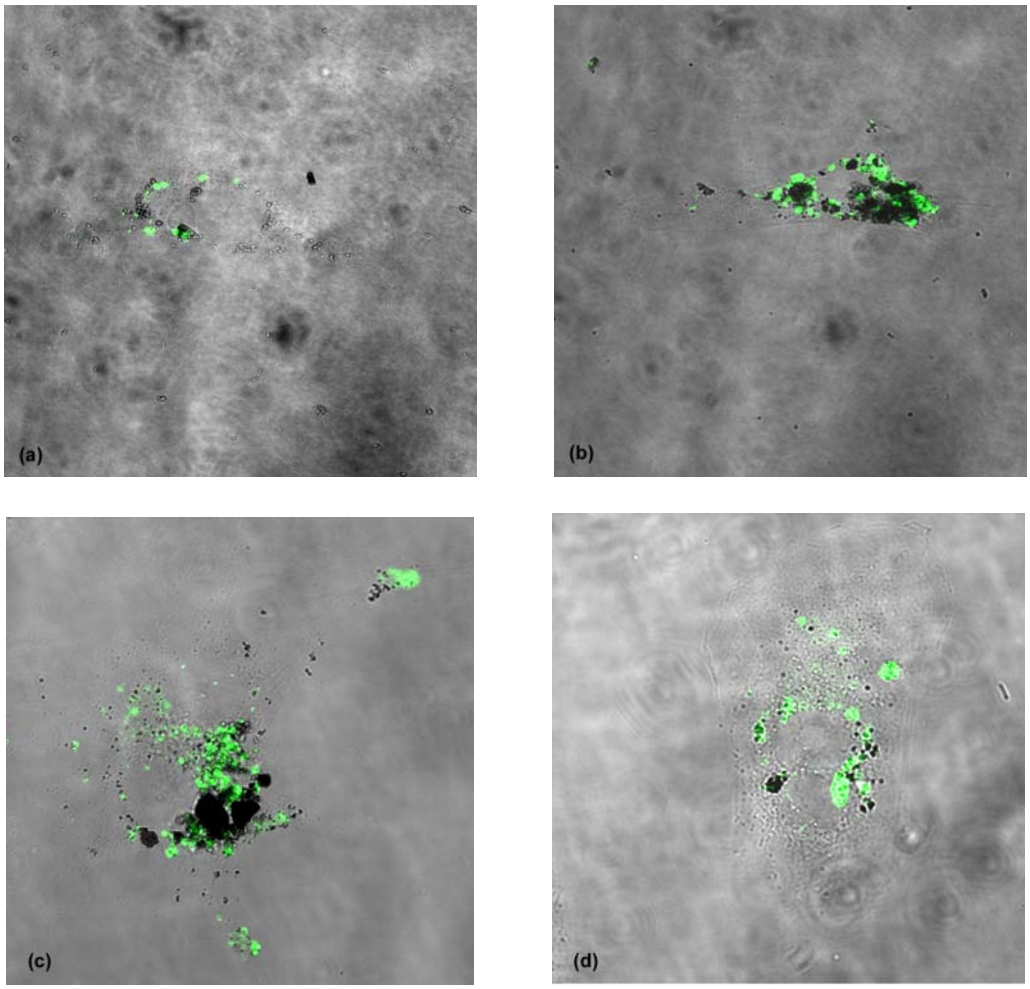

Figure 5.15 Reflective and fluorescent overlay confocal images of CV-1 cells (a) 24hrs, (b) 48hrs, (c) 96hrs, (d) 250hrs post transfection.

5.4 Conclusion

In conclusion, $CoFe_2O_4$ – oligonucleotide conjugates have been delivered into mammalian cell lines through transfection. The cellular uptake proves to be at least four times higher than reported values demonstrating an increase in uptake efficiency. Observations indicated that magnetic nanoparticles pose no adverse effect to cells *in vitro* as cells continued to proliferate normally without morphological changes up to 250 hours post transfection. Synchronized movement in response to magnetic force clearly illustrated the potential of using magnetic nanoparticles such as $CoFe_2O_4$ as carriers for drugs, genes, and other therapeutic reagents for localized treatments. Additionally, magnetic nanoparticles coupled to oligonucleotides or other macromolecules can be used for sub-cellular tracking. If the source of a magnetic field is relatively close in proximity to the magnetic cargo, force approximation calculations show that there is great potential for guided delivery and localized treatment.

As mentioned in section 5.3.1, we did not verify the surface coverage of oligonucleotides on $CoFe_2O_4$ nanoparticles but predict that it will resemble the grafting density of benzoic acid on $CoFe_2O_4$ nanoparticles. Hence, it would be interesting to study the surface coverage of oligonucleotides on $CoFe_2O_4$ nanoparticles to determine the maximum packing density. In addition, it would also be interesting to see how the uptake efficiency can be improved. The use of magnetic nanoparticles as chaperones for guided delivery and localized treatment has received a lot of attention but will require further studies to optimize *in vivo* conditions.

5.5 References

(1) Wender, P. A.; Rothbard, J. B.; Jessop, T. C.; Krider, E. L.; Wylie, B. L. *J. Am. Chem. Soc.* **2002**, *124*, 13382.

2) Wender, P. A.; Mitchell, D. J.; Pattabiraman, K.; Pelkey, E. T.; Steinman, L.; Rothbard, J. B. *Proc. Natl. Acad. Sci. USA* **2000**, *97*, 13003.

(3) Tkachenko, A., G.; ; Xie, H.; Coleman, D.; Glomm, W.; Ryan, J.; Anderson, M. F.; Franzen, S.; Feldheim, D. L. *J. Am. Chem. Soc.* **2003**, *125*, 4700.

(4) Zhao, M.; Kircher, M. F.; Josephson, L.; Weissleder, R. *Bioconjugate Chem.* **2002**, *13*, 840.

(5) Koch, A. M.; Reynolds, F.; Kircher, M. F.; Merkle, H. P.; Weissleder, R.; Josephson, L. *Bioconjugate Chem.* **2003**, *14*, 1115.

(6) Josephson, L.; Tung, C.-H.; Moore, A.; Weissleder, R. *Bioconjugate Chem.* **1999**, *10*, 186.

(7) Lewin, M.; Carlesso, N.; Tung, C.-H.; Cory, D. T.; Scadden, D. T.; Weissleder, R. *Nature Biotechnology* **2000**, *18*, 410.

(8) Wunderbaldinger, P.; Josephson, L.; Weissleder, R. *Bioconjugate Chem.* **2002**, *13*, 264.

(9) Yeh, T. C.; Zhang, W.; Ildstad, S. T.; Ho, C. *Magn. Reson. Med.* **1993**, *30*, 617.

(10) Yeh, T. C.; Zhang, W.; Ildstad, S. T.; Ho, C. *Magn. Reson. Med.* **1995**, *33*, 200.

(11) Schoepf, U.; Marecos, E.; Melder, R.; Jain, R.; Weissleder, R. *BioTechniques* **1998**, *24*, 642.

(12) Handgretinger, R.; Lang, P.; Schumm, M.; Taylor, G.; Neu, S.; Koscielnak, E.; Niethammer, D.; Klingegiel, T. *Bone Marrow Transpl.* **1998**, *21*, 987.

(13) Weissleder, R.; Moore, A.; Mahmood, U.; Bhorade, R.; Benveniste, H.; Chiocca, E. A.; Basilion, J. P. *Nature Medicine* **2000**, *6*, 351.

(14) Bulte, J. W. M.; Zhang, S.-C.; van Gelderen, P.; Herynek, V.; Jordan, E. K.; Duncan, I. D.; Frank, J. A. *Proc. Natl. Acad. Sci. USA* **1999**, *96*, 15256.

(15) Futaki, S. *International Journal of Pharmaceutics* **2002**, *245*, 1.

(16) Martin, S. E.; Peterson, B. R. *Bioconjugate Chem.* **2003**, *14*, 67.

(17) Buschle, M.; Schmidt, W.; Zauner, W.; Mechtler, K.; Trska, B.; Kirlappos, H.; Birnstiel, M. L. *Proc. Natl. Acad. Sci. USA* **1997**, *94*, 3256.

(18) Umezawa, N.; Gelman, M. A.; Haigis, M. C.; Raines, R. T.; Gellman, S. H. *J. Am. Chem. Soc.* **2002**, *124*, 368.

(19) Rondinone, A. J.; Samia, A. C. S.; Zhang, Z. J. *J. Phys. Chem. B.* **1999**, *103*, 8676.

(20) Cappechi, M. R. *Cell* **1980**, *22*, 479.

(21) Wong, T. K.; Neumann, E. *Biochem. Biophys. Res. Commun.* **1982**, *107*, 584.

(22) Ye, G. M.; Danielle, H.; Sanford, J. C. *Plant Molec. Biol.* **1990**, *15*, 809.

(23) Vaheri, A.; Pagano, J. S. *Virology* **1965**, *27*, 434.

(24) McCutchan, J. H.; Pagano, J. S. *J. Natl. Cancer Inst.* **1968**, *41*, 351.

(25) Felgner, P. L.; Gadek, T. R.; Holm, M.; Roman, R.; Chan, H. W.; Wenz, M.; Northrop, J. P.; Ringold, G. M.; Danielsen, M. *Proc. Natl. Acad. Sci. USA* **1987**, *84*, 7413.

(26) Meyers, R. A., Ed. *Molecular Biology and Biotechnology: A Comprehensive Desk Reference*; VCH Publishers, Inc.: New York, 1995.

(27) Freshney, R. I. *Culture of animal cells*; Fourth ed.; Wiley-Liss, Inc.: New York, 2000.

(28) www.invitrogen.com.

(29) Woods, A.; Ellis, R. C. *Laboratory Histopathology: A Complete Reference*; Churchill Livingston: New York, 2000.

(30) www.path.ed.ac.uk/imaging/techniques/microscopy/fix.htm **2003**.

(31) Vestal, C. R. In *Chemistry and Biochemistry*; Georgia Institute of Technology: Atlanta, 2004.

(32) Josephson, L.; Tung, C.-H.; Moore, A.; Weissleder, R. *Bioconjugate Chem.* **1999**, *10*, 186.

CHAPTER VI

SURFACE MODIFICATION OF COBALT AND MAGNANESE SPINEL FERRITE FOR CELLULAR DELIVERY

Abstract

Spinel ferrites such as $CoFe_2O_4$ and $MnFe_2O_4$ have been crosslinked to oligonuceleotides and 1-H-Pyrazole-1-carboximide (HPC) through heterofunctional crosslinker, *N*-ε-Maleimidocaproic acid (EMCA). The magnetic nanoparticle – oligonucleotide conjugates have been transfected into African green monkey kidney cells (CV-1) and Henrietta Lack human cervical cancer cells (HeLa). The surface of the spinel ferrites conjugated to oligonucleotides is functionalized with epichlorohydrin and EMCA or with aminopropyltriethoxysilane (APTES) in conjunction with mercaptopropionic acid (MPA) and EMCA. The versatility of the crosslinker group permits the attachment of oligonucleotides terminated with thiols or amine. Confocal micrographs show that both crosslinking methods formed conjugates that can be transfected into mammalian cells. Fluorescent images of synchronized responses of cells to magnetic field purport the

internalization in cells. Preliminary data indicating cellular uptake of magnetic nanoparticles, with a positively charged surface, without a “chaperone” is discussed.

6.1 Introduction

Magnetic nanoparticles have an evolving development in applications ranging from data storage to MRI contrast enhancement reagents to cell separation.[1] The focus of cellular delivery of therapeutic reagents for cancer treatment has led to many developments entailing the use of magnetic nanoparticles as carriers for purposes of delivery and cellular trafficking (see chapter 5). However, in most situations, the magnetic nanoparticles used are either magnetite or maghemite. Cobalt spinel ferrite nanoparticles are stronger magnetic nanoparticles and respond to lower magnetic field strength. This is a pertinent factor considering the ultimate goal is to be able to magnetic guide drug delivery and magnetically localize the treatment within a region. Hence, we have focused our attention on using $CoFe_2O_4$ and other spinel ferrites as magnetic carriers.

Previously, we have demonstrated that $CoFe_2O_4$ can be conjugated to oligonucelotides for cellular uptake and magnetic manipulation using a commercially available crosslinker, SPDP (*N*-succinimidyl 3-[2-pyrithiol]propionate).[2] Synchronized movements of cells in response to an external magnetic field as well as confocal and darkfield micrographs confirmed the incorporation of $CoFe_2O_4$ – oligonucleotides in cells and demonstrated the promising potential of $CoFe_2O_4$ as magnetic carriers for therapeutic reagents with magnetic control. Toxicity was not a focus in our previous study, but we

were able to demonstrate that $CoFe_2O_4$ did not induce any significant morphological change or interrupt the proliferation cycle. In this chapter, we explore different surface chemistry options for the attachment of oligonucleotides to $CoFe_2O_4$ and their applicability to different systems such as $MnFe_2O_4$. Specifically, we looked at a crosslinker that can form a thiol ester bond or an amide bond with oligonucleotides.

The possibility of using MFe_2O_4 (M = Co, Mn) nanoparticles as magnetic carriers for macromolecules has great potential and is illustrated in this chapter. Like most delivery systems, there is room for improvement. Current delivery method is often afforded through chemical transfection reagents that are toxic to cells if exposed for a long period of time. A better method is to modify the surface charge (e.g. using 1-H-pyrazole-1-carboximide, "HPC") of magnetic nanoparticles eliminating the requirement of a "chaperone". Preliminary data supporting this proposed method will be discussed as well.

6.2. Experimental

6.2.1 Preparation of Spinel Ferrite – Oligonucleotide conjugates

Cobalt spinel ferrite, $CoFe_2O_4$, was synthesized using a normal micelle method.[3] Briefly, a stoichiometric amounts of $CoCl_2 \cdot 6H_2O$ and $FeCl_2 \cdot 4H_2O$ were dissolved and added to a 1.5mM SDS (sodium dodecyl sulfate) surfactant solution at 10°C. Methylamine was then added at 10 °C and the solution was then heated to a temperature range of 55-65 °C f or 2 – 3 hrs. Nanoparticles were isolated with centrifugation followed

by several washes with 20:80 ethanol: distilled water. The final product was dried in air at 110 °C. Manganese spinel ferrite nanoparticles, $MnFe_2O_4$, were synthesized using a reverse micelle method.[4] A stoichiometric amounts of $Mn(NO_3)_2$ and $Fe(NO_3)_2$ were dissolved in water then a 0.4 M NaDBS (sodium dodecylbenzenesulfonate) surfactant solution was added followed by an addition of a large volume of toluene. After 24 hrs of reaction time, NaOH solution was added dropewisely accompanied by vigorous stirring. Volume is then reduced by distillation and the concentrated suspension was washed with water and ethanol. The final product was heat treated at 350 °C for 12 hrs under He atmosphere.

Surface activation of $CoFe_2O_4$ and $MnFe_2O_4$ nanoparticles was accomplished by washing residual surfactants of the surface with concentrated NaOH. To attach thiol terminated oligonucleotides, $CoFe_2O_4$ and $MnFe_2O_4$ were reacted with epichlorohydrin followed by amination with NH_4OH (Figure 6.1) or reacted with 1% aminopropytriethoxysilane (APTES; first step of Figure 6.2) to generate an amino moiety on the surface. Magnetic nanoparticles were then subjected to several washes with MesBupH (carbonate buffer; pH 4.5) then resuspended in a 25mM EMCA (ε-maleimidocaproic acid)/EDC (1-[3-dimethylaminopropyl]-3-ethylcarbodiimide) in MesBupH. The suspension was sonicated for one hour then shaken overnight at room temperature. The functionalized magnetic nanoparticles were then magnetically separated and washed with PBS (phosphate buffered saline; pH 7.4) several times. Thiol terminated oligonucleotides (**1** = 5' HS – $(CH_2)_6$ – GTA AAA CGA CGG CCA GTG 3') were reduced with Cleland's reagent (immobilized dithiolthreitol) and added to the magnetic nanoparticle suspension followed by gentle shaking for several hours. Subsequently, a

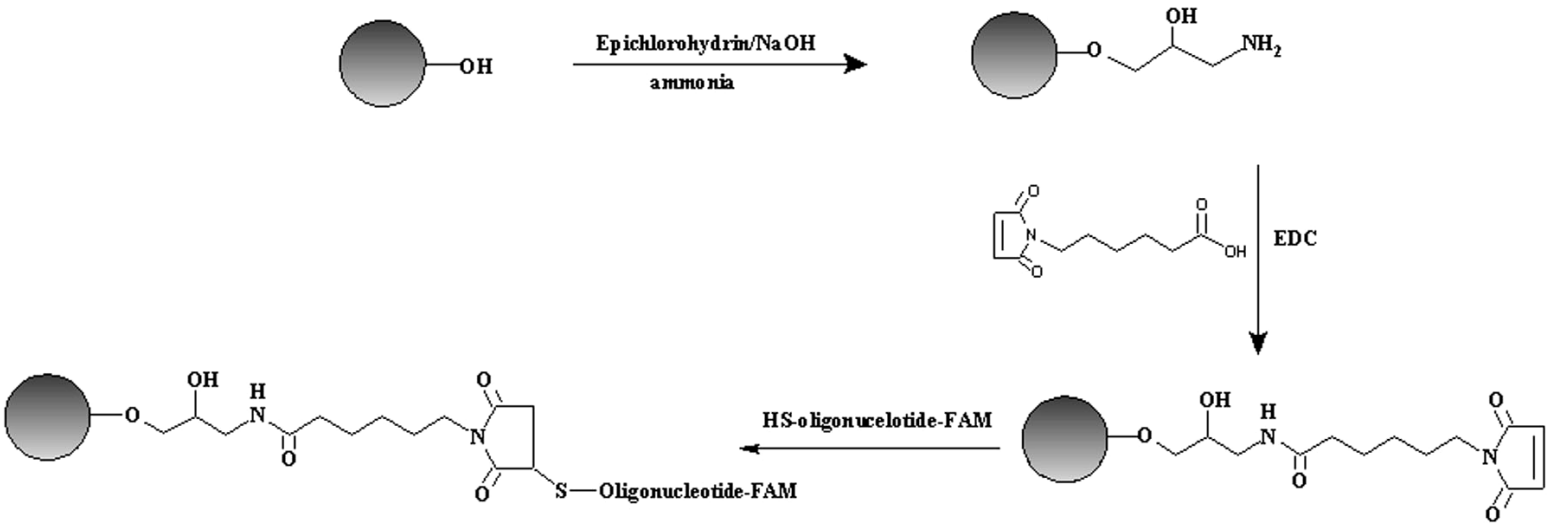

Figure 6.1 Surface modification of magnetic nanoparticles with epichlorohydrin – EMCA for attachment of thiol terminated oligonucleotides through a thiol ester bond formation. Alternatively, the first step can be accomplished with 1% APTES.

complimentary strand with a fluorescent tag (**2 =** CAC TGG CCG TCG TTT TAC 5') was added to the solution and incubated above the melting temperature ($T_m \geq 65°C$) for 30 minutes and then allowed to cool to room temperature. Prior to transfection, the final products were magnetically separated and washed with PBS or OptiMem (a reduced serum media).

Alternatively, the chemistry of EMCA can be reversed for the attachment of amino terminated oligonucleotides to the surface of magnetic nanoparticles (see Scheme 6.2). The residual surfactants on the surface are removed as described earlier. Magnetic nanoparticles ($CoFe_2O_4$ or $MnFe_2O_4$) were sonicated in a 1% APTES solution for 1 – 2hrs. After magnetic separation and several washes with PBS, a 25mM MPA (mercaptopropionic acid) / 50mM EDC was added and then incubated at 60°C for 4-6hrs with periodic shaking. The thiol functionalized magnetic nanoparticles are then magnetically separated and washed several times with PBS. A 25mM EMCA/PBS solution is then added and allowed to react overnight. Once the crosslinker, EMCA, is attached to the magnetic nanoparticles, the suspension was subjected to several magnetic separations and washes with PBS before an amino terminated oligonucleotide **3** (**3** = 5' $H_2N – (CH_2)_6 –$ GTA AAA CGA CGG CCA GTG 3') was introduced. Complimentary strands with a fluorescent tag were added to the suspension and allowed to hybridize above its T_m ($T_m \geq 65°C$) for 30 minutes and then cooled to room temperature. Hybridization with oligo **2** (**2 =** CAC TGG CCG TCG TTT TAC 5') with described conditions yielded MFe_2O_4 – **3-2**-FAM conjugates (M = Co or Mn). Conjugates were then magnetically separated and washed several times with PBS or OptiMem before transfection.

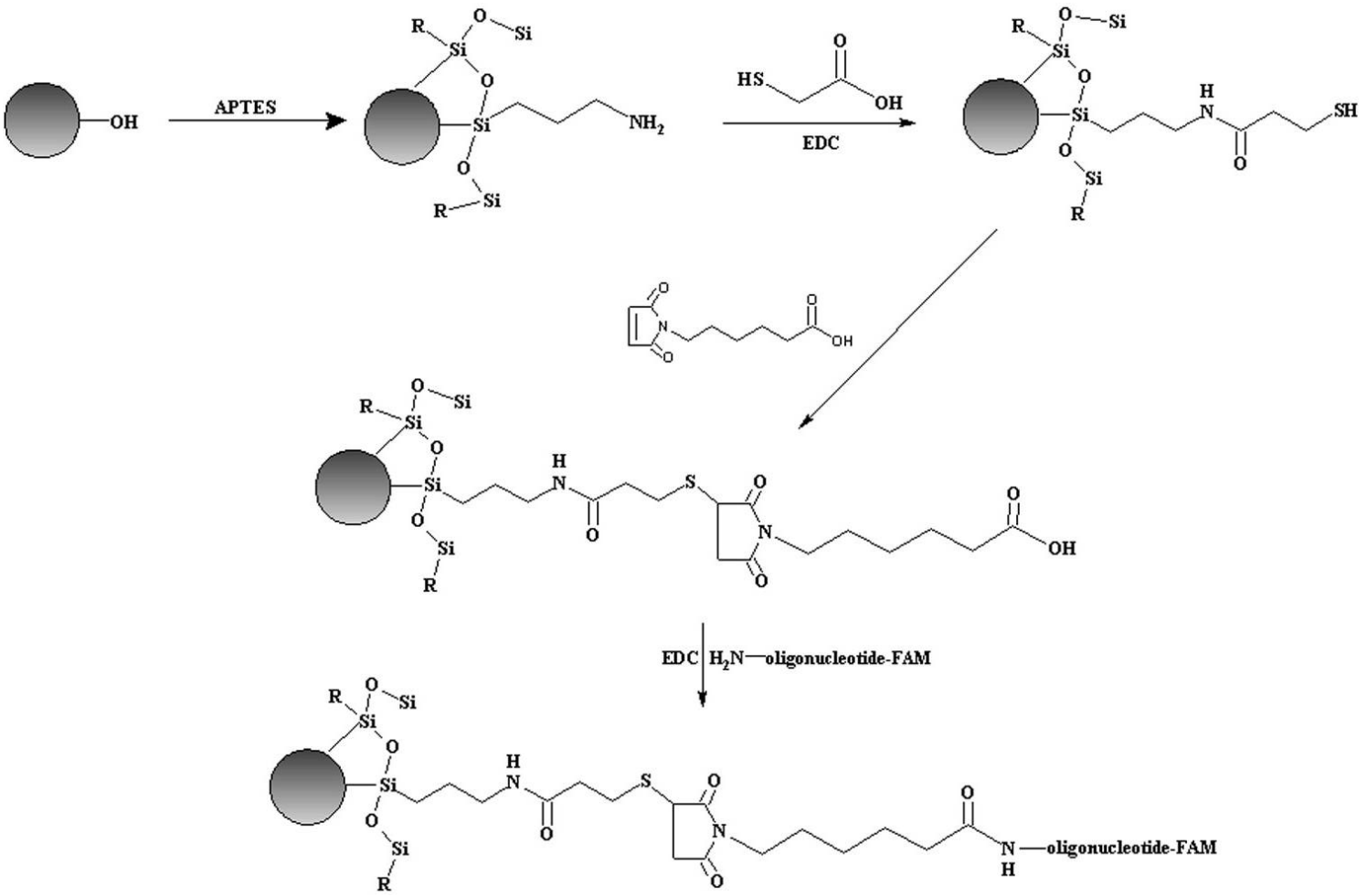

Figure 6.2 Surface functionalization of magnetic nanoparticle with APTES – MPA – EMCA for attachment of amine terminated oligonucleotides.

6.2.2. Preparation of $CoFe_2O_4$ – HPC conjugates

Using the same schematic for amino attachment, HPA was conjugated to $CoFe_2O_4$ (figure 6.3). Residual surfactant was removed with NaOH and $CoFe_2O_4$ was functionalized with APTES followed by MPA. Nanoparticles were then magnetically separated, rinsed with MesBupH, resuspended in 25mM HPC / 50mM EDC and then allowed to react overnight. The final product was then rinsed with distilled water and resuspended in distilled water for zeta potential measurements or resuspended in OptiMem for cellular delivery experiments.

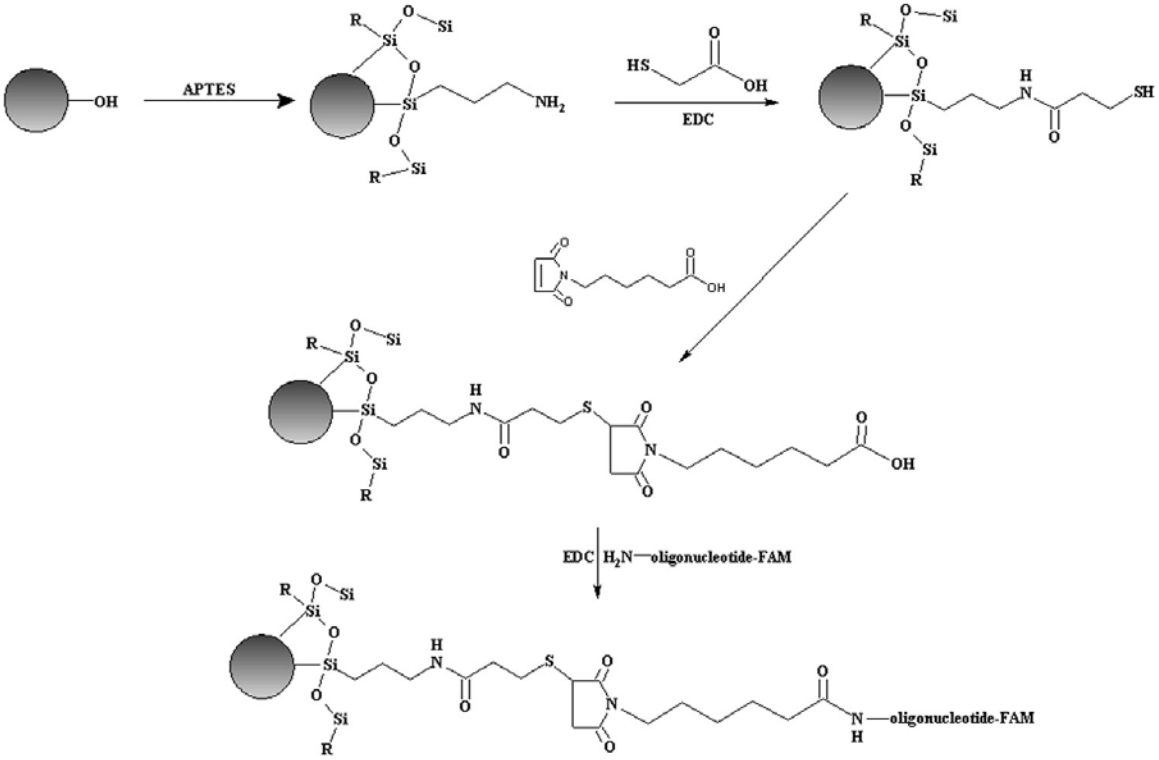

Figure 6.3 Surface modification of $CoFe_2O_4$ for the attachment of HPC.

6.2.3. Transfection

Henrietta Lack's cervical cells (HeLa) and African green monkey kidney cells (CV-1) were grown on coverslips in a 6-well plate in Dubelcco's Modified Eagle's Medium (DMEM) supplemented with 10% CBS (calf bovine serum) and 1% penicillin streptomycin glutamate to 60-70% confluency. Media was then removed and cells were washed with OptiMem. Lipofectamine™ was allowed to complex with MFe_2O_4 – oligonucleotide (M = Co, Mn) then incubated with cells in OptiMem for 7-8 hours at 37°C and 5% CO_2. Transfection media was then removed through aspiration and replaced with a growth media and incubated for an additional day.

6.2.4 Cellular Delivery of positively charged $CoFe_2O_4$ into CV-1 cells

African green monkey cells, CV-1, were grown on coverslips in a 6-well plate in DMEM supplemented with 10% CBS and 1% penicillin streptomycin glutamate to 60-70% confluency. Media was removed prior to cellular delivery and cells were rinsed with OptiMem. Cobalt spinel ferrite – HPC complexes in OptiMem (estimated 125 μg/well of $CoFe_2O_4$ – HPC complex) were added to cells and incubated for eight hours at 37°C and 5% CO_2. OptiMem was then removed from the wells and replaced with a growth media (DMEM, 10% CBS, 1% penicllin streptomycin glutamate) then further incubated for 24 hours.

6.2.5. Characterization

Post transfection, transfected cells to be examined by confocal microscopy are rinsed with PBS and fixed onto coverslips through standard fixation protocols using 4% *p*-formaldehyde in PBS for 15 minutes. Cells are then rinsed with PBS and mounted onto glass microscope slides with paramount G (preserves fluorescence). The confocal microscope used in these experiments is a Zeiss LSM 500 housed with an Argon laser. For monitoring the response of $CoFe_2O_4$ – HPC to an external magnetic field, cells are first rinsed with PBS, trypsinized, then resuspended in PBS.

6.3. Results and Discussion

6.3.1 Crosslinking of MFe_2O_4 (M = Co, Mn) to oligonucleotides

Using a heterofunctional crosslinker, EMCA, oligonucleotides terminated with a thiol group or an amino group has been conjugated to MFe_2O_4. Surface functionalization with epichlorohyrin or APTES provided the amino moiety necessary for attachment of EMCA. To generate a thiol reactive surface, EMCA was added to amine functionalized MFe_2O_4 in the presence of EDC. To make the carboxylate terminus available for reaction, amino functionalized MFe_2O_4 nanoparticles were then further modified with MPA yielding a free sulfhydryl group. Subsequently, it was reacted with EMCA to form a thiol ester bond. An alternative method to leave the carboxylate terminus of EMCA is shown in Figure 6.4. We found that more attachment occurred following Figure 6.2 than Figure

6.4. This was evident due to the lack of fluorescence present when we used the protocol in Figure 6.4 was used. The lack of attachment is proposed to be attributed to the lack of MPA molecules initially attached to the surface of MFe_2O_4 nanoparticles.

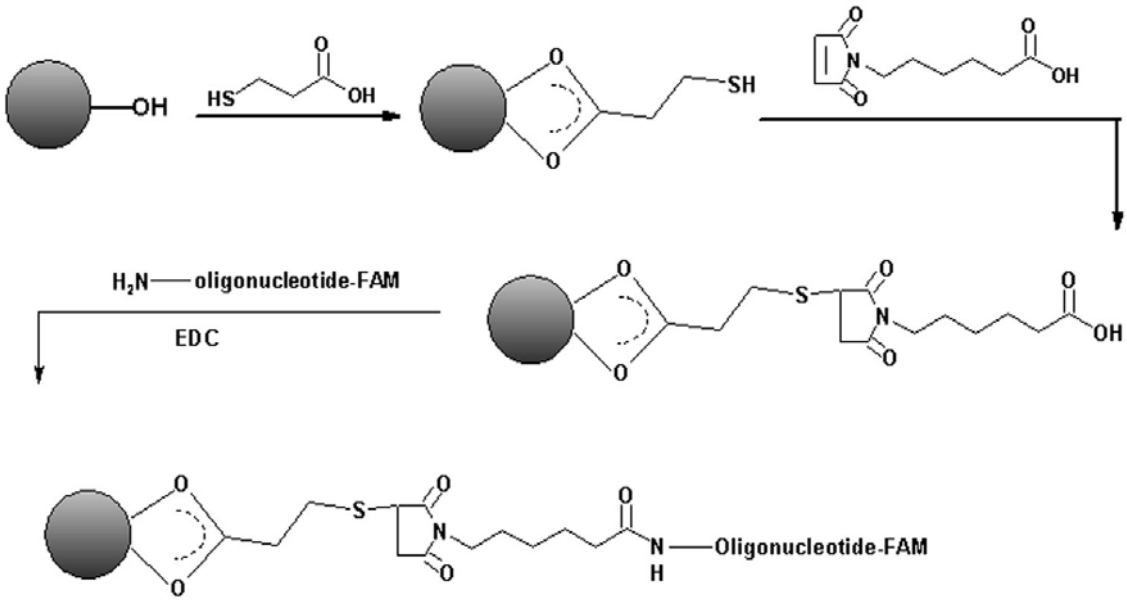

Figure 6.4 Functionalization of magnetic nanoparticles ($CoFe_2O_4$ or $MnFe_2O_4$) with a heterocrosslinker for amide bond attachment to oligonucleotides

6.3.2 Transfection of MFe_2O_4 – oligonucleotide conjugates (M = Co, Mn) into cells

The incorporation of MFe_2O_4 – oligonucleotide conjugates into CV-1 and HeLa cells were primarily monitored by the fluorescent luminescence present in confocal z-sectional images. Using two different crosslinking schematics and two different spinel ferrites, the versatility of spinel ferrite magnetic nanoparticles as carriers for therapeutic reagents has been illustrated. As can be seen in figure 6.5-6.9, there is a general trend indicating lack of fluorescent luminescence at the bottom and top of the cell and a pronounced luminescence in the mid sections of the cells. This is a lucid indication that MFe_2O_4 – oligonucleotide conjugates are internalized by the cells and is supported by our previous study. These results are very similar to those shown in chapter 5 and is further purported by the synchronized movements of the cells in response to an external magnetic field (see Figure 10; heintz_eva_l_200412_phd_magneticmovement2.mpg). The ability to magnetically manipulate the magnetic nanoparticles in cells revealed the possibility of magnetically guided transport as well as localization of magnetic nanoparticles and their conjugates.

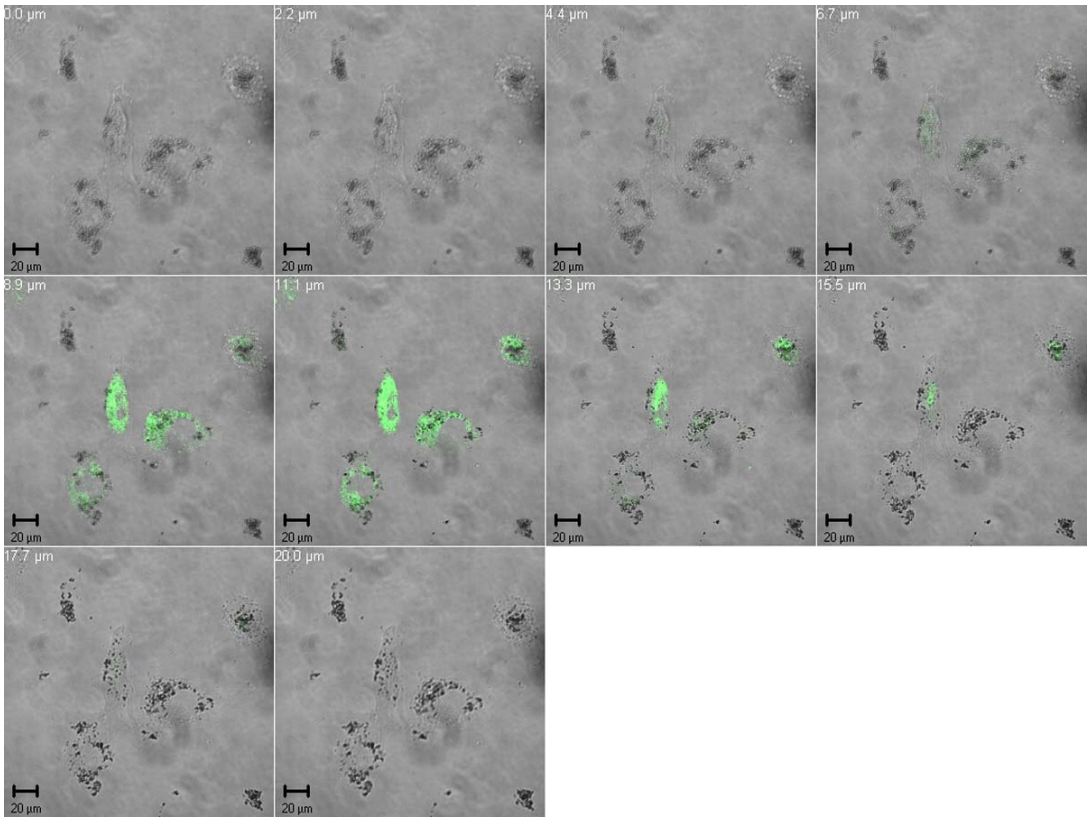

Figure 6.5 Confocal overlay z-stack images of CV-1 cells transfected with $CoFe_2O_4$-EMCA-SH-oligonucleotide.

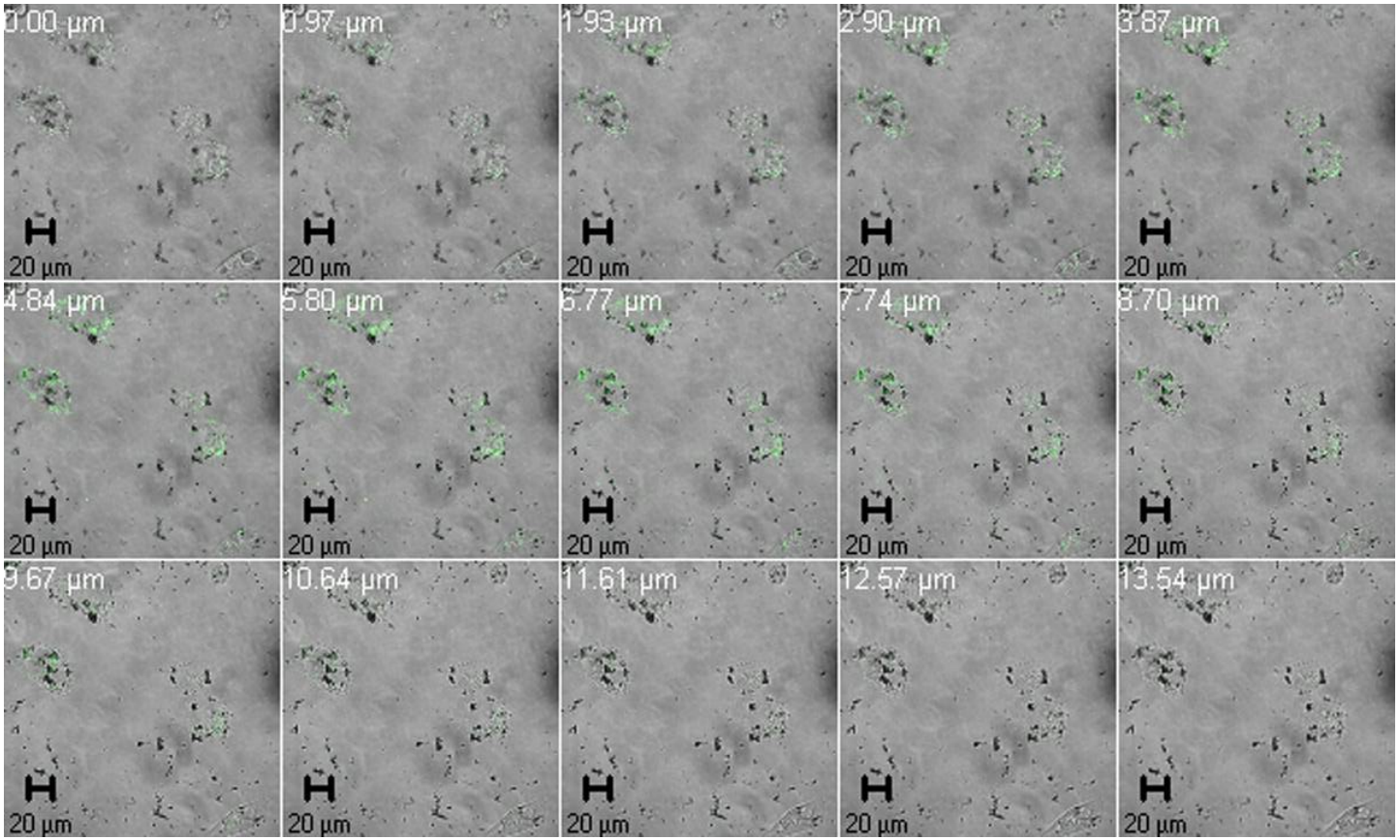

Figure 6.6 Confocal overlay z-stack images of HeLa cells transfected with $CoFe_2O_4$-EMCA-SH-oligonucleotide.

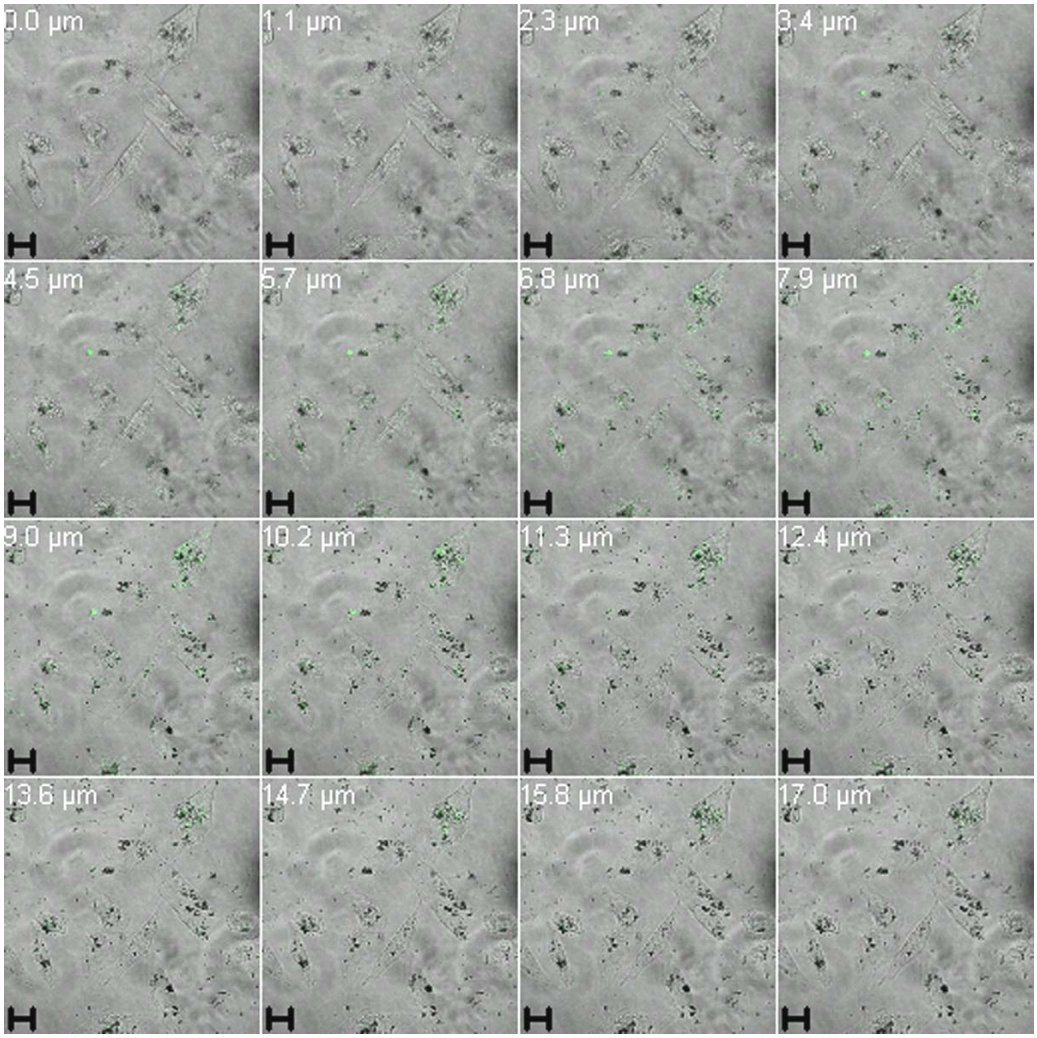

Figure 6.7 Confocal overlay z-stack images of HeLa cells transfected with $MnFe_2O_4$-EMCA-SH-oligonucleotide.

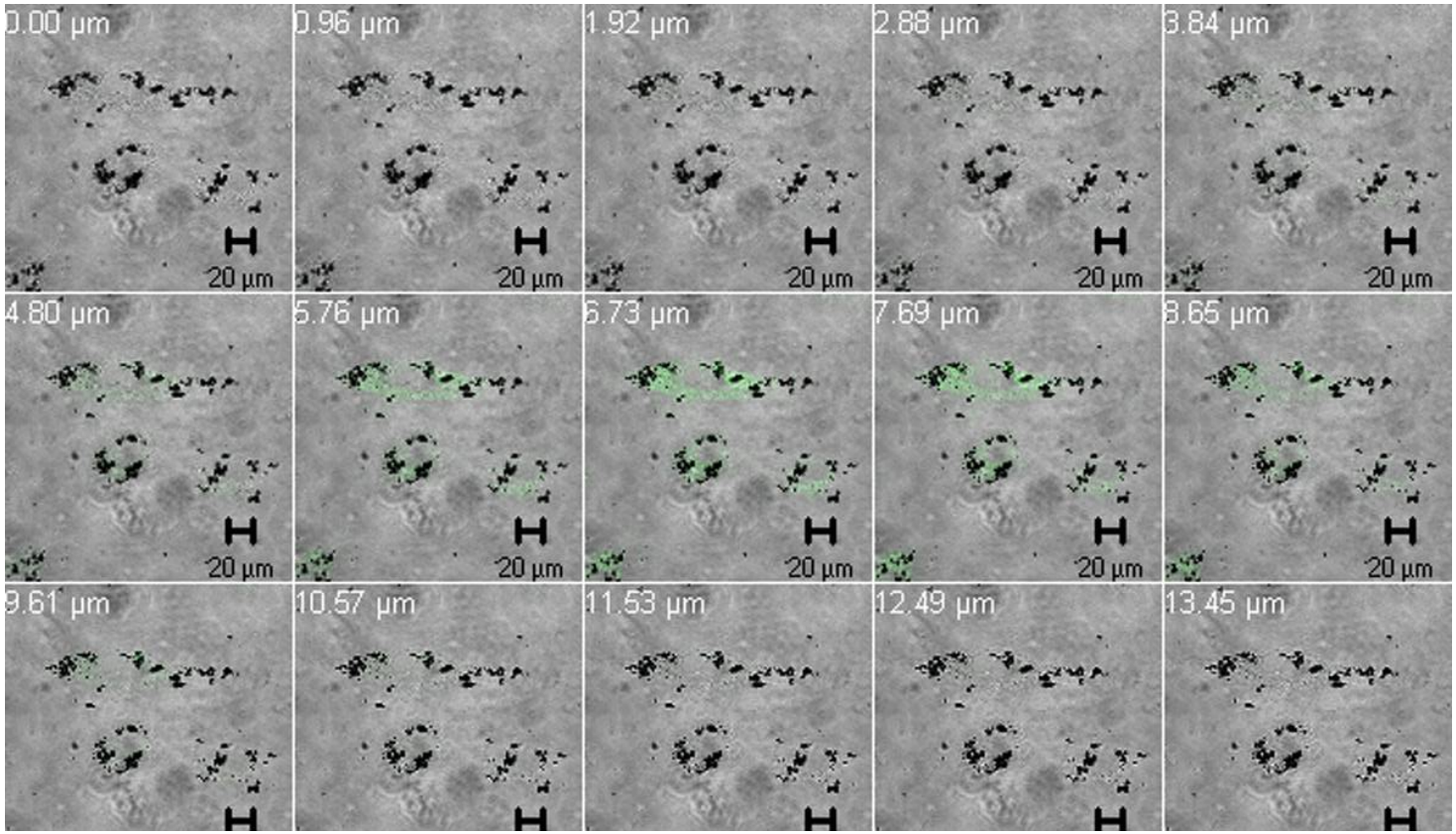

Figure 6.8 Confocal overlay z-stack images of CV-1 cells transfected with $CoFe_2O_4$-EMCA-NH-oligonucleotide.

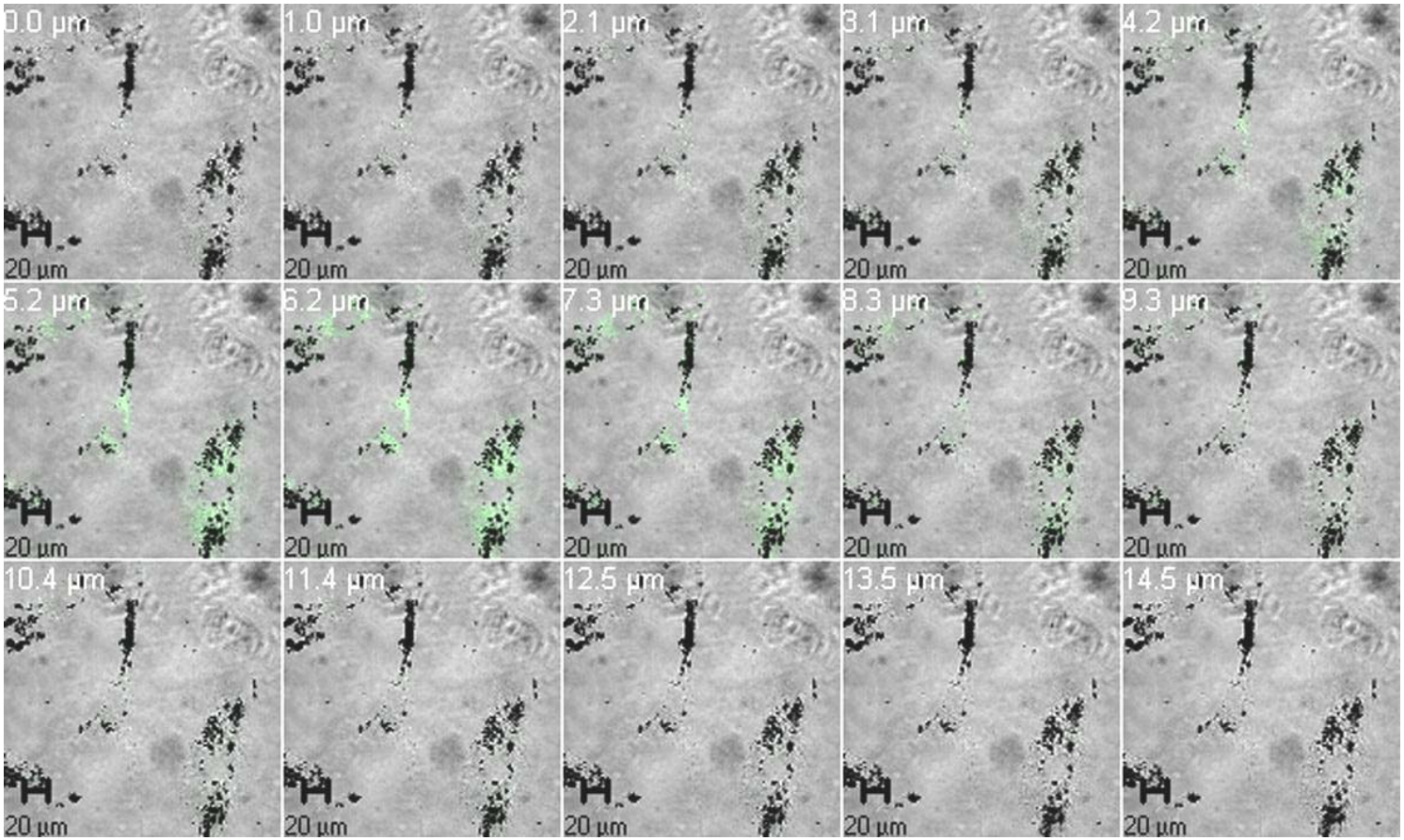

Figure 6.9 Confocal overlay z-stack images of HeLa cells transfected with $CoFe_2O_4$-EMCA-NH-oligonucleotideoligonucleotide

Figure 6.10 Movie of synchronized movements of the cells in response to an external magnetic field (heintz_eva_l_200412_phd_magneticmovement2.mpg Click tag ).

6.3.3 Surface charge modification with HPC and cellular delivery of $CoFe_2O_4$ – HPC

Many transfection or cell delivery facilitating reagents are toxic to cells after prolong exposure. From our control experiments in chapter 5, the transfection reagent did not complex with magnetic nanoparticles when oligonucleotides were not present on the surface of the particles. Hence, we explored the possibility of introducing magnetic nanoparticles without a "chaperone" by chemically altering the surface charge of the magnetic nanoparticles, $CoFe_2O_4$. Following the crosslinking schematics in Figure 6.3 we attached HPC to the surface of magnetic nanoparticles. At neutral pH, HPC has a net positive charge.[5,6] Hence, $CoFe_2O_4$ – HPC complexes is presumably positively charged. Preliminary zeta potential measurements supported our hypothesis showing that native $CoFe_2O_4$ have a net negative surface charge (~ -3 mV) but when modified with HPA, there is a net positive surface charge (~ +4 mV). We were unable to use fluorescent microscopy or confocal microscopy to trace the location of CoFe2O4 – HPC intracellularly due to the lack of a fluorescence tag. Using an external magnet, we attempted to visualize the movement of CV – 1 cells with $CoFe_2O_4$ – HPC in response to external magnetic fields with bright field microscopy. From the micrographs in Figure 6.10, the synchronized movement of cells, with incorporated $CoFe_2O_4$ – HPC, to an

external magnetic field confirms the uptake of $CoFe_2O_4$ – HPC. The mechanism of internalization is unclear at the moment. In cells, transport is either active or passive. Usually, positively charged species are transported through passive diffusion. Hence, we propose that $CoFe_2O_4$ – HPC, being positively charged, is taken up by cells through diffusion.

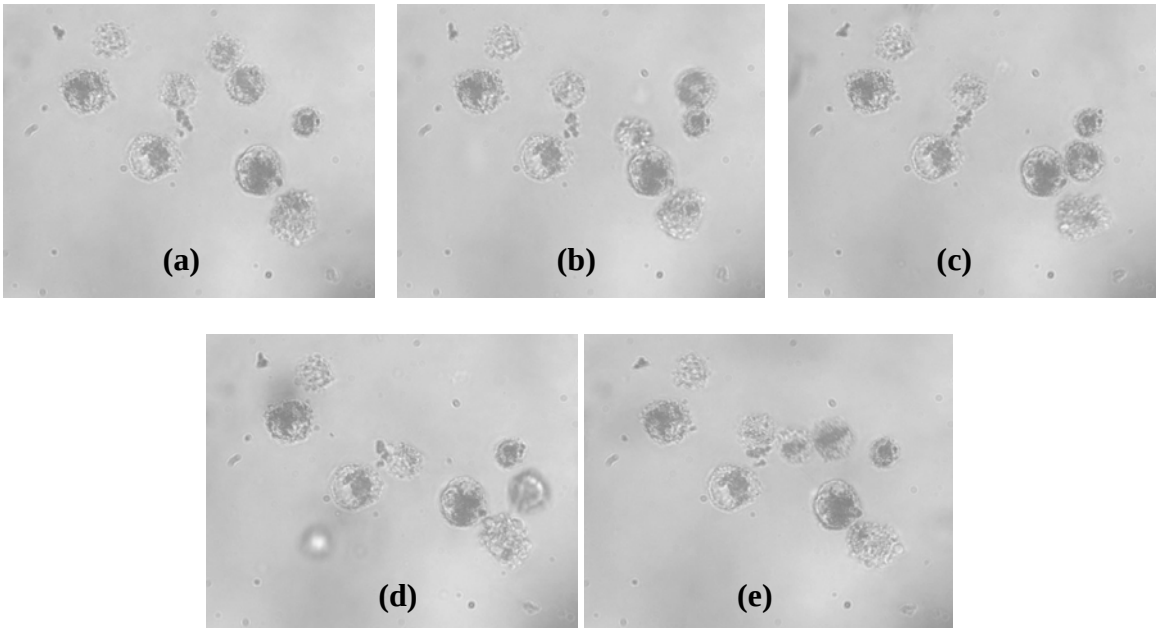

Figure 6.11 Brightfield micrographs of CV-1 cells with $CoFe_2O_4$ – HPC moving with an external magnetic field.

6.4 Conclusion

Cobalt and Manganese spinel ferrites conjugated to oligonucleotides have been successfully transfected into CV-1 and HeLa cells. Two different points of attachment utilizing one common crosslinker were explored. Comparable results were found with both attachment schematics. Cells movement corresponding to an external magnetic field revealed the possibility of magnetic guidance and localization. Surface modification of magnetic nanoparticles with HPC provided an alternate method to deliver magnetic nanoparticles into cells without facilitating reagents. This study demonstrated the various possibilities of tailoring the surface of magnetic nanoparticles for subsequent cellular delivery and explored spinel systems other than $CoFe_2O_4$. All experiments studied here were done *in vitro* and it would be interesting to resolve the parameters involved for *in vivo* experiments. Progress towards this direction will not only involve toxicity but also involve the magnetic control once magnetic nanoparticles enter the circulatory system.

6.5 References

(1) Niemeyer, C. M. *Angew. Chem. Int. Ed.* **2001**, *40*, 4128.

(2) Heintz, E. L.-H.; Rohatgi, P.; Doyle, D. F.; Fahrni, C.; Zhang, Z. J. *Submitted* **2004**.

(3) Rhondinone, A. J.; Samia, A. C. S.; Zhang, Z. J. *J. Phys. Chem. B.* **2000**, *103*, 6876.

(4) Liu, C.; Zou, B.; Rhondinone, A. J.; Zhang, Z. J. *J. Phys. Chem. B.* **2000**, *104*, 1141.

(5) Mathew, C. K.; Van Holde, K. E. *Biochemistry 2nd Ed.*; Benjamim/Cummings Publishing Company, Inc.: Menlo Park, 1996.

(6) Wender, P. A.; Rothbard, J. B.; Jessop, T. C.; Krider, E. L.; Wylie, B. L. *J. Am. Chem. Soc.* **2002**, *124*, 13382.

CHAPTER VII

CONCLUSIONS AND FUTURE WORK

7.1 Tunability of magnetic nanoparticles

In this thesis, the synthesis and characterization of samarium doped cobalt spinel ferrites was discussed. Data showed that by introducing small amounts of samarium the magnetic properties of the doped spinel ferrite dramatically differs from the native $CoFe_2O_4$. The similarity between the X-ray diffraction pattern of $CoFe_2O_4$ and the samarium doped cobalt spinel ferrite, $CoSm_xFe_{2-x}$, revealed that doping of Sm^{3+} did not change the lattice constant and retained the spinel phase. Although neutron studies were not conducted due to the large absorption cross sections of Sm^{3+} ions, data from, previous studies using La^{3+} was used demonstrate that Sm^{3+} is homogenously doped into the octahedral site of a spinel ferrite unit cell. The high coercive forces of Sm^{3+} ions comes from the large magnetocrystalline anisotropy (due to the high spin-orbit coupling). Hence, when doped into cobalt spinel ferrites, an increase in coercitivity was observed. When comparing between samples with different Sm^{3+} concentrations, a negligible change in

coercitivity and saturation magnetization was observed and is postulated to be attributed to the small change in Sm^{3+} concentration. Relative to each other, the addition of the coercive force to the spinel system is not as pronounced when comparing doped samples. By keeping the composition constant and varying the size, magnetic properties were also altered. Of particular interest is in the non-linear trend of coercitivity change. There was an initial increase in coercitivity with increase in size then coercitivity began to decrease with increasing size. While we propose that the initial increase in coercitivity is from coherent rotation of moments, the eventual decrease in coercitivity is unclear. We can only speculate that it is due to other surface effects.

We have demonstrated through this systematic study that it is possible to dope relatively large lanthanide ions into spinel ferrite system. Because of the dramatic change in magnetic properties between the native $CoFe_2O_4$ and the Sm^{3+} doped spinel ferrites, , $CoSm_xFe_{2-x}$, the tunability of magnetic nanoparticles have been demonstrated. There are many data that we cannot conclusively interpret at this time. By studying the effects of doping other lanthanide ions in a systematic manner, a comparison can be made between each dopant and a more conclusive interpretation can be presented.

7.2 Cellular Uptake of Magnetic Nanoparticles

In chapter 5 and 6, different approaches to modify the surface of $MFeO_4$ (M = Co, Fe) for cellular uptake was illustrated. Using commercially available heterofunctional crosslikners like SPDP and EMCA, thiol terminated or amine terminated oligonucleotides were attached to $MFeO_4$ nanoparticles. Using transfection reagents such

as Lipofectamine™, $MFeO_4$ – oligonucleotide conjugates were taken up by cells through endocytosis. Darkfield microscopy data in conjuction with confocal microscopy confirmed that $MFeO_4$ – oligonucleotide conjugates were indeed incorporated into the cell. Synchronized movement of transfected cells in response to a magnetic field further supported the internalization of $MFeO_4$ – oligonucleotide conjugates and demostrated magnetic control of $MFeO_4$ nanoparticles in cells. From force calculations (Appendix B), there is a large discrepancy between the magnetic force experienced by cells and the hemadynamic force experienced by a cell. Based on calculated force values, it would be very difficult to guide MFe_2O_4 nanoparticles in a flowing system. However, previous experimental data showed that it is possible to stop MFe_2O_4 in a flowing system with about 300G. Clearly, there are many factors that were not considered in the force estimation calculations. Future work such as monitoring the magnetic response of cells transfected with magnetic nanoparticles in a flowing system as well as detail mathematic modeling of all the hemadynamic parameters involved may help identify if magnetic control *in vivo* is truly possible.

When the surface charge of $CoFe_2O_4$ nanoparticles were modified with HPC, surface charge was altered. Internalization of $CoFe_2O_4$ – HPC was demonstrated by the movements of cells in response to an external magnetic field. Although the mechanism from which $CoFe_2O_4$ – HPC is unclear at the moment, it is proposed to be through passive diffusion. Surface density of HPC on $CoFe_2O_4$ was not examined but may play an important role in the uptake efficiency by cells. By examining the surface coverage of HPC and the uniformity of the attachment of HPC, better understanding of how to improve the cellular uptake of magnetic nanoparticles can be afforded.

7.3 Magnetic Nanoparticles Coupled to Viruses

We made an attempt to conjugate $CoFe_2O_4$ to Cowpea Mosaic Virus (CPMV) through surface modification of $CoFe_2O_4$ with EMCA (see Appendix B). A preliminary reconstructed three dimensional TEM image of the native CPMV capsid was compared to the, presumably, $CoFe_2O_4$ bound CPMV capsid. There was a clear difference between the two images. We speculated that the attachment was successful but more data is required to confirm the attachment. CPMV is capable of expressing foreign epitopes. Conjugating CPMV to magnetic nanoparticles for magnetically guided delivery into the circulatory system is worth pusuing to see if an immunoresponse would be prompted. Cowpea mosaic viruses are only infectious towards plants, hence, they are great DNA carriers. With the advancement of gene therapy, there is a lot of advantage of coupling magnetic nanoparticles to CPMV. For example, an active gene can be carried in the capsid of CPMV that is attached to magnetic nanoparticles. Using a magnetic field, may possible to guide the CPMV-magnetic nanoparticle conjugate close to the target site to unload the active gene. As mentioned, the data collected thus far is preliminary and this system will need a lot more progress before proposed applications are explored.

7.4 Conclusion

In conclusion, the tunability of cobalt spinel ferrites were explored as was their applications in cell biology. From synthesis to characterization to application, data

showed the versatility of magnetic nanoparticles. We are far from pursuing *in vivo* experiments but data collected throughout this thesis facilitates the progress towards *in vivo* testing.

APPENDIX A

MAGNETIC FORCE AND HEMADYNAMIC FORCE ESTIMATION

A.1 Magnetic Gradient Determination

The magnetic field of the Nd-Fe-B magnet used in Chapter 5 and 6 was measured at various distances from the probe to the magnet using a Lakeshore 410 Gaussmeter (see table A.1). The magnetic field is proportional to the distance by

$$H \propto 1/r^3 \tag{A.1}$$

where H is the magnetic field and r is the distance in meters. [1,2] Based on our experimental measurements, the data correlates well with the distance relationship (see figure A.1). Using the equation

$$y = 0.0111/ x^{2.8443} \tag{A.2}$$

at 5.08cm (distance used experimentally between cell sample and magnet), the magnetic field is estimated to be 53.2 G, comparable to those reported in literature.[3] Choosing the magnetic field value at the source (3315G) and at 5.08 cm (53.2G), the magnetic gradient is estimated to be 6.42 T/m.

Table A.1 Magnetic Flux change with distance

Approximate Distance From Magnet (m)	**Magnetic Field Measured (G)**
1.0×10^{-2}	2680
2.0×10^{-2}	846
3.0×10^{-2}	387
4.0×10^{-2}	180
5.0×10^{-2}	69.9
6.0×10^{-2}	21.1
7.0×10^{-2}	12.6
8.0×10^{-2}	9.20
9.0×10^{-2}	14.7
1.0×10^{-1}	5.50
1.2×10^{-1}	3.60
2.0×10^{-1}	1.00

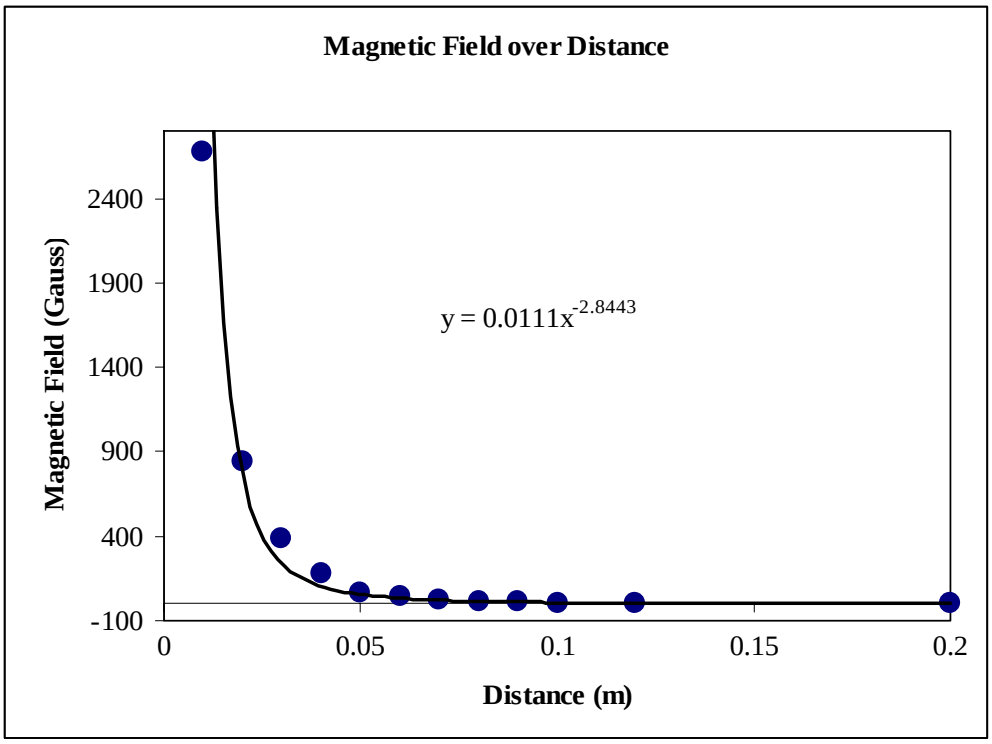

Figure A.1 Graph of Magnetic field of a small Nd-Fe-B magnet with distance.

A. 2 Magnetic Force Experienced By Cells

The amount of magnetic force exerted on one cell by a magnet can be estimated by multiplying the magnetic moment of the particles in one cell by the magnetic gradient.[1,4] Given that the diameter of the magnetic nanoparticles is 10.02 nm, the volume can be calculated by

$$V_{np} = 4/3\pi r^3 \qquad \text{(A.3)}$$

where V_{np} is the volume of each nanoparticle and r is the radius of the nanoparticle. By multiplying the V_{np} by the number particles per cell (4.44×10^{7} particles/cell), we get a total volume of 2.34×10^{-17} cm^3. The density of $CoFe_2O_4$ has been estimated to be 5.29 g/cm^3, hence there are approximately 1.24×10^{-16} g of $CoFe_2O_4$ in each cell. With a M_s of 76.7604 emu/g (determined experimentally), we can estimate the total moment present in each cell by

$$M_s \times g \text{ nanoparticles in each cell} \qquad (A.4)$$

giving us 9.52×10^{-15} emu (9.52×10^{-18} $A \cdot m^2$). Using the magnetic gradient of 6.42 T/m, the magnetic force exerted experienced per cell is 61.1×10^{-17} N.

A.3 Hemadynamic Force Experienced By Cells

Hemadynamic forces are forces required to circulate blood through the circulatory system.[5,6] It counteracts the magnetic forces on particles as they flow through the bloodstream. When the particle size, is less than 100 μm the Reynolds number (Re) is given as

$$Re = \rho v d / \mu \qquad (A.5)$$

where ρ is the density of the medium (blood), v is the velocity of flow, and μ is the viscosity of the medium.[7] If Re is relatively small, then the primary forces experienced by particles (cells) are primarily inertial forces.[6] Since viscous force is governed by Stoke's Law at small Re values, we estimate the hemadynamic force by

$$F = 6\pi\eta vr \qquad \text{(A.6)}$$

where η is the viscosity of blood (4.0×10^{-3} kg/m·s)[5], v is the velocity of blood (~ 4.7×10^{-4} m/s capillary flow)[5], and r is the radius of the cell (40μm). From equation A.6, we calculated that the hemadynamic force experienced by one cell in a capillary flow would be 1.42 nN.

A.4 Conclusion

Experimentally, we found when the distance between the magnet and the cell suspension is about 10-15 cm away, the magnetic movement halted. The most dramatic movement of cells occurs when the distance between the magnet and the cell suspension is less than 5.08cm. Using a magnetic gradient of 6.42 T/m, the magnetic force experience per cell is estimated to be 61.1 $x10^{-17}$ N. The hemadynamic force counteracting the magnetic force on a cell (with magnetic nanoparticle incorporated) in a flowing system such as a capillary was estimated to be 1.42 nN.

With such a large discrepancy between the hemadynamic force and the magnetic force, magnetic localization of cells (with internalized magnetic nanoparticles) flowing in

a capillary is not likely to occur. However, we have previously shown that magnetic nanoparticles (25nm) conjugated to proteins flowing in a carrier fluid with a 5cps viscosity at 20cm/s in a capillary can be captured with an external magnet.[8] Clearly, the system is much more complicated then what is presented here. To truly understand the complicated factors involved, models and calculations encompassing factors such as pressure, turbulence of flow, attractive forces, change in viscosity, and many other variants has to be considered. If we completely rely on the calculations presented here then we can postulate that an increase in size of the nanoparticle and an increase in magnetic field applied (e.g. 1.0 T) with a magnet at closer proximity (less than 1 cm) may provide enough magnetic force to localize the cells flowing in a capillary.

A.5 References

(1) Chikazumi, S. *Physics of Ferromagnetism 2nd Ed.*; Claredon Press: Oxford, 1997.

(2) Serway, R. A. *Physics for Scientists and Engineers with Modern Physics 4th Ed.*; Saunders College Publishing: San Francisco, 1996.

(3) Lubbe, A., S.; Alexiou, C.; Bergemann, C. *J. Surg. Res.* **2001**, *95*, 200.

(4) Leach, J. In *Electrical Engineering*; Virginia Polytechnic Institute and State University: Blacksburg, 2003, p 83.

(5) Lodish, H.; Baltimore, D.; Berk, A.; Zipursky, S. L.; Matsudaira, P.; Darnell, J. *Molecular Cell Biology 3rd Ed.*; W. H. Freeman and Company: New York, 1995.

(6) Hademenos, G. J.; Massoud, T. F. *Stroke* **1997**, *28*, 2067.

(7) http://www.cvphysiology.com/Hemodynamics/H007.htm.

(8) Rondinone, A. J. In *Chemistry and Biochemistry*; Georgia Institute of Technology: Atlanta, 2001, p 180.

APPENDIX B

COWPEA MOSAIC VIRUS COUPLED COBALT SPINEL FERRITES

ABSTRACT

An attempt to couple cobalt ferrite magnetic nanoparticles to Cowpea mosaic virus (CPMV),a plant virus, capable of expressing foreign antigenic epitopes, has been made. Cobalt spinel ferrite nanoparticles modified with ε-maleimido caproic acid are used to probe for free sulfhydryl groups present at the interior of the CPMV capsid. Preliminary data of three dimensionally reconstructed cryo-transmission electron micrographs showed that the nanoparticles are likely to be bound to the pores of the viral capsid. The versatility of the virus with the addition of magnetic properties from the magnetic nanoparticles may lead to many potential biological applications including guided and localized gene transfer, biosensors, and self-assembly models.

B.1 Introduction

The application spectrum of nanoparticles extends across several fields of science and will continue to expand with time. Focusing on magnetic nanoparticles, application such in data storage,[1-4] ferrofluids,[5-8] magnetic resonance imaging[9-12], cell separation[13,14], and cellular trafficking[15-19] have all been demonstrated. Recently, the induced self-assembly of magnetic nanoparticles through viruses has also been addressed as a means of detecting viral particles through magnetic resonance imaging.[20,21] Although there are numerous publications on virus identification, viral applications, and viral genome manipulation, few are focused on the applications of virus coupled to magnetic nanoparticles. Our study here focuses on expanding the bio-applications of magnetic nanoparticles by coupling cowpea mosaic virus to cobalt spinel ferrite to investigate on potential uses.

Cowpea mosaic virus, a plant virus in the *Como* genera of the Comoviridae share similar structural organization, DNA and RNA sequence, and replication processes to mammalian picornaviruses such as poliovirus.[22] The primary host of CPMV is *Vigna unguiculata* and when infected with, CPMV can cause vein yellowing, mosaic formation, and deformation of leaves.[23,24] Recently, the crystal structure of CPMV was resolved at 2.8Å resolution by Lin and co-workers.[25] The capsid contains 60 copies of a large protein and 60 copies of a small coat protein that assembles into an icosahedral symmetry. Cowpea mosaic virus can express foreign epitopes when its wild type sequence of CPMV is removed and replaced with epitopes of foreign viruses such as the human rhinovirus type 14 (HRV-14) or the human immunodeficiency virus type 1 (HIV-1) [26] The structural

symmetry of CPMV, the stability of CPMV at a broad pH range of 3-9 at room temperature, the ease of producing large quantities of CPMV, and the ability of CPMV to express foreign epitopes without infecting mammalian hosts with its own infectivity makes it an attractive system to study as gene carriers and self assembly models.

Recently, the versatility of CPMV has been demonstrated through several variations of applications. Raja and co-workers attached polyethylene glycol onto the surface of CPMV to monitor changes in primary immunogenic responses.[27] Smith et. al. have immobilized CPMV onto gold substrates through dip-pen nanolithography (DPN) chemospecifically minimizing adsorption of nonspecific proteins that may serve as a ligand-receptor model and may have potential uses as biosensors.[28] In a separate study, Raja and co-workers have also demonstrated that carbohydrates can be decorated on the capsid of CPMV.[29] The potential of CPMV as a nanoscale building block was addressed as gold nanoparticles were attached to mutant CPMVs forming a nice assembly.[30,31] In this chapter, preliminary data on the coupling of magnetic nanoparticles to CPMV will be discussed. Additionally, future directions of this system will be proposed.

B.2 Experimental

Magnetic nanoparticles, $CoFe_2O_4$, between 3.7nm and 4.2nm were prepared using a normal micelle method.[32] Briefly, stoichiometric amounts of $CoCl_2 \cdot 6\ H_2O$ and $FeCl_2 \cdot 4\ H_2O$ were mixed together with 1.5mM sodium lauryl sulfate (SDS). After nucleation, the pH was increased with methylamine. The suspension is then heated to 65°C to allow

growth of the magnetic nanoparticles. Nanoparticles were isolated through centrifugation and dried at 110 °C in air. The size and phase of the sample is then verified with powder XRD before use.

Before attachment to the Cowpea Mosaic Virus, modification to the surface of $CoFe_2O_4$ was made (see Figure B.1). Residual surfactant was removed by stirring $CoFe_2O_4$ in concentrated NaOH. After several washes with distilled water followed by magnetic separation after each wash, the surface was then functionalized with epichlorohydrin in 5M NaOH at 60°C for two hours followed by amination with NH_4OH. The amine functionalized magnetic nanoparticles were then washed with DMSO several times followed by magnetic separation after each wash. A commercially available heterofunctional crosslinker, *N*-ε-Maleimidocaproic acid (EMCA), was attached to the surface of $CoFe_2O_4$ through amide bond formation in the presence of 1-(3-dimethylaminopropyl)-3-ethylcarbodiimide (EDC). Maeimide functionalized magnetic nanoparticles(~210 μg) were reacted with thiol groups in the CPMV capsid (~100μg) in PBS or 20% DMSO/PBS with a reducing agent, dithiothreitol (DTT). The resulting $CoFe_2O_4$ – CPMV is then characterized with cryo-TEM and a three-dimensional image is reconstructed through complex modeling.

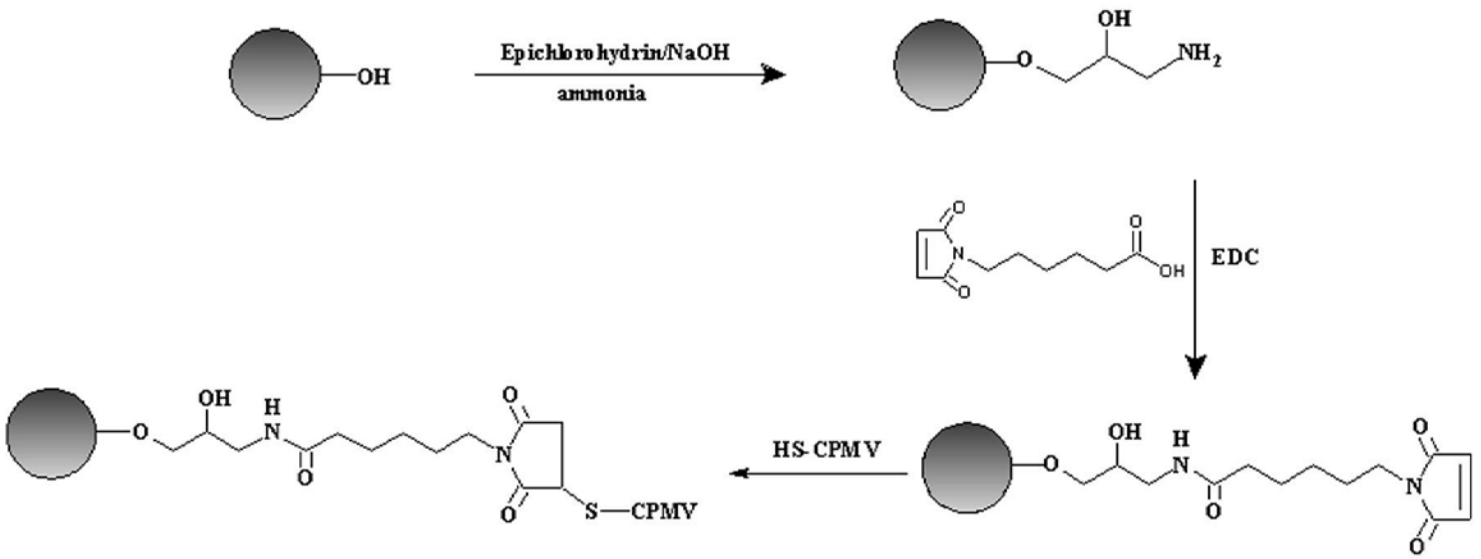

Figure B.1. Surface modification of magnetic nanoparticles with EMCA crosslinker for the attachment of CPMV

B.3 Results and Discussion

Surface modification of $CoFe_2O_4$ with crosslinker ε-Maleimidocaproic acid provided the attachment points between the Cowpea Mosaic virus and $CoFe_2O_4$ magnetic nanoparticles. Three-dimensional reconstruction of the cryo-TEM image of the native CPMV and that of $CoFe_2O_4$ bound to CPMV can be seen in Figure B.2. Clearly, the two images are different. From the native structure, you can see pores on the capsid. These pores are then filled with cone shaped structures, presumably cobalt spinel ferrites. There are cysteine groups in the interior of CPMV one of which is close to exterior of CPMV capsid. Cobalt spinel ferrites-EMCA nanoparticles presumably are binding at the pores of the capsid. At this time, there is not enough data to confirm the binding between the nanoparticles and the viral capsid. Since similar structures such as gold nanoparticle bound mutant CPMV, seen in Figure B.3,[22,31] have been observed before, it likely that the image seen in Figure B.2.b is $CoFe_2O_4$ bound to CPMV.

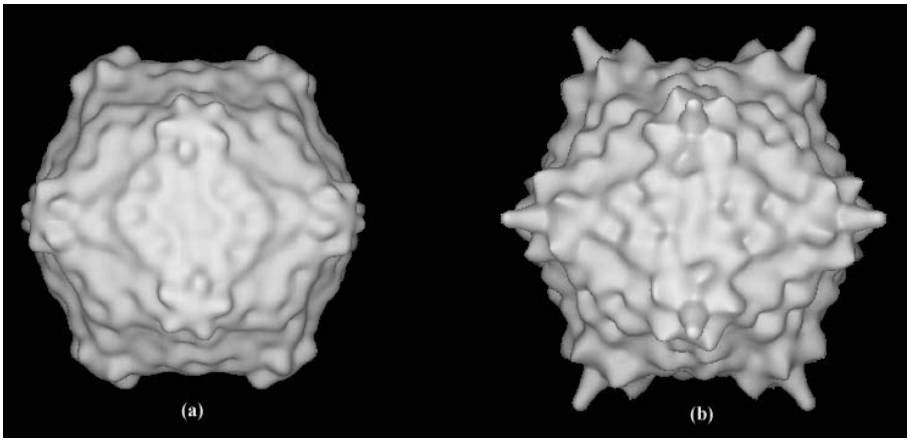

Figure B.2 Three dimensionally reconstructed cryo-TEM image of the (a) native CPMV virus and (b) CPMV-$CoFe_2O_4$ virus.

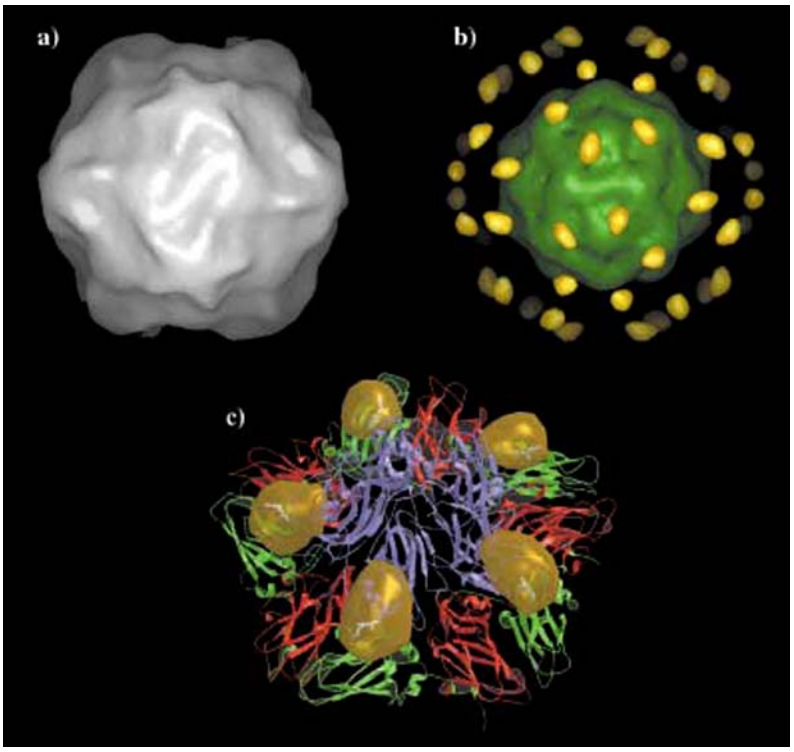

Figure B.3 (a) Three dimensional reconstructed cryo-TEM image of mutant CPMV labeled with 1.45nm gold nanoparticles. (b) Difference electron density map showing the gold nanoparticles and the nucleic acids. (c) Superimposed image of a pentametric section of the difference electron density map and the atomic model of CPMV.[22,31]

B.4 Conclusion

In this study we focused on coupling of $CoFe_2O_4$ to CPMV. Data shown thus far is preliminary and will require further systematic investigation to confirm the binding of CPMV to $CoFe_2O_4$. The conjugation chemistry described here is straightforward and should be applicable to different magnetic nanoparticles such as $MnFe_2O_4$ as well as other viral systems such as the poliovirus. We know that there are only a few internal cysteine groups available for anchoring magnetic nanoparticles. Hence, the reactivity between magnetic nanoparticles and CPMV may be enhanced by using mutant CPMVs that contain multiple cysteine insertions. Added cysteine residues will protrude to the exterior of the capsid providing more anchoring points. Although data described here is preliminary, the foundation for a systematic study to probe into different crosslinking chemistry as well as potential applications such as magnetically guided gene transfer, has been laid out.

B.5 References

(1) http://www.pcguide.com/ref/hdd/hist-c.html, 2004; Vol. 1997-2004.

(2) Hayes, B. *American Scientist* **2002**, *90*, 212.

(3) Thompson, D.; Best, J. S. *IBM J. Res. Develop.* **2000**, *44*, 311.

(4) http://nanotechweb.org/articles/new/2/56/10/1, 2003.

(5) Livingston, J. D. *Driving Forces: The Natural Magic of Magnets*; Harvard University Press: Cambridge, 1996.

(6) O'Handley, R. C. *Modern Magnetic Materials: Principles and Applications*; Wiley & Sons, Inc.: New York, 2000.

(7) Popplewell, J. *Phys. Technol.* **1984**, *15*, 1650.

(8) Raj, K.; Moskowtiz, R. *IEEE Trans. Magn.* **1980**, *16*.

(9) Rabine, Y.; EurekAlert, 2002.

(10) Moroz, P.; Jones, S. K.; Gray, B. N. *Int. J. Hyperthermia* **2002**, *18*, 267.

(11) Gilchrist, R. K.; Medal, R.; Shorey, W. D.; Hanselman, R. C.; Parrott, J. C.; Taylor, C. B. *Ann. Surg.* **1957**, *146*, 596.

(12) Rosenweig, R. E. *J. Magn. Magn. Mater.* **2002**, *252*, 370.

(13) Pel-Freez.com.

(14) Roger, J.; Pons, J. N.; Massart, R.; Halbreich, A.; Bacri, A. *Eur. Phys. J. AP* **1999**, *5*, 321.

(15) Yeh, T. C.; Zhang, W.; Ildstad, S. T.; Ho, C. *Magn. Reson. Med.* **1993**, *30*, 617.

(16) Yeh, T. C.; Zhang, W.; Ildstad, S. T.; Ho, C. *Magn. Reson. Med.* **1995**, *33*, 200.

(17) Wunderbaldinger, P.; Josephson, L.; Weissleder, R. *Bioconjugate Chem.* **2002**, *13*, 264.

(18) Schoepf, U.; Marecos, E.; Melder, R.; Jain, R.; Weissleder, R. *BioTechniques* **1998**, *24*, 642.

(19) Lewin, M.; Carlesso, N.; Tung, C.-H.; Cory, D. T.; Scadden, D. T.; Weissleder, R. *Nature Biotechnology* **2000**, *18*, 410.

(20) Perez, J. M.; Simeone, J.; Saeki, Y.; Josephson, L.; Weissleder, R. *J. Am. Chem. Soc.* **2003**, *125*, 10192.

(21) Perez, J. M.; Josephson, L.; O'Louglin, T.; Hogemann, D.; Weissleder, R. *Nat. Biotechnol.* **2002**, *20*, 816.

(22) Lin, T.; Johnson, J. E. In *Advances in Virus Research*; Maramorosch, K., Lauffer, M. A., Eds.; Elsevier, Inc.: Amsterdam, 2003; Vol. 62, pp 167.

(23) Brueing, G. *Virology* **1969**, *56*, 577.

(24) Pouwels, J.; Carett, J. E.; Lent, J. V.; Wellink, J. *Molecular Plant Pathology* **2002**, *3*, 411.

(25) Lin, T.; Che, Z.; Usha, R.; Stauffacher, C. V.; Dai, J. B.; Schmidt, T.; Johnson, J. E. *Virology* **1999**, *265*, 20.

(26) Porta, C.; Spall, V. E.; Loveland, J. E.; Johnson, J. E.; Barker, P. J.; Lomonosoff, G. P. *Virology* **1994**, *202*, 949.

(27) Raja, K. S.; Wang, Q.; Gonzalez, M. J.; Manchester, M.; Johnson, J. E.; Finn, M. G. *Biomacromolecules* **2003**, *4*, 472.

(28) Smith, J. C.; Lee, K.-B.; Wang, Q.; Finn, M. G.; Johnson, J. E.; Mrksich, M.; Mirkin, C. A. *Nano Lett.* **2003**, *3*, 883.

(29) Raja, K. S.; Wang, Q.; Finn, M. G. *ChemBiochem.* **2003**, *4*, 1348.

(30) Wang, Q.; Lin, T.; Johnson, J. E.; Finn, M. G. *Chem. & Biol.* **2002**, *9*, 813.

(31) Wang, Q.; Lin, T.; Tang, L.; Johnson, J. E.; Finn, M. G. *Angew. Chem. Int. Ed.* **2002**, *41*, 459.

(32) Rondinone, A. J.; Samia, A. C. S.; Zhang, Z. J. *J. Phys. Chem. B.* **1999**, *103*, 8676.

VITA

Eva Liang-Huang Heintz was born on August 12th, 1976 as Liang Huang in Chengdu, Szechuan, China to Ling Xiao Jia and Peihuang Huang. Eva, her mom, and dad immigrated to the United States on March 10th, 1984. She grew up in Los Angeles, California attending Logan Elementary and Nightingale Junior High. While attending Rosemead High School, Eva also received her Medical Assistant certification from Northwest College in West Covina, California. After graduating from Rosemead High School in 1993, Eva majored in Biochemistry at California State University, Los Angeles where she earned her B.S. in 1998 under the guidance of Dr. Wayne Tikkanen. In 2000, Eva received her M.S. in Chemistry from California State University, Los Angeles, under Dr. Feimeng Zhou's guidance. Eva joined Georgia Institute of Technology in August of 2000 to pursue her Ph.D. in Analytical Chemistry with a minor emphasis in Organic Chemistry. The focus of Eva's research in Dr. Z. John Zhang's group is primarily developing methods to conjugate magnetic nanoparticles to macromolecules for cellular delivery and subsequent magnetic manipulation.